# Automotive Free-Space Optical Communication at 1400nm

**James Francis Peter Farmer**

Balliol College

Supervisor:

**Prof. Dominic O'Brien**




Michaelmas Term 2020

A thesis submitted for the Degree of Doctor of Philosophy

Department of Engineering Science
University of Oxford
Parks Road, Oxford OX1 3PJ

# ABSTRACT

Future vehicular transportation will use autonomous and semi-autonomous systems with, in part, the aim of significantly improving road safety. Implementing a reliable communication system that allows for the sharing of information between vehicles and their environment could improve computational efficiency and facilitate collective pre-planning for arising situations. Optical Wireless Communication (OWC) is a promising candidate for a safe, reliable, and practical automotive communication system.

One of the major issues in the field of automotive OWC is the mitigation of ambient light, especially in the outdoor environment. In addition, maintaining a link in a dynamic environment and achieving high data rates over the distances required for automotive communication are crucial areas of current development.

This thesis describes the development of an optical communication system operating at 1400nm. The strong absorption of sunlight by water vapour at close to 1400nm creates a wavelength band with substantially lower ambient sunlight light noise than in the visible region. This noise benefit over the conventionally used visible range is explored in a link budget model, which compares the links at the different wavelengths.

A 1400nm link is then experimentally demonstrated using a custom-built hybrid LED. This provides 1400nm emission alongside visible emission, using a Quantum Dot based wavelength converter that is excited by the visible radiation. This provides simultaneous illumination and communication in the visible region of the optical spectrum and at 1400nm in a single, small form factor package. With this system, data rates of 1.75Mb/s at 1400nm and 41Mb/s at 450nm could be achieved. Using a second, dedicated 1400nm transmitter, developed using commercially available InGaAsP LEDs, a >4.5Mb/s 1400nm link could be facilitated over long ranges (1.25-5m) and outdoors in a high ambient light scenario.

Finally, consideration is given to the potential enhancement of the receiver side of a 1400nm link with the employment of a fluorescent concentrator (FC). 3D printing is explored for the fabrication of these FCs in the visible and the NIR range, with the possibility of new topologies and fluorescence properties being quickly prototyped and characterised. As a proof-of-concept for this new fabrication procedure, a visible FC with a signal gain of 4 could be demonstrated. In addition, the fabrication method was extended to PbS quantum-dot based NIR FCs to be used within the receiver of the proposed 1400nm link system.

*This thesis is dedicated to my mother, Caroline. We did it.*

*La chance ne sourit qu'aux esprits bien préparés. – Louis Pasteur*

# ACKNOWLEDGEMENTS

This thesis results from the generosity, kindness and hard work of a significant number of people throughout my life. Without which, I would be a fraction of the person I have grown to become.

Firstly, concerning the thesis and my tuition, I would like to thank Prof Dominic O'Brien for taking a chance on me as a DPhil student within his group. In addition, I would like to thank him immensely for his council, for crafting me into a researcher who has confidence in his convictions and providing me with the creative freedom to pursue my ideas.

Thank you to Mr Grahame Faulkner for his advice and willingness to get involved in the numerous problems I have encountered during my DPhil. His years of advice have helped me to think more practically about the problems I face. With his mentorship, I have become an engineer who has developed a passion for manufacturing devices and developed a greater eye for detail. Thank you also for all the orders you put through for me and the risk assessments you reviewed which were not always given to you at the most convenient times.

To my friends and colleagues Vincent Lee and Paramin Sangwongngam for the comradeship we have shared over the past several years. For the talking through of problems, both professional and personal, I am extremely grateful to you both. My DPhil was made all the easier for having you to rely upon. I would also like to thank the many people I have collaborated with during my DPhil, including Prof Hyunchae Chun, Dr Ravinder Singh, Daniel Gregory, Prof Andrew Watt and Dr Wajahat Ali. Without whom the reach of my thesis would have been significantly limited.

To the various teachers who have guided and supported me during my education, thank you. I would like to especially thank Mrs Bull and Mr Gleeson, who saw that I had the makings of a scientist and passionately fostered my love of all things technical. Mrs Fletcher, who worked with me tirelessly to improve my English skills, so that I could cope with the writing challenges that were to face me. To Dr Tejas Parikh for his tuition in my A-level mathematics.Finally to Ms Lavery, who gave up her Wednesday lunchtimes each week to teach me higher syllabus GCSE mathematics, setting me on the path to study undergraduate physics.

I would also like to take the opportunity to thank my friend Prof Norman McCubbin, who has been instrumental in my love of science and was always willing to provide advice. Since our first meeting when I was 16, with my passion for physics, you have help me in so many ways and have always taken a caring interest in my progress. I can never thank you enough for your kindness. I also wish to thank Mrs Inge McCubbin for her kindness, hospitality, and apple cake, which were always greatly appreciated.

To Omid, Thank you always for the laughs and for keeping me grounded, particularly during the last year. It has been great to be reminded that during this COVID lockdown, the world isn't filled with only a thesis. I do not think either of us could have imagined where we would end up in our lives and I think we might have laughed at the idea of doing PhDs at Oxbridge. You often inspire me to be the best I can be, not only academically but also with your generosity and kindness. I think I would have achieved a fraction of what I have without you around. Having said this, you might want to frame this text, as I have now used up my yearly 'Be nice to Omid' fund so expect the usual mocking from here on in.

To Jack, Cal, Will, Jenny, Marcus, Sam and Tim. Over the past decade that we have known each other, I have developed from a timid person who struggled to make friends to someone confident in his ability and an understanding on the deepest level of what friendship can be. In large part, this is down to you guys. Thank you all for being there during some of the toughest times of my life, but mostly thank you for helping to make me a rounded individual. I am always up for a game of smash, but I'm still not up for playing Twilight Imperium.

To Tobi, Eloise, Daan, Miles, Maria, Helen, Janina and Sophie. Thank you for expanding my culture, challenging my assumptions, taking a local boy, and helping him see the world from an international viewpoint. Thank you for your friendship, the great deal of personal and intellectual conversations we have had over the years, and how this has enriched my life, I can not express.

To my girlfriend, Mirjam, whose infinite patience with my moaning has been so needed, particularly over the past year despite her own challenges. Thank you for your constant love and friendship and being there for me when I have struggled, particularly with the writing of this work. Without your love and support, your encouragement and belief in me, I doubt that this work would have been completed, even though you must have felt like Sisyphus sometimes. I owe a huge debt to you for your commitment and to helping me to see the light at the end of the tunnel; hopefully, it is LED-based.

To my Grandparents, Sheila, Pete, John and Barbara whom all contributed to my education where they could, always encouraged me by listening to my mad ideas and telling me there was nothing I could not achieve.

To my father, Robin, thank you for all the extra hours you had to work to get me the help I needed with my Dyslexia. We did not always have much, but whatever we did have was given to me to help with my education. I know you often say you didn't do as much as mum, but I would never have had the chance to get to this point without your hard work. Thank you for always listening to my ideas, even when I don't make much sense.

Finally, I would like to thank my mother, Caroline, who saw me off on this journey but unfortunately can not be here to see me finish. Since I was age 5, when she realised that I was struggling in school, insisting I got tested for Dyslexia, to the day she died where we were chatting about my transfer of status report, my mother always fought for the help I needed and encouraged me to reach my full potential. Without her love, I do not doubt that I would have been bound to a life of frustration, believing I could achieve so much but being passed over by so many. Together with my father, both have proved to me that there is very little that one cannot achieve with loving parents.

Myself and this work are humbly the product of those above and so many more which I do not have space to thank. To all, from the bottom of my heart, thank you. I hope this work goes some way to show your trust and hard work were well place in me.

# TABLE OF CONTENTS


Abstract ..... 2

Acknowledgements ..... 5

List of Figures ..... 12

List of Tables ..... 14

1. Chapter: Background ..... 17

1.1 Introduction ..... 17

1.2 Automotive Optical Wireless Communication ..... 18

1.2.1 Overview ..... 18
1.2.2 Recent Developments in the Field ..... 19
1.2.3 Current Research and Challenges ..... 21
1.2.4 Summary ..... 31

1.3 Automotive Optical Communication at 1400nm ..... 33

1.4 Thesis contribution and structure ..... 34

1.5 Key Contributions of this thesis: ..... 35

1.6 Publications ..... 36

2. Chapter: Modelling of automotive OWC links ..... 37

2.1 Introduction ..... 37

2.2 Methodology ..... 37

2.2.1 Modelled components ..... 37
2.2.2 Ambient light noise ..... 46
2.2.3 BER using NRZ-OOK ..... 47
2.2.4 Modelling of water in the optical path ..... 48
2.2.5 Hardware parameters of sources and receivers ..... 50

2.3 Simulation Results ..... 54

2.3.1 Brake and Headlight Communication Channels at 450nm ..... 54
2.3.2 Daylight Running Light Communication Channels at 450nm and 1400nm ..... 55

2.4 Discussion ..... 61

2.4.1 VLC using Headlights and Brake lights ..... 61
2.4.2 VLC using Daylight Running Lights ..... 61

2.5 Conclusions ..... 64

3. Chapter: Hybrid LED ..... 66

3.1 Overview ..... 66

3.2 Introduction to Quantum Dots ..... 66

3.3 Hybrid LED Construction ..... 68

3.3.1 White LED selection ..... 68
3.3.2 PbS QDs ..... 70

3.3.3 Sample Fabrication ..... 71
3.4 Characterisation of optical properties ..... 81
3.4.1 Emission spectrum at 1400nm ..... 81
3.4.2 Illumination ..... 82
3.4.3 Stability ..... 84
3.5 Characterisation of Communication Properties ..... 85
3.5.1 Experimental set-up ..... 85
3.5.2 Bandwidth Measurements ..... 87
3.5.3 On-Off keying communication in dark conditions ..... 89
3.5.4 Sunlight effect on 1400nm and 450nm links ..... 91
3.5.5 Characterising the ambient sunlight benefit at 1400nm ..... 93
3.6 Discussion ..... 98
3.6.1 Communication at 450 nm and 1400 nm ..... 98
3.6.2 Robustness to sunlight ..... 99
3.6.3 Illumination ..... 100
3.6.4 Functional Encapsulation using DLP resin ..... 100
3.6.5 Vehicular deployment ..... 101
3.7 Conclusion ..... 101
4. Chapter: 1400nm Transmitter ..... 103
4.1 Overview ..... 103
4.2 Transmitter Design ..... 103
4.2.1 Choice of Source ..... 103
4.2.2 Circuit Design ..... 104
4.2.3 Protective Casing ..... 107
4.3 Performance ..... 108
4.3.1 Safety testing ..... 108
4.3.2 Power measurement ..... 109
4.3.3 Bandwidth ..... 109
4.3.4 Communication Performance ..... 111
4.3.5 Ambient light mitigation ..... 113
4.4 Discussion ..... 115
4.5 Conclusion ..... 116
5. Chapter: Fabrication Method for NIR fluorescent Concentrators ..... 118
5.1 Introduction ..... 118
5.1.1 Optics of Fluorescent concentrators ..... 118
5.1.2 Fluorescent concentrators in optical communication ..... 120
5.2 Methods ..... 122
5.2.1 Concentrator Fabrication ..... 122
5.2.2 Visible concentrator bandwidth and signal gain measurements ..... 126
5.2.3 1400nm Illumination ..... 127
5.3 Results ..... 128

5.3.1 Substrate Characterisation ..... 128
5.3.2 Visible Concentrators using Coumarin 7 ..... 130
5.3.3 Visible Concentrator bandwidth and signal gain ..... 132
5.3.4 NIR Concentrators ..... 133
5.4 Discussion ..... 135
5.4.1 Functional 3D Printed Fluorescent Concentrator ..... 135
5.4.2 NIR Fluorescent Concentrators ..... 137
5.5 Conclusion ..... 138
6. Chapter: Conclusion and future work ..... 139
6.1 Conclusion ..... 139
6.2 Future work ..... 141
References ..... 143

# LIST OF FIGURES

Figure 1: Schematic of Vehicle to vehicle (V2V) communication. ..... 18
Figure 2: UV-Visible-NIR region of Air Mass 1.5 Spectrum. [49] ..... 33
Figure 3: Link model diagram [51]. ..... 38
Figure 4:Optical Transmitter for VLC [51]. ..... 38
Figure 5: Relative emission intensity against wavelength for white and red light LED sources used in the model. ..... 40
Figure 6: Diagram of a typical photodiode based VLC receiver [8]. ..... 41
Figure 7: Diagram of a Compound Parabolic concentrator (CPC), redrawn from [61]. ..... 41
Figure 8: Equivalent circuit of a photodiode with amplifier. Where isig is the signal current, ishot is the shot noise components of the signal and iamb is the shot noise induced by ambient light [51]. ..... 42
Figure 9:Diagram of imaging receiver with direct signal and noise sources. ..... 45
Figure 10:BER against x and y ranges for brake light link (left) and headlight channel (right) for night and direct sunlight conditions. Car image not to scale in relation to the Figure. ..... 54
Figure 11: BER against x and y range for 450nm and 1400nm links under night-time and direct sunlight conditions. (a) 450nm and ideal 1400nm link without atmospheric water present. (b) 1400nm link in conditions of various atmospheric water contents. ..... 56
Figure 12: BER against x and y range for imaging receiver link at 10000 lux with saturation contour (red). ..... 59
Figure 13: Diagram of LED bandwidth measurement experimental set-up. ..... 68
Figure 14: Attenuation (dB) versus frequency (Hz) for Osram compact CM and CL LEDs with 80mA bias applied. ..... 69
Figure 15: Absorption and emission spectrum of Pbs QDS in toluene (10mg/mL) [77]. ..... 70
Figure 16: Samples of various QD concentrations with UR5634 polyurethane resin. ..... 72
Figure 17: Diagram of UV Gun optics. ..... 74
Figure 18: Images of UV curer built to cure IBOA/QD samples. ..... 75
Figure 19: Fabricated test samples of polystyrene, PMMA and UV curing resin. ..... 78
Figure 20: Experimental set-up for power measurements. ..... 79
Figure 21: Emission spectrum of the DLP QD sample when excited with a white light LED (Osram OSLON Compact CM) ..... 81
Figure 22: Emission spectrum of the hybrid LED over the visible region. ..... 82
Figure 23: CIE 1931 standard observer plot with UNECE permitted daylight running light region and marker for white light LED and hybrid LED CIE coordinates. ..... 84
Figure 24: Normalized Signal Power versus time of the hybrid LED 1400nm emission. ..... 85
Figure 25: Diagram of Hybrid LED Experimental Set-up. ..... 86
Figure 26: Frequency response (electrical-electrical) of 1400nm component of light emitted from Hybrid LED. ..... 88
Figure 27: Frequency response (electrical-electrical) of the 450nm component of light emitted from the hybrid LED. ..... 89
Figure 28: BER versus data rate (Mb/s) of the 1400nm channel for 0.25m, 0.5, 0.75m links with and without DFE. Forward Error Correction (FEC) ..... 91
Figure 29: BER versus data rate (Mb/s) of the 450nm channel for 0.25m, 0.5m, 0.75m links without DFE. Forward Error Correction (FEC) ..... 91
Figure 30: BER histogram for darkroom (2 lux) and sunlight conditions (33600 lux) for the 1400nm link. ..... 92

Figure 31: BER histogram for darkroom (2 lux) and sunlight conditions (28000 lux) for the 450nm link. ..... 93
Figure 32: Picture of the experimental set-up for 450nm and 1400nm power measurements, angled to match the incident angle of the sun. ..... 94
Figure 33: Transmission (relative to calibrated source) of collimated radiation through 1400nm and 450nm filters. ..... 95
Figure 34: Circuit Diagram of 1400nm Transmitter. ..... 105
Figure 35: Pictures of PCB design with ground fill included (left) and excluded (right). ..... 106
Figure 36: Picture of complete transmitter with 3D printed surround. ..... 107
Figure 37: Absolute Irradiance of 1400nm transmitter at full power (distance = 200mm)..... 108
Figure 38: Diagram of the experimental setups for A: Profiling of the receiver, B: Profiling of the transmitter, and C: Communication test (with the addition of a 1400 bandpass filter)..... 110
Figure 39: Attenuation (dB) versus Frequency (MHz) for the receiver, receiver and transmitter combined and transmitter. ..... 111
Figure 40: Picture of the experimental set-up for 5m link. ..... 112
Figure 41: Log10(BER) versus data rate (Mb/s) over various link distances. ..... 113
Figure 42: Experimental set-up for outdoor 1400nm link experiment. AWG and laptop not shown in image. ..... 113
Figure 43: BER histograms for night (2.4 lux), typical daylight (10800 lux) and direct sunlight (81000 lux) conditions for the 1400nm link over a link distance of 0.25m. ..... 115
Figure 44: Ray propagation in a fluorescent concentrator [101]. ..... 119
Figure 45: Cross-section through a DLP printer. ..... 123
Figure 46: Clear DLP printed substrate for fluorescent slab concentrator. ..... 124
Figure 47: Set of various substrates of thickness 1-50mm ..... 124
Figure 48: Absorption spectrum of PbS QDs used for NIR concentrators [78]. ..... 125
Figure 49: The bandwidth measurement experimental set-up for the visible FC. ..... 127
Figure 50: Image of single 1400nm transmitter used for the NIRFC characterisation. ..... 128
Figure 51: Transmission (%) versus Wavelength (nm) for resin samples of a 1-50mm thickness. ..... 129
Figure 52: Resin transmission versus sample thickness for absorption (blue) and emission wavelengths (red) of (a) Coumarin 7 and (b) PbS QDs, including Beer lambert law fitting. ..... 130
Figure 53: Images of completed fluorescent concentrator with and without illumination from a 405nm source. ..... 131
Figure 54: Spiral and fibre-based fluorescent concentrators. ..... 132
Figure 55: Attenuation versus Bandwidth for 3D printed visible Fluorescent Concentrator. ..... 132
Figure 56: Attenuation versus Frequency (MHz) for a single LED transmitter with -3dB line (Red). ..... 134

# LIST OF TABLES

Table 1: Selection of existing literature for VLC links in the automotive environment. ..... 23
Table 2: Power ratio (dB) of various filters relative to 450nm filter with a 12nm optical passband. ..... 34
Table 3: Parameters used to model light sources. ..... 51
Table 4: Parameters used for the photo-diode simulation ..... 52
Table 5: Parameters used in the imager model ..... 53
Table 6:Results of Blue and 1400nm filtered Photodiode receiver links. Maximum communication distance (m) for BER = $10^{-6}$; RH: relative humidity. ..... 57
Table 7: Results of the imager receiver link mode in comparison to the PD model of a 450nm channel ..... 58
Table 8: Results of blue and 1400nm filtered photodiode receiver links in foggy conditions. Maximum communication distance (m) for BER = $10^{-6}$. ..... 60

# ABBREVIATIONS

**AC** – Alternating Current

**APD** – Avalanche Photodiode

**AWG** – Arbitrary Waveform Generator

**BER** – Bit Error Rate

**CdSe** – Cadmium Selenide

**CIE** – International Commission on Illumination

**CMOS** – Complementary Metal-Oxide-Semiconductor

**CPC** – Compound Parabolic Concentrator

**CuInSexS2-x** – Copper Indium Selenide Sulphide

**CWL** – Centre Wavelength

**dB** – Decibel

**DC** – Direct Current

**DFE** – Decision Feedback Equalization

**DLP** – Direct Light Projection

**EU** – European Union

**FC** – Fluorescent Concentrator

**FDM** – Frequency Division Multiplexing

**FDMA** – Frequency-Division Multiple Access

**FEC** – Forward Error Correction

**FOV** – Field-Of-View

**FWHM** – Full Width at Half Maximum

**Ge** – Germanium

**GPS** – Global Positioning System

**IBOA** – Isobornyl Acrylate

**InGaAs** – Indium Gallium Arsenide

**InGaAsP** – Indium Gallium Arsenide Phosphide

**IR** – Infra-Red

**LED** – Light Emitting Diode

**LOS** – Line-of-Sight

**LTA** – Logarithmic Transimpedance Amplifier

**MCPCB** – Metal Core Printed Circuit Board

**MIMO** – Multiple-Input and Multiple-Output

**NEP** – Noise Equivalent Power

**NIR** – Near Infra-Red

**NIRFC** – Near-Infrared Fluorescent Concentrator

**NRZ-OOK** – Non-Return to Zero On-Off Keying

**OD** – Optical Density

**OFDM** - Orthogonal Frequency-Division Multiplexing

**OFDMA** – Orthogonal Frequency-Division Multiple Access

**OOK** – On-Off Keying

**OWC** – Optical Wireless Communication

**PbS QDs** – Lead Sulfide Quantum Dots

**PCB** – Printed Circuit Board

**PD** – Photodiode

**PLA** – Polylactic Acid

**PMMA** – Polymethyl Methacrylate

**PPM** – Pulse-Position Modulation

**QAM** – Quadrature Amplitude Modulation

**QPSK** – Quadrature Phase Shift Keying

**QY** – Quantum Yield

**RF** – Radio Frequency

**Si** – Silicon

**SNR** – Signal-to-Noise

**SPAD** – Single Photon Avalanche Photodiode

**UNECE** – United Nations Economic Commission for Europe

**UPFS-OOK** – Undersampled Phase-Frequency Shift On-Off Keying

**UV** – Ultraviolet

**V2I** – Vehicle-to-Infrastructure

**V2V** – Vehicle-to-Vehicle

**V2X** – Vehicle-to-Everything

**VLC** – Visible Light Communication

**VSCC** – Vehicle Safety Communication Consortium

**ZnS** – Zinc Sulfide

# 1. CHAPTER: BACKGROUND

## 1.1 INTRODUCTION

It is estimated that 1.25 million people are killed on the world's roads each year [1]. In addition, 50-60 million people are seriously injured, and by 2030 fatalities on roads are predicted to be the seventh most significant cause of fatalities worldwide [1]. In the UK, 95% of all road accidents involve some human error, and in 76% of cases, humans are solely to blame [2]. Besides injury and loss of human life, road accidents are estimated to cost £34,000 per minute for hospital costs and damage to property and vehicles [2]. As an effective solution to these problems and the issue of traffic congestion, autonomous and semi-autonomous vehicles are currently being developed by companies such as Google, Tesla and Oxbotica [3][4][5].

Currently, these vehicles are designed to work independently [6]. As such, each vehicle needs to be equipped with many sensors and detection systems, so that sufficient coverage can be provided to identify neighbouring objects, other vehicles, cyclists or pedestrians, who could cause accidents [7]. The processing of this data is computationally expensive, requiring highly sophisticated algorithms to process sensor data in real-time [6].

A communications system operating between vehicles could allow for the sharing of information about a vehicle's own data, such as GPS position and speed, but also information about hazards encountered [6]. Such a system could also allow for advanced warnings and intelligent traffic control, which is decided on by a collective of vehicles, in order to ensure passenger comfort and safety.

Due to the technology's maturity, Radio frequency (RF) communication is the predominant choice for such an automotive communication system. A significant issue with using only RF systems is spectrum scarcity and high interference when the user density increases [7],

for example, in an urban environment. Due to the potentially safety-critical nature of vehicular communication, any system must be robust enough to be implemented on the world's roads. Therefore, an alternative system for free-space communication is highly desirable. Optical Wireless Communication (OWC) systems are promising candidates for a safe, reliable, and practical automotive communication system.

## 1.2 Automotive Optical Wireless Communication

### 1.2.1 Overview

Optical wireless communication (OWC) facilitates the transmission of information by modulating an optical medium generated by a light source and detected by a light-sensitive element. OWC is a growing research area, with systems operating over a wide range of wavelengths and data rates (see Table 1).

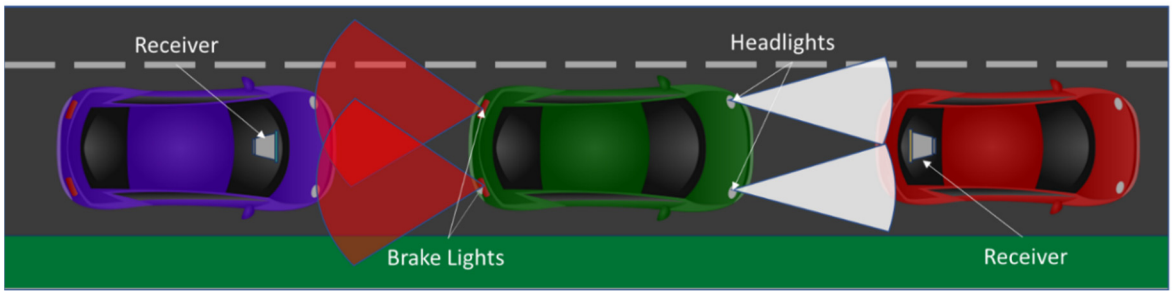



*Figure 1: Schematic of Vehicle to vehicle (V2V) communication.*

Figure 1 shows a typical scenario for the employment of OWC in the automotive environment. Using automotive lighting (headlights, taillights, brake lights, and daylight running lights) as modulated sources, and photodiode (PD) or CMOS camera-based receivers which sit within the illumination of the transmitter, optical communication channels could be facilitated. Due to the increasing use of LED-based automotive lighting and the inclusion of camera sensors on vehicles, which could act as transmitters and receiver respectively, OWC is becoming an increasingly attractive communication system in the automotive environment [7].

OWC operates on a Line-of-Sight (LOS) principle, which leads to a high level of security: An attacker would be required to be in visual range of the victim link, making it less likely to be hacked compared to that of an RF-based system [7]. This is of particular importance for the transmission of safety-critical information between vehicles.

The LOS nature of the link also enables the system to be highly scalable due to the expected low number of vehicles within direct LOS of any other, those being of the most importance since these are the vehicles most likely to collide [7]. Because of the directional nature of the transmitted light, the system is useful for high user density urban environments where RF systems will suffer from increased interference.

### 1.2.2 Recent Developments in the Field

Two types of automotive OWC can be distinguished based on the communication partners involved. Vehicle-to-Vehicle (V2V) OWC is communication between vehicles, allowing them to warn and know of hazards in the immediate environment [8 and references therein].

Vehicle-to-infrastructure (V2I) communication allows for data to be sent between vehicles and transceivers linked into the transport infrastructure, such as traffic lights, over-head gantry displays, and devices involved in traffic monitoring [8]. These transceivers could provide connectivity between vehicles and a central network allowing for wide-area communication of accident and traffic data.

In the following, a brief overview is given on the current state of research and development of OWC in the automotive environment.

***Vehicle to Infrastructure (V2I) communication***

The use of infrastructure as part of the optical wireless framework has been investigated to construct a well-connected, central network within which vehicles can communicate. Traffic

lights have been one the most widely investigated transmitters in automotive OWC, partially because they are commercially available, tightly regulated devices [8].

In [9], a 2.4kb/s link has been demonstrated over 130m outdoors using a green traffic light, one of the longest such Visible Light Communication (VLC) links. In [10], a 50m link was demonstrated under heavy snowfall conditions with the employment of a VLC transmitter based on a commercially available traffic light. To account for movement of vehicles approaching a traffic light, researchers in [11] developed a tracking system, which could maintain the link when a vehicle (equipped with tracking device and receiver) approached.

Some of the proposed systems have reached a high level of technology readiness, such as a replacement for the Japanese police's traffic management system [12]. Through the use of a commercially available headlight unit mounted to a vehicle, a data rate of 3.1Mbp/s over a link distance of 25m could be facilitated to a set of narrow Field-of-View (FOV) receivers mounted at 5m above the road surface [12]. The link could be maintained when the vehicle was driven past the sensor at a speed of 20km/h [12].

Modelling work outlined in [13] concentrated on how non-LoS OWC might be achieved in an urban landscape, using traffic infrastructure. The simulation of indirect laser-based OWC using diffuse reflectors attached to buildings suggested that a 1Gbp/s link over 200m could be possible [13]. The employment of diffusers allowed for greater coverage but reduced security because of the diffuse nature of the link.

***Vehicle to vehicle (V2V) communication***

V2V envisions the use of the vehicular lighting infrastructure as transmitters for OWC between vehicles. The suitability of headlights for high-speed communication has been demonstrated in [14], where a data rate of 427.5Mbit/s could be achieved. Daylight running

lights were used as transmitters in [15] and rear lights and brake lights have also been considered but have not been as extensively tested yet [8].

In contrast to V2I communication, both ends of the link are mobile in a V2V scenario. To date, several links between two moving vehicles have been demonstrated, relying on the wide FOV of an imaging sensor based receiver to ensure alignment of transmitter and receiver [15, 16]. The system in [15] uses a wide FOV camera as a replacement of side mirrors. The following vehicles use their daylight running lights to transmit simple 24-bit messages about their vehicle type and driving actions to the front running vehicle. The link was tested between vehicles moving at 40km/h in day-and night-time conditions.

Overall, most research currently conducted on automotive OWC could be used interchangeably in both V2I and V2V. Consequently, progress made in either field will advance both technologies towards real-world applications.

### 1.2.3 Current Research and Challenges

Within the field of automotive OWC, there are several research areas, which contribute to the development of the technology. The following sections will provide a brief overview of the current status of this research.

***Data rate and communication range***

In order to assess the performance of automotive OWC systems, a benchmark for data rate and the desired minimum range needs to be defined.

The IEEE has defined a standard for outdoor applications of VLC, which for OOK modulation promotes a maximum of 100kbit/s data rate (IEEE 802.15.7-2011 and 2018) [17]. However, the implementation of the standard has been limited in the context of inter-vehicle VLC [18]. Thus, another source for defining minimum data rate requirements for OWC in the automotive context seems more appropriate at this point.

The vehicle safety communications consortium (VSCC) consisting of BMW, Ford, VW and others defined preliminary communication requirements for automotive RF links [19]. The consortium defined several high priority safety signals, including traffic signal violation warnings, lane changes, left turns, and pre-crash sensing [19]. For these, the minimum required data rate from the communication system is 9.04 kb/s. In addition to safety-critical signalling, the IEEE 802.11p standard extends the requirements to other applications, including multimedia, where data rates of 3-27Mbit/s are specified [20].

The VSCC envisions communication ranges of up to 1000m. However, it is essential to acknowledge that the reliability of these systems is more crucial over shorter distances where accidents are more probable to occur [19, 21]. Most common traffic scenarios are set at shorter distances of up 160m [21]. In summary, this defines minimum targets for data rate and range which should be met by VLC-based systems if applied in the automotive environment.

Table 1 provides an overview of the existing literature in the field, primarily focusing on the achievable ranges and data rates demonstrated. Currently, visible communication at the minimum required data rate and desired range (9kbit/s over ≈160m) has not yet been shown. However, several developments worth mentioning highlight how future research could rapidly change the feasibility of optical inter-vehicular communication.

*Table 1: Selection of existing literature for VLC links in the automotive environment.*

| Receiver Type | Receiver FOV | Data Rate | Link distance | Modulation scheme/ Coding technique | Comments | Reference |
|---|---|---|---|---|---|---|
| Imager | >22° | 10-20 Mbit/s | 2m | QFDM/QAM/Manchester coding | Static V2V | [16, 22, 23] |
| | | 10Mbit/s | 20m | | | |
| | | 32 kbit/s | 70m | | Mobile V2V | [22] |
| | | 2kbit/s | 110m | | | |
| | | 55Mbit/s | 1.5m | OFDM | Static V2X | [24] |
| Imager | | 50 bit/s | 160m | UPFS-OOK | Static | [25] |
| PD + tracking | 1.3° | 4.8kbit/s | 90m | 2PPM | V2I, furthest using PD | [26] |
| | 0.4° | 1-2 Mbit/s | 60m | QPSK, 16QAM | | [27] |
| Photo-transistor | ±15° | 2.4 kbit/s | 130m | OOK | V2I, longest experimental distance | [9] |
| PD | ±35° | 14Mbit/s | 15m | OFDM | V2V | [28] |
| PD | Not specified | 427.5Mbit/s | 1.2m | 64QAM | V2X, indoor test only | [14] |
| PD | ±15° | 11-50kbit/s | | OOK with Manchester coding | In & outdoors | [10] |

To date, communication links over typically 40-60m have been achieved using photodiode-based receivers at data rates of around 15kbit/s, or up to 2 Mbit/s when reducing the FOV to 0.4° [27, 29, 30]. As outlined previously, very narrow FOVs, as in this case, significantly limit the link mobility and stability in the scenario of moving transmitters and receivers. The longest link reported using a photodiode-based system has been shown in [26], where a communication distance of 90m at a data rate of 4.8kbit/s has been achieved using a 1.3° receiver FOV. At slightly lower data rates of 2.4 kb/s, the work in [9] achieved a link over 130m using a phototransistor combined with a logarithmic transimpedance amplifier.

For imaging receivers, in general, the data rate is fundamentally limited by the frame rate of the imaging sensor. The longest link which has been experimentally facilitated, used an imager-based receiver over a link distance of 160m at a data rate, dictated by the camera unit, of 50bit/s [25].

A fundamental problem with such a receiver is that even for high frame rate imaging systems, the achievable data rates are small compared with that of a photodiode-based receiver [8]. Links at higher data rates rely on techniques such MIMO (Multiple Input Multiple Output), where each LED of a multiple-LED emitter is used to facilitate separate channel with a set of pixels on the imager sensor of the receiver [24].

The works in [16, 22, 23, 24] explore the concept of creating a sensor which could provide the mobility and spatial resolution of an imager in conjunction with the high bandwidth of a photodiode based receiver. The optical communication imager is constructed of columns of dedicated imager and communication pixels. The imager pixels are first analysed to provide the location of the transmitter within the FOV. This data is then relayed to a controller which selects the nearest of the individually addressable communication pixels to receive the signal. Using this custom topology imager sensor, link distances of up to 110m have been achieved at a data rates of 2kbit/s [22]. At shorter link distances, much higher data rates (10-20Mb/s) were demonstrated using the same sensor (see Table 1) [22, 23, 24].

Within the field, one of the highest data rates which has been experimentally achieved is 427.5 Mb/s, using a commercial LED headlight over 1.2m link distance with a Bit Error Rate (BER) of $3.8 \times 10^{-3}$ [14]. Regarding practical automotive communication, the work was conducted indoors over a short distance using a modulation scheme (64 Quadrature amplitude modulation QAM) which will be considerably less robust to ambient light than the employment of on-off keying used in other systems. However, the results demonstrate that commercially available headlights can be modulated at high frequencies and should not be a limiting factor in developing high-speed VLC communication systems in the automotive environment.

***Mitigation of adverse weather conditions***

In addition to ambient light, adverse weather conditions also need to be considered to facilitate a practical automotive optical communication system.

Since the inception of OWC in the outdoor environment, concerns have been raised over the attenuation which adverse weather conditions could introduce into communication links. Conditions such as rain, fog, and snowfall are known to impair visual signalling, and so considerable effort has been spent on the development of models to accurately predict the link attenuation for these conditions [31, 32, 33, 34, 35, 36]. These models vary significantly, some of which assume a wavelength-independent attenuation at certain visibility conditions, others highlighting a wavelength-dependency [34, 35]. Overall, the models indicate that fog and snow impact optical links significantly, with rainfall being less detrimental [36].

Experimental evaluations of these models are sparse and do not always yield a conclusive picture. The wavelength dependency of light attenuation by fog was experimentally verified for example, in [35] for the range of 600-1600nm. However, the models can differ considerably from the experimental data depending on the visibility range. According to many models, but also the experimental data in [35], the employment of NIR in general, as opposed to visible, may well provide an SNR (Signal-to-Noise) benefit.

Testing VLC links in visibility-impaired scenarios have been performed, dealing with heavy snowfall in a blizzard, smoke, and fog [10, 37, 38]. To systematically assess the effects of fog and smoke, links have been tested in specially designed chambers that can provide defined visibility conditions [38, 39].

Regarding the mitigation of adverse weather conditions on an OWC link, limited literature has been published. Regarding simulation, the use of Single Photon Avalanche Photodiodes (SPADs) in the receiver to improve sensitivity for links in fog conditions is considered in

[32]. The authors compare the use of SPADs to Avalanche photodiode's (APDs) and estimate a 1.62-times increase in the maximum link distance achievable. Although this improvement could prove to be highly useful in conditions such as snowfall or fog with low visibility, there is currently no modelling on the effects of how such a link would handle high degrees of ambient light and in particular sunlight.

Hybrid Systems, combining RF and optical communication, could also mitigate these effects as can be seen in [40, 41]. RF technology can be used for longer-range communication, where OWC links can be critically impaired by adverse weather conditions [40]. LOS-based optical links could be used in high user-density environments where the robust transmission of safety-critical data cannot be guaranteed due to channel interference and congestion in RF-based links [41]. As such, the optical system could be supplemented by RF to provide better robustness for safety-critical data in both links.

***Mobility***

OWC requires a LOS link between emitter and receiver. In an automotive scenario, both emitter and receiver are dynamic; alignment of the link becoming a key challenge.

Consequently, the FOV of the receiver is crucial to the link stability, especially when safety-critical data is being transmitted. Photodiode based receivers with FOVs of around ±15° have been used in several papers [9, 10, 28]. Based on the typical lane width in the EU (≈4m) and an assumed minimal inter-vehicle distance of >15m, a ±15° FOV is sufficient to cover vehicles in the same and the nearest adjacent lanes [8, 42]. For traffic-jam scenarios, congestion, and infrastructure communication, larger FOVs will be required. In order to achieve larger FOVs, the use of multiple PDs at various angles has been explored, such as in [8, 28], where a FOV of up to ±35° is facilitated. Multiple sensors could also be placed on various sides of a vehicle to facilitate a full 360° FOV.

In research focussing on the link robustness to ambient light, narrow FOV PD-detectors are often employed (see Table 1) [26, 27]. In turn, this limits the mobility of the system, making the link susceptible to connection losses if transmitter and receiver move relative to each other. In an actual, mobile scenario, this degree of alignment will be problematic, and the narrow FOV may render the link unsuitable.

In an attempt to circumvent connection losses of small FOV-receivers, while using their robustness to ambient light, tracking systems have been implemented. Such systems would allow the narrow FOV receiver to follow the emitter's relative movement, compensating for the displacement [11, 26, 43].

The device in [11] uses a wide-and a narrow FOV camera which facilitates coarse and fine tracking. The camera data is used as feedback for two galvanometer mirrors, facilitating tracking in the vertical and horizontal plane. In a stationary, outdoor setting with a 0.4° receiver FOV, data rates of up to 2Mb/s with a BER of $10^{-4}$ using a 16QAM modulation scheme could be reached over a distance of 60m [11]. For preliminary testing of the tracking ability, the system was mounted into a vehicle, moving at 35km/h towards the transmitter. The recorded data suggests that the system can compensate for vibration in the link when driven directly towards the source. Nevertheless, these systems come at a higher overall complexity, particularly with the use of mechanically moving parts that may require regular maintenance.

In contrast to PD-based systems, the employment of imager sensors in the receiver offers a large FOV even at high levels of ambient light, making connection losses less of a concern [16]. As such, imaging-based communication links have been established on moving vehicles, as demonstrated in [15, 16, 22].

In addition to a suitable FOV, another critical feature of the mobility of such systems is the ability to deal with multiple users. Imager sensors can do this spatially by resolving different users and noise sources onto different pixels [16, 22, 23, 24]. In photodiode-based systems, there has been limited literature published on multiple user optical automotive communication. The concept of Frequency Division Multiplexing (FDM) is a scheme which could enable such multi-user systems. In FDM, the bandwidth of a link can be divided into non-overlapping or orthogonally overlapping subcarriers (FDMA or OFDMA) to create individual frequency bands for users on a network.

An example of the use of OFDMA schemes can be found in [44], where researchers facilitate the simultaneous reception of four users, with each user assigned 8 of 32 subcarriers. This provided a data rate of 10.8Mb/s per user over a range of 30m whilst keeping the BER $< 10^{-3}$. Such systems could dynamically tailor the bandwidth and number of subcarriers to account for the type and priority of information and the number of users on the network. For the future employment of such a modulation scheme, ambient light mitigation is critical to a robust multi-user system to minimise inter-user interference [44].

***Ambient light mitigation***

Ambient sunlight, both direct and diffuse, is the dominant ambient light interference component for outdoor optical communication.

One type of receiver investigated in the literature is based on imaging sensors. By their topology, they exhibit partial immunity to sunlight. In such a receiver, an imaging lens in front of the sensor will focus incident collimated light from different positions onto different sensor pixels. This allows for the discrimination of direct ambient light and multiple sources within the FOV of the receiver. As a result, several proof-of-principle experiments have demonstrated imager-based links in daylight conditions. [16, 15, 25]. Despite this key

advantage, the diffusive component of the ambient light, due to its Lambertian nature, will be spread uniformly across the imager, inducing a shot noise in the imaging pixels.

Within a photodiode-based communication system, the receiver will detect an AC communication signal along with DC and AC noise components. The DC photocurrent resulting from the detection of sunlight can easily be removed, leaving only the AC signal and the unavoidable AC shot noise. This noise component can easily become dominant in an OWC system, limiting performance, and potentially saturating the receiver. Different strategies for ambient light mitigation have been explored, mainly focussing on the topology of the receiver.

In photodiode-based systems, the potential for saturation and for the induction of a large shot noise component from sunlight, which impairs the SNR, are two significant challenges. The use of optical filters, as well as the employment of logarithmic transimpedance amplifiers (LTA), can aid in mitigating receiver saturation [45]. This provides a large dynamic range to the system, allowing for the amplification of small detected signal currents whilst providing a greater level of protection under high signal levels or ambient light.

In order to increase the SNR in a photodiode-based receiver, researchers in [45] focused on using an adaptive FOV. By mechanically reducing the FOV from ±30° to ±3.75°, ambient sunlight can be excluded from the detector in a broader range of scenarios. This reduction is dynamic and can adapt to the given conditions. The system has been tested in an outdoor link over 50m in various weather and sunlight conditions. The maximum FOV of ±30° was used in overcast conditions (1200-1400 $\mu W/cm^2$) at data rates between 11-48kb/s using Manchester coding. For sunny conditions (51000 $\mu W/cm^2$), similar BER ($<10^{-3}$) levels could be reported when reducing the FOV to ±3.75°.

Nevertheless, by reducing the FOV to small values, the link will be more susceptible to connection loss due to sudden movements of the source-receiver. This is especially prevalent in short-range scenarios, where movements by the source-receiver (e.g. changing lanes or on curved roads) induce a large change in the angle of incidence onto the receiver. Reduction in the FOV will therefore reduce the mobility and reliability of the system, overall limiting its practicality.

Optical filters can significantly improve the robustness by rejecting ambient light outside of the selected communication wavelength band. As such, some VLC systems employ short-pass filters to reject unwanted IR components of ambient light [8, 10]. As around 60% of the power of ambient sunlight (see Figure 2) lies within the visible spectrum, narrow bandpass filters that also cut out unwanted components of the visible range could improve noise rejection [46, 47]. However, there is a limited discussion in the literature of the use of bandpass filters for noise rejection in the automotive environment.

The primary use of bandpass filters in the literature is to increase channel bandwidth, especially for links employing white light LEDs, where the use of a bandpass filter in the blue region (450nm) is relatively common [8]. This removes the slower yellow phosphor components used to generate the white light spectrum [46, 47]. Consequently, the communication channel has a higher intrinsic bandwidth, as it uses the faster blue component emitted by the die of the white LED. Overall, it appears as if bandpass filters have not yet been used to their full potential and could be a valuable part in attempts to demonstrate sunlight-robust outdoor VLC.

Another scheme for ambient light mitigation is presented in [48], where the properties of linearly polarised light are used. The system employs two transmitter-receiver units, each facilitating orthogonally polarised links. When transmitting a binary signal, the "1"-level is

sent using a link with 0° polarisation, whereas the "0"-level is transmitted using the link polarised at 90°. Both receivers are connected to a differential amplifier that subtracts the signals and thereby reconstructs the initial bitstream. Due to the employment of linear polarisation filters in front of each receiver, 50% of ambient light is rejected in each receiver and therefore reduces the contribution to the system noise. For the initial generation of the polarised signals, one consideration regarding this system is that the polarisation filters in front of the transmitters significantly cut the signal power. This, in turn, reduces the SNR in each channel. However, the transmission of an active "0" signal allows for the toleration of a lower SNR. This technology has not been tested in an outdoor scenario, so its actual robustness benefit is yet to be confirmed.

### 1.2.4 Summary

The research outlined so far shows that data rate and communication range are intrinsically linked. Each critically relies on the SNR of the link, which is greatly affected by ambient light and adverse weather conditions.

A practical system for operation within the automotive environment needs to meet the outlined requirements regarding data rate and range, whilst being robust to weather and ambient light. Thus, the employed link requires a high SNR, facilitated by a high signal power in conjunction with effective noise mitigation strategies.

Regarding practical employment, the system topology has to consider its application in a mobile environment, where the alignment of the optical path is challenging, and the system complexity has to be kept to a minimum.

The employment of imaging sensors provides a high level of robustness to ambient light and allows for spatial separation of multiple sources. However, conventional sensors are limited by their frame rate, which limits the achievable data rate significantly. Photodiode-based

detectors have a much higher bandwidth, allowing for higher data rates in the optical link. Strategies for the mitigation of ambient light, as well as for enhancing the mobility required in the automotive environment, are crucial challenges for PD-based links.

Within the field of automotive OWC, several challenges need to be addressed before the technology is sufficiently practical to implement in the automotive environment. These are as follows [8]:

1. Increasing the maximum link distance and data rate – Providing communication over typical inter-vehicular distances whilst allowing for the transmission of safety-critical data, with the potential extension to multimedia applications.
2. Mitigation of adverse weather conditions – Creating a robust communication system which can tolerate signal attenuation induced by fog, snow, rain etc.
3. Maintaining a link in a dynamic environment – Increasing the mobility of a communication link to account for the changing positions of transmitters and receivers.
4. Ambient light mitigation – Creating a robust link which can operate in high ambient light conditions subject to rapid change.

Of these challenges presented, one of the highest importance, and the focus of this thesis, is that of ambient sunlight mitigation. With effective mitigation, both the mobility and link performance could be significantly improved due to noise reduction.

## 1.3 AUTOMOTIVE OPTICAL COMMUNICATION AT 1400NM

Ambient sunlight, both direct and diffuse, is the dominant ambient light component for outdoor optical communication. The solar irradiance is not uniformly distributed with wavelength, as seen in the Air Mass 1.5 sunlight spectrum in Figure 1 [49]. In the region between 1350 – 1410nm, the sunlight spectrum is severely attenuated. This is due to absorption by water as the sunlight passes through the atmosphere [50]. Compared to the 450nm wavelength used in conventional "white light" VLC systems, ambient light is reduced dramatically in the 1400nm band.

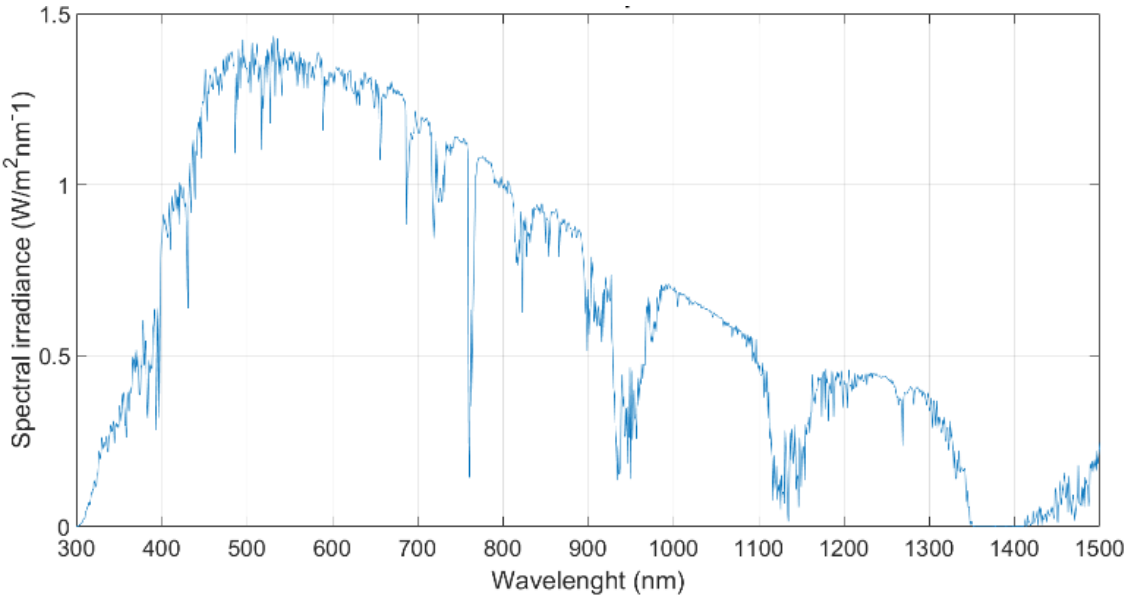



*Figure 2: UV-Visible-NIR region of Air Mass 1.5 Spectrum [49].*

From the Air Mass 1.5 spectrum data, it is possible to estimate this ambient noise benefit. Table 2 shows the power ratio of ambient light passing through a set of ideal optical bandpass filters in the 1400nm region relative to an ideal filter of the same bandwidth centred at 450nm.

*Table 2: Power ratio (dB) of various filters relative to 450nm filter with a 12nm optical passband.*

| Centre Wavelength (nm) | Filter passband (nm) | Power ratio (dB) |
|---|---|---|
| 1350 | 12 | -16.3 |
| 1360 | 12 | -46.7 |
| 1375 | 50 | -28 |
| 1400 | 12 | -32.1 |
| 1400 | 25 | -28.9 |
| 1400 | 50 | -18 |
| 1420 | 12 | -18.3 |
| 1425 | 50 | -10.3 |

These initial estimations in Table 2 suggest that using a communication system based on the 1400nm channel could offer a significant ambient sunlight noise reduction over using a 450nm channel.

## 1.4 THESIS CONTRIBUTION AND STRUCTURE

The outline of this thesis is as follows:

**Chapter 2** discusses the development of a link budget model for assessing the practicality of a 1400nm link versus that of a visible alternative at 450nm. In addition, different receiver topologies are explored using both photodiode and imaging sensors. The results from these models indicate that a 1400nm system could provide a communication link which has a higher level of sunlight immunity and could therefore improve maximum link distances and data rates compared to visible photodiode-based systems.

**Chapter 3** explores the development of a hybrid LED, to provide a 1400nm channel alongside a visible communication channel, and illumination in a single, small form factor package. This chapter explores the fabrication of such devices using PbS quantum dots to convert a portion of the emitted visible radiation to 1400nm. A device is fabricated, and proof-of-concept links implemented operating at 1.75Mb/s at 1400nm and 41Mb/s at 450nm using the same transmitter.

**Chapter 4** discusses the development of a dedicated 1400nm transmitter using commercially available InGaAsP LEDs, including the layout of the associated electronics for driving the LED sources. The results of the communication testing of this system over long ranges (1.25-5m) and in the outdoor environment are presented and discussed in the context of the results obtained using the hybrid LED.

**Chapter 5** explores the potential enhancement of the receiver side of a 1400nm link by the use of a fluorescent concentrator. A particular focus is given to the initial steps towards the fabrication of different shapes of these optical devices using a 3D printer. As a proof-of-concept for this new fabrication procedure, the signal gain of a visible fluorescent concentrator is experimentally assessed. In addition, the fabrication method was extended to PbS quantum-dot based NIR fluorescent concentrators to be used within the receiver of the proposed 1400nm link system.

## 1.5 KEY CONTRIBUTIONS OF THIS THESIS:

The main aim of this thesis was to develop elements of a novel communication system to enable mitigation of ambient sunlight in outdoor applications. Key contributions of this thesis are:

1. The design and development of a custom-built hybrid LED, which facilitates two optical links in parallel, one of which is at 1400nm and was tested under high ambient light conditions. To the best of the author's knowledge, this is the first time that both visible and NIR communication links (1.75Mb/s at 1400nm and 41Mb/s at 450nm) have been facilitated within the same source.
2. A communication link facilitated without saturation in an outdoor environment in daylight conditions, facilitated by a 1400nm transmitter developed from

commercially available parts. This provided evidence as to the feasibility of a sunlight-robust optical communication link.

3. 3D printing a working fluorescent concentrator which provided a signal gain of 4. This served as a proof-of-principle to demonstrate the power of a novel, 3D-printing-based fabrication technique to produce FCs with custom topologies and configurable fluorescence properties.

## 1.6 PUBLICATIONS

(1) Hybrid LEDs for Automotive Communication. J Farmer, D Gregory, R Singh, H Chun, G Faulkner, D.C O'Brien and A Watt. ***Currently under review at the IEEE Journal of Lightwave Technology (JLT)***

(2) A Qualitative Study on the Multi-Domain Suppression of Ambient Light in Visible Light Communication Transceivers. M Yousuf, Z Dawy, A Bermak, J Farmer and D.C O'Brien. **Currently being drafted**

# 2. CHAPTER: MODELLING OF AUTOMOTIVE OWC LINKS

## 2.1 INTRODUCTION

As discussed in Chapter 1, a communication system for autonomous and semi-autonomous vehicles could utilise automotive lighting to facilitate optical links. Although employing existing infrastructure, the primary issue with such a system is that using visible light as a communication medium is highly susceptible to sunlight noise. Using 1400nm as a communication wavelength could provide robust links to ambient sunlight compared with visible links. This chapter focusses on creating a model to quantify this effect and assess the practicality of using 1400nm versus visible links in the automotive environment.

In the following sections, each of the system components and their representation in the model are explained, then link budgets, noise models, and signal to noise ratios are derived. Given the absorption of light in the 1400nm wavelength region by water, the model primarily focusses on simulating different weather conditions with regards to the water content in the atmosphere, allowing for a comparison of visible and 1400nm links. Additionally, the ambient light level is varied in the model to simulate direct sunlight through to night-time conditions. The simulations in this chapter were implemented into a custom MATLAB script, generating Bit Error Rate (BER) contour plots, which were used to determine maximum communication performance.

## 2.2 METHODOLOGY

### 2.2.1 Modelled components

***Basic Equations for link budget modelling***

To assess the effectiveness of various communication links, a link budget model was developed. Figure 3 shows the system [51]. Modulated light from a transmitter, e.g. daylight running lights, propagates to a receiver, which is within the illumination pattern of the lights.

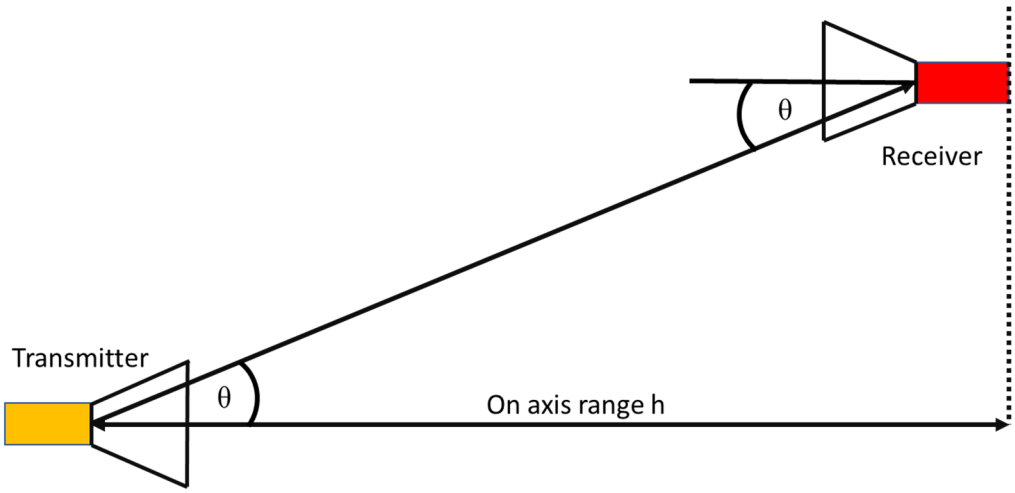



*Figure 3: Link model diagram [51].*

The power falling onto the receiver of a VLC link is given by Equation 1 as follows [51]:

$$\begin{cases} P = \dfrac{(n+1)}{2\pi}\cos(\theta)^n \cos(\theta/h)^2 \, A_{coll} P_{total} \quad (1) \\ \quad where\ n = \dfrac{\log(0.1)}{\log(\cos(\theta_{90\%}))} \quad (2) \end{cases}$$

Where $A_{coll}$ is the collection area of the receiver, $P_{total}$ is the total power of the source, $h$ is the on-axis range between the source and receiver, $\theta_{90\%}$ is the angle from the normal of the source to where the intensity falls by 90% of the maximum value, which is assumed to be half the LED beam angle, and $n$ is the Lambertian order which is related to $\theta_{90\%}$ by (Equation 2) [51]. From the power calculated and the sensitivity of the receiver, the signal current and therefore the SNR for a link can be determined.

***Transmitter/ Source***

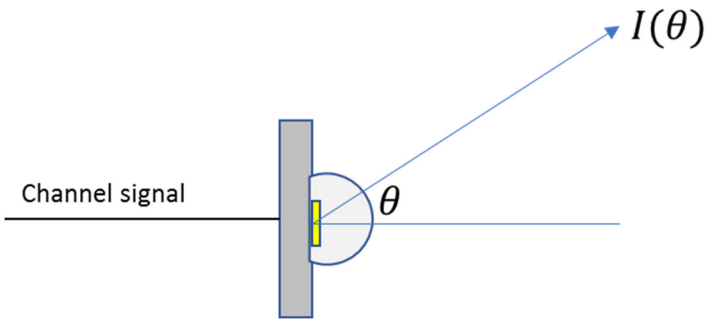



*Figure 4:Optical Transmitter for VLC [51].*

Figure 4 shows an optical transmitter. In this model, the optical transmitter is assumed to be an LED and therefore, a Lambertian source whose intensity is given by Equation 3 [51].

$$I = I_0 \cos^n(\theta) \quad (3)$$

Where $I_0$ is the maximum intensity (W/Sr) [51].

Simulations within this work were performed using three different light sources: brake lights, headlights and daylight running lights. A 1400 nm equivalent of the daylight running light served as a source for the 1400nm channel. The parameters of these sources used in the model can be found in Table 3.

To calculate the SNR for an optical link, the total source power $P_{Total}$ needs to be estimated from the emission spectrum data and luminous flux of the sources considered. The total power generated by the sources is given by Equation 4.

$$P_{Total} = \frac{L}{\int S(\lambda) y(\lambda) d\lambda} \int_{\lambda_1}^{\lambda_2} S(\lambda)\, d\lambda \quad (4)$$

$$y(\lambda) = 1.019 e^{-285.4((\lambda/1000)-0.559)^2} \quad (5)$$

Where $\lambda_1$ and $\lambda_2$ are the lower and upper limits of the optical bandwidth of the channel (nm). $S(\lambda)$ is the relative emission intensity of the source at a given wavelength (a.u.), $L$ is the luminous flux of the source and $y(\lambda)$ is the photopic curve equation [52].

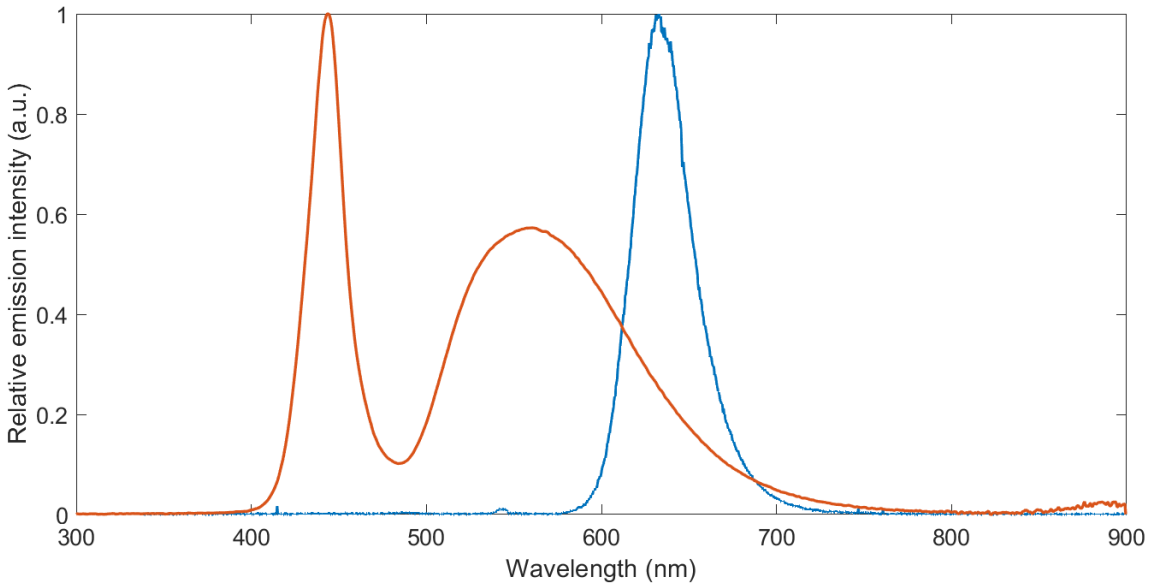



*Figure 5: Relative emission intensity against wavelength for white and red LED sources used in the model.*

To determine $P_{Total}$ for the modelled sources, the relative emission intensity from typical white and red LEDs (see Figure 5), are scaled to fulfil the luminous flux requirements for vehicle lighting [53, 54]. The spectra in Figure 5 were acquired using an Ocean optics OCEAN FX visible spectrometer with a QP400-2-SR-BX fibre and a CC-3-UV-S cosine corrector.

The optical bandwidth used to model the communication channels in this chapter is 12nm. For the brake-light source, the signal power was calculated over 624nm-636nm, and 444nm-456nm for headlights and daylight running lights, respectively. The 1400nm source was modelled to have the same power as calculated for the daylight running lights, within its 12nm optical bandwidth. All calculated powers can be found in Table 3, with all other source parameters.

***Photodiode Receiver***

Figure 6 shows a typical Photodiode-based (PD) receiver, modelled in this chapter. Incident light passes through a bandpass optical filter increasing the system robustness to noise by

reducing the broad sunlight spectrum transmitted to the receiver whilst allowing the signal's optical spectrum to pass. This light is collected by an optical concentrator and focused onto a photodetector. Once the signal is converted to a current, it is then amplified by a transimpedance amplifier [51].

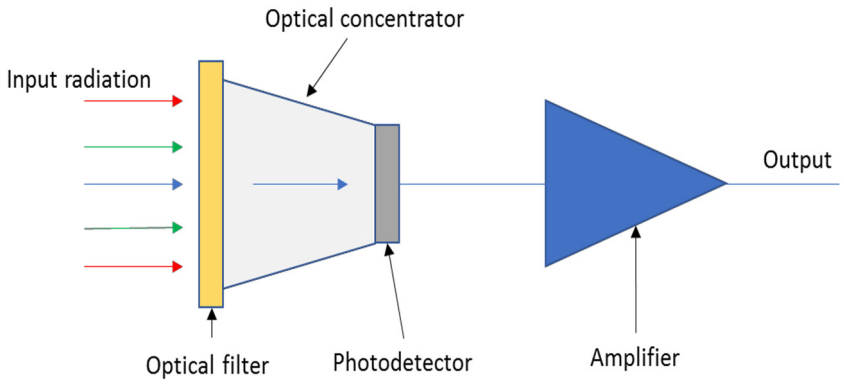



*Figure 6: Diagram of a typical photodiode-based VLC receiver [8].*

*Optical Concentrator*

The area and bandwidth of a photodiode receiver share an inverse relationship due to the area dependence of the capacitance of the photodiode [51]. It is desirable to increase the bandwidth for a system to achieve maximum data rates while maintaining the largest area possible for power collection. To increase the effective area while maintaining a particular bandwidth, an optical concentrator can be employed. However, this comes at the cost of reducing the field of view of the system.

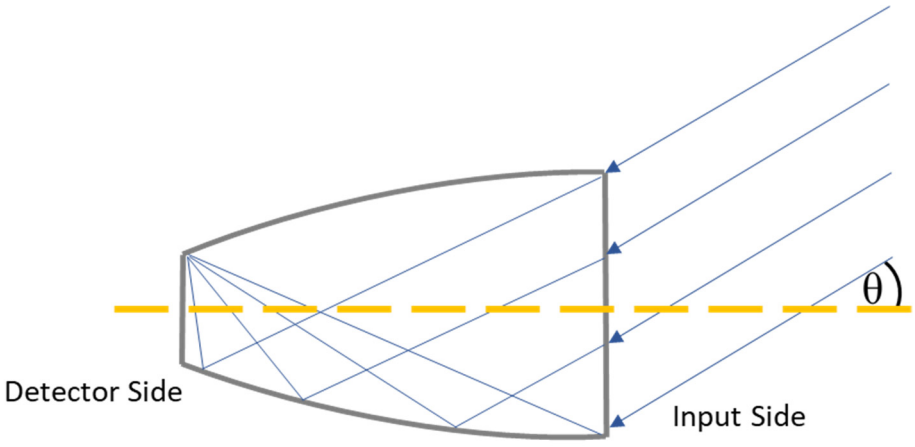



*Figure 7: Diagram of a Compound Parabolic concentrator (CPC), redrawn from [61].*

A compound parabolic concentrator is a non-imaging optical element which captures light with an incident angle smaller than the acceptance angle θ (Figure 7) and internally reflects it to the narrow end where it is collected by the detector [51]. The effective area of the CPC is given by Equation 6 below [51].

$$A_{coll} = KA_{det}(\frac{n_c}{\sin(\theta)})^2 \quad (6)$$

Where $A_{coll}$ is the collection area, $A_{det}$ is the detector area, $n_c$ is the refractive index of the CPC, $\theta$ is half the field of view (FOV), and *K* is a constant, linked to the efficiency of the concentrator [51]. The model assumes that *K* is a typical value of 0.5.

*SNR model*

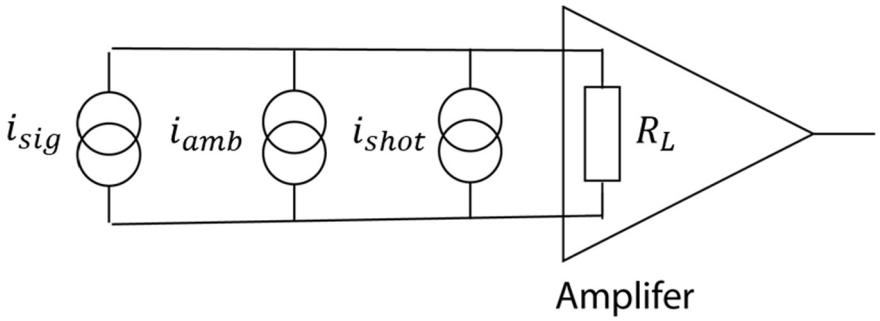



*Figure 8: Equivalent circuit of a photodiode with amplifier. Where $i_{sig}$ is the signal current, $i_{shot}$ is the shot noise components of the signal and $i_{amb}$ is the shot noise induced by ambient light [51].*

Figure 8 shows a circuit model of a typical photodetector/amplifier receiver frontend. To model the SNR of a link, the equivalent circuit of the photodiode receiver must be examined to determine the signal and noise sources present within the model [51]. The SNR for this photodiode receiver is given in equation 7.

$$\begin{cases} SNR = 10\log_{10}(\frac{i_{sig}^2}{i_{Noise}^2}) \quad (7) \\ i_{sig} = RP \quad (8) \\ i_{shot}^2 = 2ei_{sig} \quad (9) \\ i_{Noise}^2 = (\, i_{shot}^2 + 2ei_{amb} + i_a^2)B \quad (10) \end{cases}$$

The SNR, as defined by Equations 7-10, takes into account the signal current received, and various noise sources. $i_{sig}$ is the signal current generated at the receiver and is expressed by Equation 8, where R is the responsivity of the detector in the wavelength region of interest (A/W), and P is the collected power at the receiver (Equation 1). As the optical bandwidths examined in this work are small within the simulations, the detector responsivity is assumed to be constant across the optical bandwidths of interest.

The overall noise $i_{noise}$ contains three components: The signal current shot noise ($i_{shot}$) induced by $i_{sig}$ is defined by Equation 9, where $B$ is bandwidth (Hz) and e is electron charge of $1.6 \times 10^{-19}\ C$. Secondly, there is a current noise $i_a$ which is intrinsic to the receiver amplifier connected to the photodiode. Finally, the largest of the noise sources is typically the shot noise generated by ambient light in daylight conditions. As photodiode receivers are typically AC coupled, the ambient current $i_{amb}$ generated is blocked within the system, but the shot noise generated by this current is not. From summing these noise contributions (Equation 10), the SNR can be calculated (Equation 7).

***Imager Receiver***

As explained in chapter 1, in addition to photodiode based optical communication CMOS (complementary metal oxide semiconductor) imagers are increasingly being investigated as VLC receivers [8, 16, 17, 55-56]. One reason for this is that CMOS imagers are now being employed as sensors around vehicles for video surveillance and parking assistance [17]. Such receivers could be useful for optical communication as they can receive data from multiple sources without interference. In addition, an imaging receiver can also spatially separate sources from direct ambient light, thereby increasing link robustness [8]. Despite this ambient light benefit, conventional imaging sensors can only provide frame rates around 50Hz, limiting data rates achievable, as opposed to the 10s of Mb/s possible with a single-pixel photodiode receiver [8]. Custom imagers, with higher potential data rates, can be

implemented but these are expensive and complex [8]. This section presents the modifications made to the model to characterise the link budget for imager based optical communication, allowing for comparison with photodiode-based receivers.

*System optics*

For an imaging receiver, the collection area at the aperture is given by Equation 11 [57].

$$A_{coll} = \frac{A_{imager}}{4f\#^2 \tan\left(\frac{FOV}{2}\right)^2} \quad (11)$$

Where $A_{coll}$ is the collection area of the receiver, $A_{imager}$ is the area of the imager, $f\#$ is the f-number of the receiver lens and FOV is the Field-Of-View of the imaging receiver [57].

*Ambient light mitigation*

Figure 9 shows direct ambient light and a signal source incident upon an imaging receiver. This demonstrates a key advantage of using an imager as a VLC receiver, as it can resolve multiple signal sources from one another and direct sunlight. This is due to the effectively collimated sources being focused to different parts of the imaging plane. As such, direct ambient light has not been considered in the imager model. Despite this, an imager is affected by diffuse ambient light which, being Lambertian, will be spread evenly across all pixels.

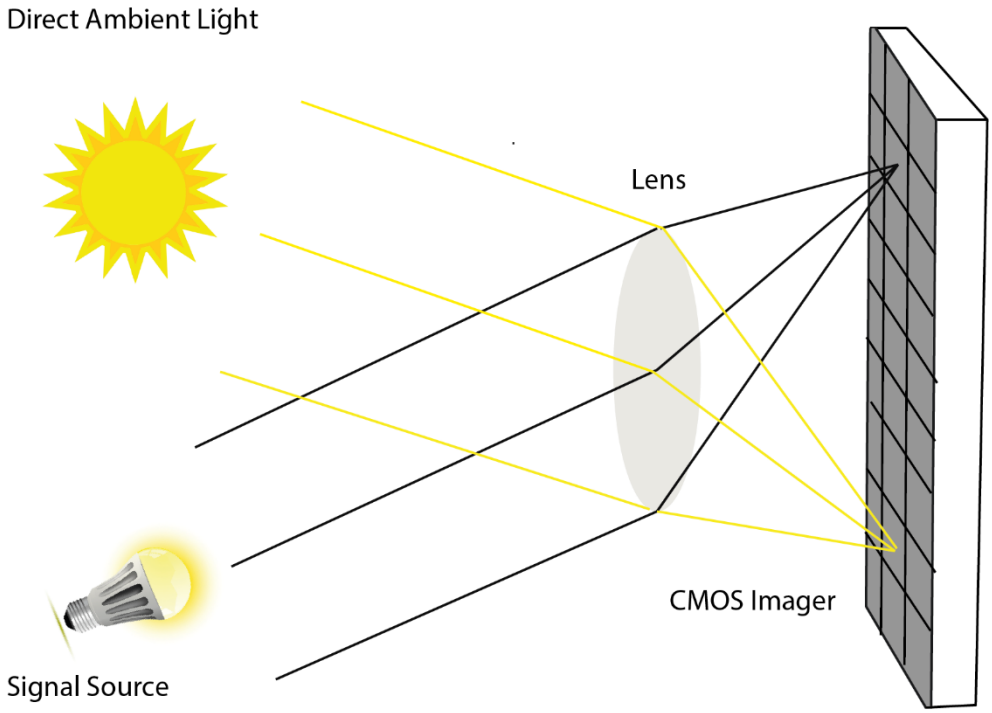



*Figure 9:Diagram of imaging receiver with direct signal and noise sources.*

*SNR model*

For evaluating the performance of an imaging receiver, the SNR needs to be considered by examining the noise sources present, including diffuse indirect ambient light, signal shot noise and pixel read noise. The SNR for a multiple pixel receiver is given by Equation 12 [58].

$$SNR = 10log_{10}\left[\frac{(\frac{i_{ph}}{B})^2}{\frac{e}{B}\left(i_{ph} + i_{dc} + \frac{i_{amb}}{m}\right) + (e\sigma_r)^2}\right] \quad (12)$$

Where $i_{ph}$ is the photocurrent collected by a pixel, $B$ is the bandwidth of the imager system and is assumed that $B = {}^{1}/_{t_{int}}$ where $t_{int}$ is the integration time of the pixel [58]. $i_{dc}$ is the dark current of the pixel, $i_{amb}$ is the current induced by indirect ambient light across the entire imager, $m$ is the number of pixels, $\sigma_r$ is the read noise in electrons and $e$ is electron

charge [58]. This model assumes that the imager electronics are ideal and do not require any time to process the signal from the imager pixels and that a global shutter is used.

*Saturation modelling*

A critical parameter which a CMOS pixel has is known as the full well capacity. This is the maximum amount of charge held within the pixel before it becomes insensitive to light incident upon it. At this point, the pixel is said to have saturated and requires resetting.

Saturation imposes the minimum communication distance possible between transmitter and receiver due to the increase in signal photons at the imager as the link distance is decreased. The model includes the condition for a pixel to be saturated, which occurs when the charge collected during one frame exceeds the full well capacity of the pixel as set out in Equation 13 [58]:

$$i_{ph} > [eB(Q_{Full\,well}) - i_{dc}] \quad (13)$$

Where $Q_{Full\,well}$ is the full well capacity of a pixel in electrons and $i_{dc}$ is the dark current [58]. When the capacity is reached, the imager pixel is saturated, and no communication can occur.

### 2.2.2 Ambient light noise

In order to incorporate ambient sunlight into the model, spectral data for sunlight (NREL Air Mass 1.5 spectrum) was used, as shown in Figure 2. Within the model, it was essential to simulate different sunlight illuminance levels; therefore, the spectrum needed to be adjusted for varying conditions. Equation 14 was developed to estimate the sunlight power over a fixed optical band.

$$P_{amb} = \frac{Lux \times A}{\int \varphi(\lambda) y(\lambda) d\lambda} \int_{\lambda_1}^{\lambda_2} \varphi(\lambda)\, d\lambda \quad (14)$$

$$y(\lambda) = 1.019e^{-285.4\left(\left(\lambda/1000\right)-0.559\right)^2} \quad (15)$$

$$i_{amb} = RP_{amb} \quad (16)$$

Where $P_{amb}$ is the sunlight power at the receiver in a fixed optical band, $Lux$ is the illuminance level (lux) of the sunlight, $A$ is the collection area of the receiver optic, $\lambda_2$ and $\lambda_1$ are the upper and lower wavelength bounds of the region of interest, $y(\lambda)$ is the photopic curve equation and $\varphi(\lambda)$ is the spectral irradiance of the sunlight spectrum $(Wm^{-2}nm^{-1})$[52]. Using Equation 16 and the detector responsivity R in the optical band of interest, the current induced to the receiver by ambient light $i_{amb}$ can be calculated.

From this, the sunlight conditions were modelled from night (0 lux) through overcast (1000lux) and typical daylight (10,000lux) to direct sunlight (100,000lux) [59]. The ambient sunlight photocurrent received at the detector is determined by multiplying the sunlight power by the sensor's responsivity over the optical bandwidth considered. For the results in this work, the optical bandwidth is small; therefore, a fixed value for responsivity can be assumed.

### 2.2.3 BER using NRZ-OOK

For the models, data transmission using Non-Return to Zero On-Off keying (NRZ-OOK) was assumed. From [60], the BER can be expressed in terms of the SNR through Equation 17.

$$BER = \frac{1}{2} erfc\left(\frac{1}{2\sqrt{2}}\sqrt{(10)^{\frac{SNR}{10}}}\right) \quad (17)$$

Where SNR is in dB and erfc is the complementary error function [60].

### 2.2.4 Modelling of water in the optical path

Water can affect the optical transmission within a link in several ways: Scattering is induced by droplets of water in the air, resulting from rain or fog. There is an additional absorption component attenuating the 1400nm link, which is induced by any form of water in the optical path. This is assumed to have a negligible effect on the 450nm link.

***Attenuation by Fog***

Scattering in foggy conditions is described by the Beer-Lambert law as can be seen in Equation 18 [51].

$$p = p_0 e^{-\beta_f x} \quad (18)$$

Where $p$ is the received power through fog, $p_0$ is the power received without fog, $x$ is the distance from the source to the receiver and $\beta_f$ is the extinction coefficient of the attenuation medium (fog) [51]. Modelling the extinction coefficient $\beta_f$ for fog has been a challenge that has been addressed using the Kim model, as shown in Equation 19 [34].

$$\beta_f = -\frac{3910}{V}\left(\frac{\lambda}{550}\right)^{-\varsigma} \quad (19)$$

Where $V$ is the visibility distance in meters and was assumed to be equal to $500m$, which is regarded as a moderate fog [34, 51]. For $V$≤500m, it has been shown that the attenuation is independent of wavelength and so ς is equal to zero [34].

***Attenuation by Rain***

To model rainfall, the optical attenuation due to the absorption and scattering components needed to be considered. A heavy thundershower is assumed in the model with 25.4 mm/h rainfall and a drop diameter of 5mm as a worst-case precaution [62,63].

The absorption component in the 450nm link was assumed to be negligible. For the 1400nm channel, the transmission ($\tau$) can be expressed in terms of absorption by water using Equation 20 [64].

$$\tau = e^{-\beta w} \quad (20)$$

Where $\beta$ is the extinction coefficient at a particular wavelength which for 1400nm was estimated to be 0.9511 $mm^{-1}$ [65, 66].

The precipitable water *w* in the optical path in rainfall is calculated using Equation 21.

$$w_{rain} = \frac{1000Rx}{3V_{Terminal}} \quad (21)$$

Where $R$ is the rainfall rate (cm/s), $x$ is the link distance (m) and $V_{Terminal}$ is the average terminal velocity of the raindrops (cm/s). This equation was derived by considering that the concentration of raindrops in the air is the rainfall rate divided by the terminal velocity of the raindrops. To calculate the precipitable water in the optical path, the concentration is multiplied by the conical volume enclosing the path (between transmitter and receiver) and divided by the receiver's collection area.

In addition to absorption, rainfall will also scatter the transmitted light. The scattering attenuation coefficient in rain is given by Equation (22) [64]. As the diameter of raindrops are many times larger than that of the wavelengths being used in this model, there is no wavelength dependency on scattering [64]. This equation characterises the scattering attenuation coefficient in terms of the drop diameter $d$ (mm) and rainfall rate $R$ (cm/s). The transmission $\tau$ due to scattering is described by Equation 23 [64].

$$\beta_{rain} = (1.25 \times 10^{-6}) \left[ \frac{R}{\left(\frac{d}{20}\right)^3} \right] \quad (22)$$

$$\tau = e^{-\beta_{rain} x} \quad (23)$$

***Attenuation by water vapour***

The primary distinction between a typical VLC and a 1400nm link is that the latter will experience a significant absorption attenuation due to the water vapour in the air. This attenuation is thus only modelled for the 1400nm link.

The transmission ($\tau$) follows the Beer-Lambert Law and can be expressed using Equation 20. The precipitable water, in this case, is given in Equation 24.

$$w_{vapour} = 10^{-3}\rho x \quad (24)$$

where $\rho$ is the density of water vapour in the atmosphere and x is the length of the optical path (m). The density of water vapour is calculated using Equation 25 [64].

$$\rho = 1322.8\left(\frac{RH}{100T}\right)e^{\left\{\frac{25.22(T-273.16)}{T}-5.31\ln\left(\frac{T}{273.16}\right)\right\}} \quad (25)$$

Where RH is the relative humidity (%) and T is the temperature (K) of the environment the link is operating within [64].

### 2.2.5 Hardware parameters of sources and receivers

***Source parameters***

The values implemented in the model for the transmitters were taken from the World Forum for Harmonization of Vehicle Regulations, part of the United Nations Economic Commission for Europe (UNECE), who provide advisory legislations for modern vehicle lighting. In the regulation for a daylight running light, the minimum permitted horizontal full beam angle is 40° with the luminous intensity emitted by each lamp required to be not less than 400 cd on axis [67]. Daylight running lamps may also not exceed 1200 cd in any direction the lamps are visible [67]. Therefore, the source is modelled as Lambertian with a 40° beam angle and maximum luminance of 455lm, resulting from the maximum 1200cd limit. The light emitted by the lamps must be white, and a 6000k colour temperature LED-

based transmitter is assumed for both daylight running and headlights. The optical spectrum for these white light sources and for brake lights were taken from data displayed in Figure 5.

For brake lights, similar regulations exist, here the full beam angles of 90 degrees and a luminous intensity of 140 cd is assumed, corresponding to a luminous flux of 256 lm [53]. Finally, for headlights, a beam angle of 30 degrees and a luminous flux of 4000lm is used [53]. For all the results shown in the following sections, the link models use two identical transmitters spaced by 1.6m to model typical separation of the various vehicular lighting sources.

*Table 3: Parameters used to model light sources.*

| Parameters | Daylight running lights | Brake lights | Headlights |
|---|---|---|---|
| Beam Angle (degrees) | 40 | 90 | 30 |
| Luminous intensity (cd) | n/a | 140 | n/a |
| Luminous Flux (lm) | 456 | 256 | 4000 |
| Equivalent Power (mW) (optical bandwidth) | 128 (444-456nm) | 600 (624-636nm) | 1121 (444-456nm) |

***Photodiode receiver***

Table 4 shows the photodiode-based receiver parameters to calculate maximum link distances in various light and weather conditions, as outlined in the methodology section. In all results that follow, the data rate is assumed to be equal to the bandwidth of the channel. In the simulation, both Silicon and InGaAs commercially available detectors were considered, with the largest active areas that could be found. Responsivities and capacitances were determined from typical data [68, 69]. This data was then used to estimate the minimum amplifier noise and maximum data rate achievable.

Significantly, for the 1400nm link, the permitted light which passes through the receiver filter must be limited to between 1350-1410nm to achieve the maximum ambient sunlight

rejection. The Field of View (FOV) of a 1400nm link receiver thus has to consider that the passband of an interference filter shifts to lower wavelengths as light hits the filter at an increasing angle of incidence. This relationship is described by Equation 26 [70].

$$\lambda(\theta) = \lambda(0)\sqrt{1 - \frac{\sin(\theta)^2}{n_{eff}^2}} \quad (26)$$

Where $\lambda(0)$ is the lowest wavelength of the filter's passband at a 0-degree angle of incidence, $\theta$ is the angle of incidence and $n_{eff}$ is the refractive index of the filter [70]. Assuming a 1400nm filter with a 12nm passband and refractive index of 2 (Edmund Optics #65-790), the full angle FOV needs to be limited to 50° to maintain the passband in the optimum region.

*Table 4: Parameters used for photodiode simulation.*

| **Parameters** | **Daylight running lights** | **Brake lights** | **Headlights** |
|---|---|---|---|
| Reciever Area ($mm^2$) | 19.6 | 19.6 | 19.6 |
| CPC Refractive Index | 1.5 (Glass) | 1.5 | 1.5 |
| Responsivity (A/W) | 0.95 @ 1400nm (InGaAs)<br>0.3 @ 450nm (Si) | 0.45 @ 630nm | 0.3 @ 450nm |
| FOV (degrees) | 50 | 50 | 50 |
| Optical Filter | 1394-1406nm, 444-456nm | Red | Blue |
| Amplifier noise $pA/\sqrt{Hz}$ | 2 | 2 | 2 |
| NRZ-OOK Data rate | 1 Mb/s | 1 Mb/s | 1Mb/s |
| K | 0.5 | 0.5 | 0.5 |

***Imaging receiver***

The vehicle safety communications consortium consisting of BMW, Ford, VW and others defined preliminary vehicular communication requirements [8]. These requirements are based on the RF standard IEEE 802.11p for wireless access in vehicular environment (WAVE) [8]. The minimum data rate required for high priority safety applications is 9kb/s, and so a 10kb/s target is set for the imager [8]. In order to meet this, high frame rate (FPS) commercial cameras were considered, and the FastCMOS-128X imager was selected, using

the number of pixels, pixel area, full well capacity, dark current and read noise for this imager in the model [71]. For the imaging optics, a FOV of 140 degrees is used as this is typical of a "dash camera" imager found in the automotive environment. The f-number for the receiver lens was set to 1. Table 5 gives an overview of the parameters used to model the link using an imager receiver in this section. The Parameters for the source can be found in Table 1.

*Table 5: Parameters used in the imager model.*

| **Parameters** | |
|---|---|
| Total area ($mm^2$) | 3.69 |
| Pixel area ($\mu m^2$) | 225 |
| Number of Pixels | 128 x 128 |
| Responsivity (A/W) | 0.3 @ 450nm (Si) |
| FOV (degrees) | 140 |
| Optical Filter | 450nm (12nm passband) |
| Dark current ($fA$) | 0.02 (fps = 10kHz) |
| Read noise (electrons) | 30 (fps = 10kHz) |
| Full well capacity (electrons) | 20,000 |
| NRZ-OOK Data rate | 10kb/s |
| f-number | 1 |

## 2.3 SIMULATION RESULTS

### 2.3.1 Brake and Headlight Communication Channels at 450nm

In an initial simulation, the model was configured to generate BER contours for headlight and brake lights-based links for communication via visible channels. The parameters used for the model can be seen in Table 3 and 4.

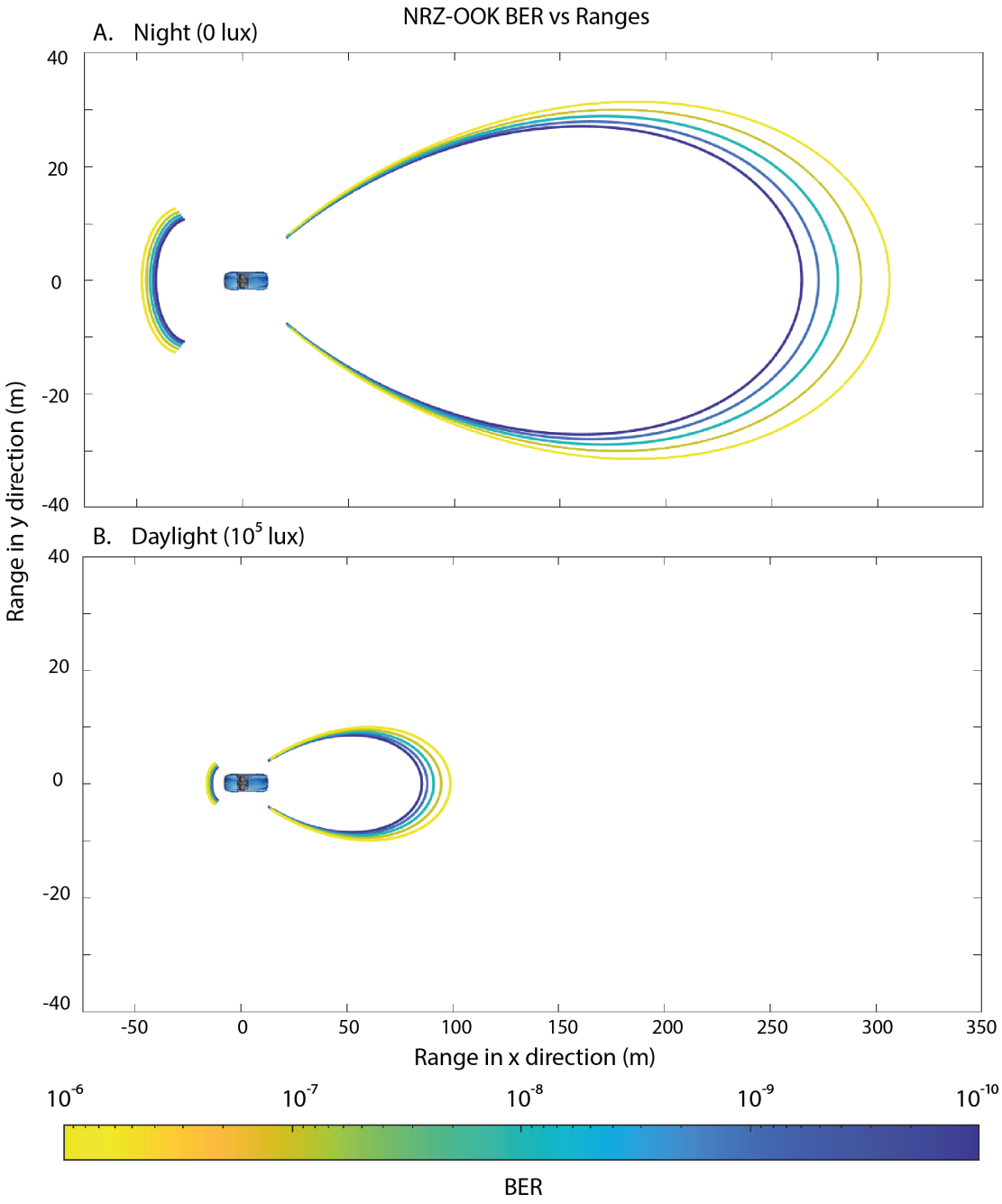



*Figure 10:BER against x and y ranges for brake light link (left) and headlight channel (right) for night and direct sunlight conditions. Car image not to scale in relation to the Figure.*

The contours shown in Figure 10a show different BER levels for a link at a data rate of 1Mbit/s. The $10^{-6}$ contour (yellow) was deemed the upper limit to facilitate a reliable link in all models. In nighttime conditions (0 lux), the headlight channel permits a maximum communication range of approximately 306m, whereas the brakelight channel achieves a maximum range of 48m. Communication with vehicles using the headlights is, therefore, possible over typical inter-vehicular distances (>100m) [8]. However two-way communication is limited by the brake lights to distances of up to approx. 50m.

Figure 10b, shows results in daylight conditions ($10^5$ lux). In comparison to the previous result, the maximum communication range is reduced by approximately 70% to 16m in the brake light channel and 99m in the headlight channel.

Two-way communication is therefore limited to approximately 20m on-axis, restricted by the brake light channel. Using headlights and brake lights, two-way communication at a range up to 100m, the target for such a system, is therefore not feasible, neither in daylight nor in night-time conditions.

### 2.3.2 Daylight Running Light Communication Channels at 450nm and 1400nm

The following simulations aim to investigate differences in performance between a visible 450nm and 1400nm link. For this work, daylight running lights were used as sources as they are designed to be on in daylight conditions.

***Photodiode-based Receiver***

Simulations were performed to analyse the maximum achievable link distances for the various communication systems. Figure 11 shows the simulated BER contours for visible and NIR links in various conditions. Table 6 summarises these results for various ambient light levels and atmospheric water contents for a BER of $10^{-6}$.

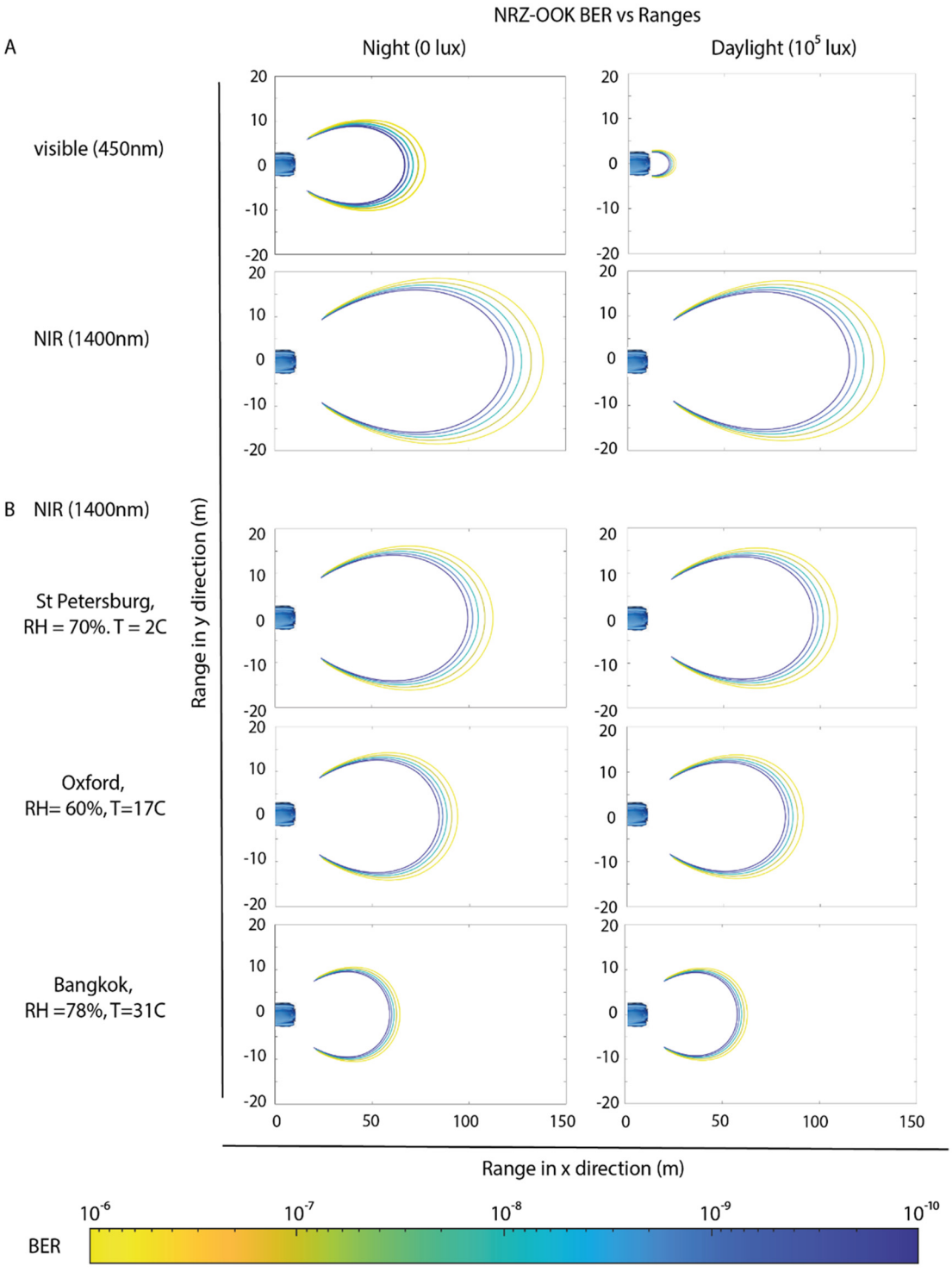



*Figure 11: BER against x and y range for 450nm and 1400nm links under night-time and direct sunlight conditions. (a) 450nm and ideal 1400nm link without atmospheric water present. (b) 1400nm link in conditions of various atmospheric water contents.*

*Table 6:Results of 450nm and 1400nm filtered Photodiode receiver links. Maximum communication distance (m) for BER = $10^{-6}$; RH: relative humidity.*

| | Visible (λ=450nm) | NIR (λ=1400nm) | | | |
|---|---|---|---|---|---|
| | | RH= 0% | St Petersburg RH=70%, T=2 °C | Oxford RH=60%, T=17°C | Bangkok RH=78 %, T=31°C |
| Night-time, 0 lux | 77.5 m | 138.2 m | 112.3 m | 93.7 m | 64.2 m |
| Overcast, 1,000 lux | 66.0 m | 138.1 m | 112.2 m | 93.7 m | 64.2 m |
| Typical daylight, 10,000 lux | 43.4 m | 137.7 m | 111.9 m | 93.5 m | 64.0 m |
| Direct sunlight, 100,000 lux | 24.8 m | 133.4 m | 109.0 m | 91.4 m | 62.9 m |

Figure 11A shows that both the ideal 1400nm and the 450nm links enable communication over tens of meters under night-time conditions. The maximum communication distance of the ideal 1400nm link is approximately 62% larger than the 450nm link. This difference in the range between the links is attributed to different detector responsivities for the two links.

The introduction of sunlight at $10^5$ lux (direct sunlight) decreases the maximum communication range of the visible link, as given by the BER = $10^{-6}$ contour, from 78m to 25m. In contrast, the 1400nm link is only reduced by 3%, from 138 m to 133 m. As expected, the differences between the links are less prominent at lower ambient light levels ($10^3 - 10^4$ lux, corresponding to overcast and typical daylight conditions, respectively). These results suggest that the ideal 1400nm channel is robust to ambient sunlight, which would enable better performance in daylight conditions than visible links at 450 nm can offer.

Different atmospheric conditions were introduced to the model to assess the impact of water vapour in the optical path. The cities of Oxford, St Petersburg, and Bangkok serve as examples of the various climatic conditions found around the world. The local temperature

and relative humidity determine the amount of water vapour contained in the air. In the 1400nm link, the introduction of increasing amounts of water vapour causes a considerable variation in link distance. In the conditions for Bangkok, with the largest amounts of water in the optical path, the maximum link distance decreases from 138m without water present to 64m. Even under these worst-case conditions (RH=78%, T=31°C), the overall maximum distance in daylight conditions is still greater in the 1400nm link than the 450nm. Notably, the robustness to ambient light of the 1400nm link is maintained for all weather conditions, with the communication link distances decreasing by a maximum of 3% compared to night-time conditions (Figure 11B).

***Imaging Sensor-based Receiver***

In this section, a 450nm visible link at 10kbit/s was simulated using an imaging receiver and daylight running lights. Table 7 shows an overview of the calculated maximum and minimum communication distances for reliable links without saturation of the imager. The effects of direct sunlight on the imaging sensor ($10^5$ lux) were not considered in this simulation, as it was assumed mitigated by the nature of the sensor (see Figure 9). Thus, no communication distances for direct sunlight were calculated.

*Table 7: Results of the imager receiver link model in comparison to the photodiode model for a 450nm channel.*

| | Maximum communication distance (m) for BER = $10^{-6}$ | | Minimum distance without saturation (m), Imager sensor |
|---|---|---|---|
| | Photodiode (1Mbit/s) | Imager sensor (10kit/s) | |
| Night-time, 0 lux | 77.5 m | 325.7 | 42.2 |
| Overcast, 1,000 lux | 66.0 m | 311.3 | 42.4 |
| Typical daylight, 10,000 lux | 43.4 m | 249.1 | 42.5 |

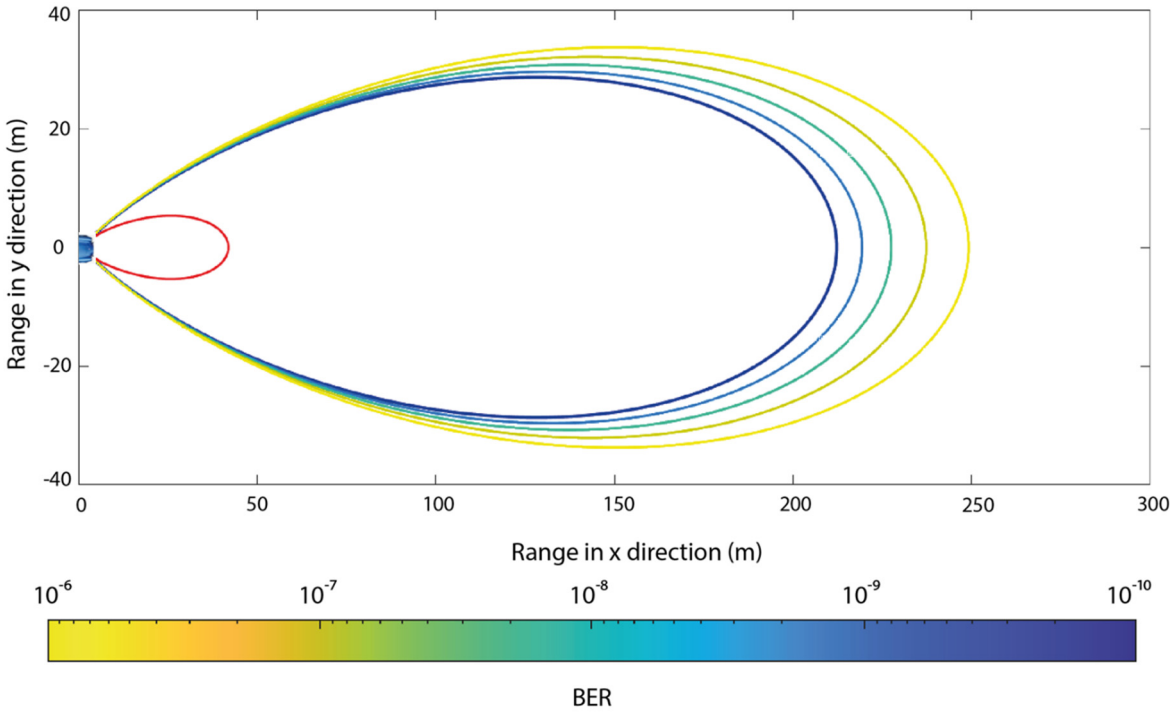



*Figure 12: BER against x and y range for imaging receiver link at 10000 lux with saturation contour (red).*

Figure 12 shows the BER contours generated for the Imaging receiver at an ambient light luminous flux of $10^4$ lux producing a maximum communication distance achievable is 249m. At 0 lux, this distance increases to a maximum of 326m.

Compared to the 450nm Photodiode based link, the overall maximum distance is significantly larger (326m compared to 78m at 0 lux) whilst also providing a greater FOV. Additionally, the simulation results for the imaging sensor suggests greater robustness to sunlight. At $10^4$ lux, the decrease in the maximum achievable link distance is 24% for the imager as opposed to 44% for the photodiode link. Despite this, even under direct sunlight of $10^5$ lux, the 1400nm photodiode link only lost 3% of the maximal link distance.

Despite these advantages, the saturation of pixels is an issue with imaging sensors. Within a communication link, this would limit the minimum distance between transmitter and receiver to provide communication. In the model presented here, this effect was considered, and the minimum distance was simulated. As seen from the red contour in Figure 12 and Table 5, this distance is 42 m at $10^4$ lux with variation in the ambient light level having only

minor effects on this distance. Taken together, this simulation data suggests that communication can be achieved at distances between 42 m and 249 m.

***Attenuation by adverse weather conditions***

*Table 8: Results of blue and 1400nm filtered photodiode receiver links in foggy conditions. Maximum communication distance (m) for BER = $10^{-6}$.*

| | Visible PD (λ=450nm) | Visible imager (λ=450nm) | NIR photodiode (λ=1400nm) | | |
|---|---|---|---|---|---|
| | | | St Petersburg T = 2°C | Oxford T = 17°C | Bangkok T = 31°C |
| 1,000 lux | 66.0 m | 311.3 m | 112.2 (RH=70%) | 93.7 (RH=60%) | 64.2 (RH = 78%) |
| Fog & 1,000 lux RH = 100% | 53.5 m | 163.9 m | 81.1 m | 66.9 m | 51.4 m |
| Rainfall & overcast, 1,000 lux | 66.0 m | 311.3 m | 110.9 m | 92.9 m | 63.9 m |

To further assess the effects of different weather conditions, the model was extended to incorporate rainfall enclosed in the optical path. An ambient light level of 1,000 lux was assumed, corresponding to a typically overcast sky. As shown in Table 8, rainfall affects the maximum achievable link distance in the 1400nm channel by a maximum of 2%. This can be attributed primarily to absorption by the rain in the optical path. For light at 450nm, which is not significantly absorbed by water, only scattering occurs which does not have a measurable effect on the maximum link distance as simulated here.

Similarly, fog was introduced to the modelled links. Table 8 shows the simulation results for foggy conditions at 1000 lux ambient light (overcast conditions). In the visible photodiode-based link, the fog reduces the maximum achievable distance by 19% from 66 to 54m. The maximum link distance in the 1400nm link is decreased by up to 29% compared to solely overcast conditions in Oxford, St Petersburg, or Bangkok. Finally, the maximum

achievable distance for the imaging sensor decreases by 47%, from 311m in overcast conditions to 164m in moderate fog.

The scattering component of fog attenuates a signal independent of the wavelength (within the range of interest to this work). This accounts for the attenuation seen in the 450nm photodiode and imager links and in part at 1400nm. For the latter, the rise in the relative humidity to 100%, as fog is saturated air, increases the absorption of the signal, which further reduces the maximum distance.

## 2.4 DISCUSSION

### 2.4.1 VLC using Headlights and Brake lights

According to the head and brake light communication simulations, the headlight channel provided a large communication range of several hundred metres. It is significantly impaired by ambient light, limiting its range in direct sunlight to approximately 100m. However, the range achievable in the brake light channel limits the overall communication distance. This range is drastically reduced in direct sunlight compared to night-time conditions (48m), lowering the range to 16m.

### 2.4.2 VLC using Daylight Running Lights

***V2V communication at 1400nm***

The significance of the ambient sunlight challenge was demonstrated by initially modelling a 450nm visible link. It was significantly impaired in its performance, reducing the achievable link distances by over 60%. In contrast, the simulation of a V2V link at 1400nm, using sources equivalent to daylight running lights, demonstrated its higher robustness to ambient sunlight. This suggests that using the 1400nm band for communication addresses one of the major challenges currently existing for outdoor optical communication [8].

The robustness benefit of a 1400nm link can be attributed to the absorption of ambient light in this band by water molecules when sunlight travels through the atmosphere. To investigate whether absorption of a communication signal could become problematic on typical inter-vehicle distances, water was introduced in the optical path. Between the most extreme environments, one with a theoretical 0% relative humidity, and Bangkok, which was the modelled condition with the highest water content, the maximum link distance was decreased by 70%. Although the variation is significant between these extreme cases, it is the variation within the local environment which is critical to a 1400nm links performance. Generally, environments will not be subject to such drastic changes in relative humidity and temperature in short time frames. This could mean that the power of automotive 1400nm transmitters could be compensated, depending on, e.g. the time of year, to maintain the same link performance.

In contrast to the different environmental conditions above, which are relatively stable over time, fog and rain can appear in most climate conditions on a short time scale. This makes it more difficult to compensate for and worth being considered in this work. In the simulations, rain only minimally affected the achievable link distances, suggesting that both links are reliable during rainfall.

Upon the introduction of fog, the achievable link distances in the two channels were reduced by up to 28%. Fog affects both channels equally by scattering the signal, along with an additional absorptive component in the 1400nm link due to the high water content of the air. Regarding the absolute performance, the 1400nm link achieves a worst-case maximum communication distance similar to the 450nm link.

***Comparing receivers***

In addition to analysing the effect of using different sources and optical bands for communication, different receiver topologies were evaluated.

The use of an imaging sensor instead of a photodiode as the link receiver allows for a greater communication distance at the chosen data rates, reaching into the hundreds of metres range. Additionally, the imager-based link is also more robust to ambient sunlight than a 450nm photodiode-based link, but still considerably less robust than the 1400nm link. Both receivers performed approximately the same in rain; however, fog seems to significantly affect the imaging sensor.

As seen in the simulation, saturation of the imager pixels is one of the significant limiting issues affecting the practicality of an imaging receiver, as communication below a minimum distance of approximately 42m is not possible., There are three potential solutions to reduce the minimum communication distance:

1. Increase the full well capacity of the imaging pixels: This is dependent on various parameters such as pixel architecture and well depth in addition to the relationship between the pixel area and capacity.

2. Increase the frame rate of the imaging sensor: This may, however, go along with a decrease in the imager resolution, rendering the sensors impractical for vehicle surveillance and possibly decreasing the robustness benefit over using a photodiode receiver.

3. Use adaptive filtering to avoid saturation: This could effectively reduce the signal as the receiver moves closer to the transmitter. The distance over which communication could be achieved without saturation of the receiver could be adjusted in accordance

with conditions and link distance to maintain a robust link. Such adaptive filtering could potentially be achieved with a variable neutral density (ND) filter.

Despite these options to increase the saturation limit, the most significant disadvantage of using an imaging sensor is the limited frame rate of typically around 50Hz, which limits the achievable data rate. Higher frame rate imagers are expensive, and a significant advance in technology is needed to allow low-cost automotive camera systems to provide the required frame rate. Short integration times might, in turn, compromise the quality for video surveillance, as it reduces the number of photons collected per frame.

## 2.5 CONCLUSIONS

The absorption of light by water vapour at 1400nm creates a band where optical links could operate with lower ambient light noise than in the visible region. This has been explored in this chapter by modelling a series of automotive optical communication links, of which the 1400nm link is highly robust to ambient sunlight and rainfall. Such a link could be an attractive part of an optical communication infrastructure for automotive applications, outperforming visible photodiode and imaging receiver-based links in terms of robustness. Despite potentially lower robustness than a 1400nm photodiode link, imaging sensors are commonly deployed in-vehicle surveillance systems, and therefore could be used for V2V communication with minimal costs.

A possible communication solution might combine imager-based visible links for low data-rate long-range applications, with a 1400nm link used for higher rate data transfers, such as map-sharing. In addition, the 1400nm link is intrinsically robust to being saturated by direct sunlight, whilst an imager-based system requires spatial separation and signal processing to

achieve this. A combination of the two approaches might offer increased robustness, as is required for safety-critical information.

The following chapters of this thesis will focus on technologies to efficiently generate and detect the radiation required for such 1400nm links, as well as architectures which can combine the visible and infrared approaches.

# 3. CHAPTER: HYBRID LED

## 3.1 OVERVIEW

As explained in the introduction, the use of 1400nm light for communication could be useful in the automotive environment. Additional sources would need to be added to vehicles to facilitate such a link, increasing complexity and cost. Typically, white light LEDs generate light using a high-efficiency 450nm blue LED covered with a mixture of phosphors which absorb the blue light and emit from green (500nm) to red (650nm) [72]. Such LEDs are employed in automotive lighting in headlights, sidelights and daylight running lamps. This chapter proposes a system incorporating an additional fluorescent material with an emission peak at 1400nm into the white LED already used in automotive lighting systems. This system would have the benefit of generating 1400nm radiation for robust communication, provide an additional visible communication link and illumination for visibility and safety. This chapter discusses the stages of development and testing for such a hybrid LED and reports a proof-of-concept demonstration of such a system.

## 3.2 INTRODUCTION TO QUANTUM DOTS

The main challenge in developing a hybrid LED was to find a 1400nm emitting fluorophore which could absorb in the visible region. After research into various types of conventional fluorescent materials, it was decided to use Lead Sulphide Quantum Dots (QDs), as they can convert visible light into the desired wavelength with a high quantum yield (QY) [73].

QDs are nanocrystals, in this instance constructed of Lead Sulphide semiconductor. At sizes of 3-10nm, they provide 3-dimensional spatial confinement of electrons which is analogous to a particle in box model [74]. As such, this confinement to length scales smaller than the de Broglie wavelength of the electron leads to a quantised energy spectrum [75]. The

quantised energy states allow for defined electronic transitions, and therefore have absorption and emission properties similar to those found in dye molecules or atoms.

As the quantisation and therefore the energy levels critically rely on the confinement, the QD emission properties can be tuned by varying their physical size/diameter [76]. The wavelength emission range of PbS QDs can be varied between 900-1600nm [77]. By growing the dots to an average diameter of 5nm, the emission spectrum peak can be set to approximately 1400nm [78].

An additional feature of PbS QDs is a broadband absorption from 400nm through the visible region. Such a property is due to the semiconductor nature of the QDs. Typically, quantum dots absorb all photons with higher energy than the semiconductor bandgap energy of the QDs [79]. The light causes the electron in the QD to be excited from the valence band to the conduction band, forming an exciton (electron-hole pair) [79]. As the electron is confined within the conduction band, the exciton eventually recombines, leading to light emission at the bandgap energy [79].

The broad absorption characteristics provide the foundation for the use of QDs in the proposed communication system. Most conventional fluorescent materials (mostly organic molecules) show a shift between absorption and emission (stokes-shift) in the region of 20-50nm, which can be attributed to relaxation processes in the molecule after the absorption of the photon, but before the emission takes place. This energy loss is reflected in the shift of the emission towards longer wavelengths [80]. For the application proposed here, a shift from blue light (450nm) to 1400nm is required, which cannot easily be facilitated using conventional fluorophores. The QDs, with their broad absorption throughout the visible spectrum and a precise emission peak at 1400nm, provides the basis for the required shift

into the NIR. Together with their high QY achievable (>40%), this makes QDs well suited for the application outlined in this chapter [78].

## 3.3 Hybrid LED Construction

### 3.3.1 White LED selection

The initial stage for realising the proof-of-concept hybrid LED was to select a white light LED. For optical communication, a high bandwidth together with a high output luminous flux was desirable. In order to maximise the bandwidth, a low LED capacitance is required. This is typically proportional to the LED die area and therefore, the emitter area of the LED.

After conducting a search across multiple LED manufacturers, two LEDs were selected, these having the smallest die area which could be found with high luminous flux. The OSRAM Compact CM and CL LEDs have light emission areas of $0.79mm^2$, and $1mm^2$, respectively, and thus are potentially well suited for high-frequency modulation [81][82].

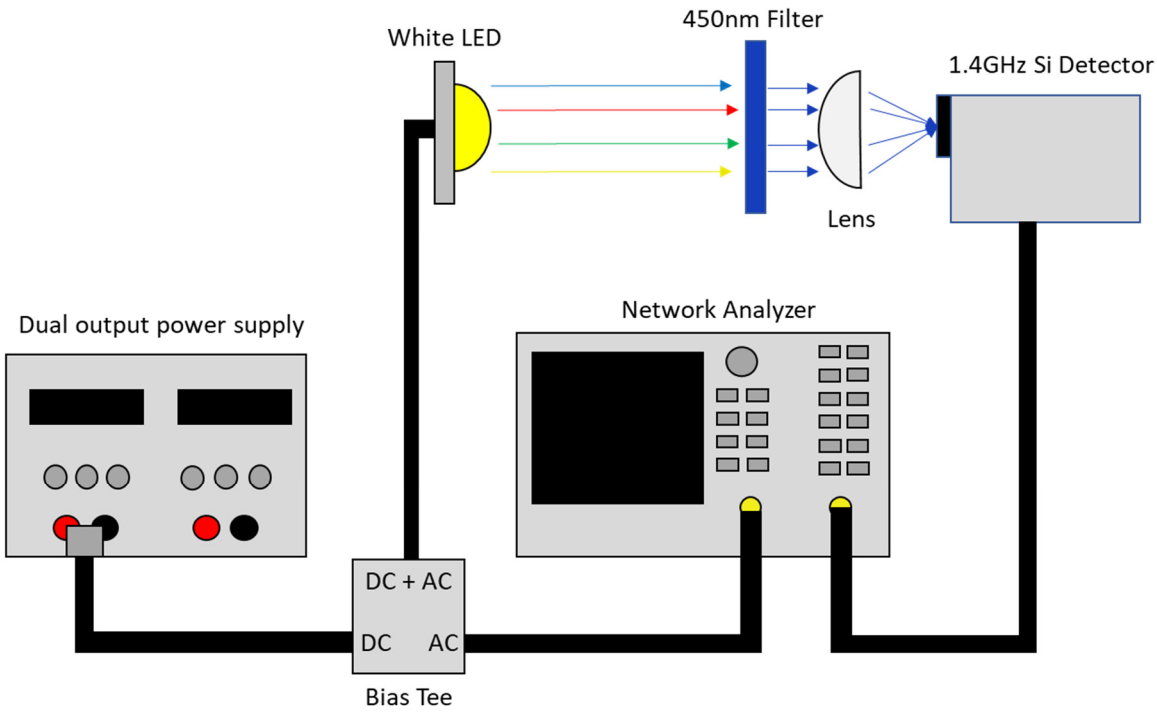



*Figure 13: Diagram of LED bandwidth measurement experimental set-up.*

The luminous flux from the LEDs at 350mA was 100lm (Compact CM) and 150lm (Compact CL), which is high, especially considering their sizes [81][82]. To deal with the heat dissipation of the LEDs, they were soldered to a Metal Core Printed Circuit Boards (MCPCB) (MEODEX France), and then mounted onto an aluminium heatsink for further thermal dissipation and to mechanically mount the devices.

To evaluate the LED bandwidths, an experiment was set-up as can be seen in Figure 13. A Keysight E5061B ENA Vector Network Analyzer was connected to a Mini-circuits ZFBT-4R2GW-FT+ bias tee with low and high-frequency cut-offs of 100kHz and 4.2GHz respectively. This was connected to the LED and supplied with a bias voltage from an Aim-TTi EX752M 75V 2A 300W dual output power supply. The optical signal produced from the LED was passed through a Thorlabs FBH450-10 450nm filter (10nm Full Width at Half Maximum) and collected by a 25mm lens, focused onto a Femto HSPR-X-I-1G4-SI-FS 1.4GHz Si photoreceiver. The Network Analyser collected the received electrical signal.

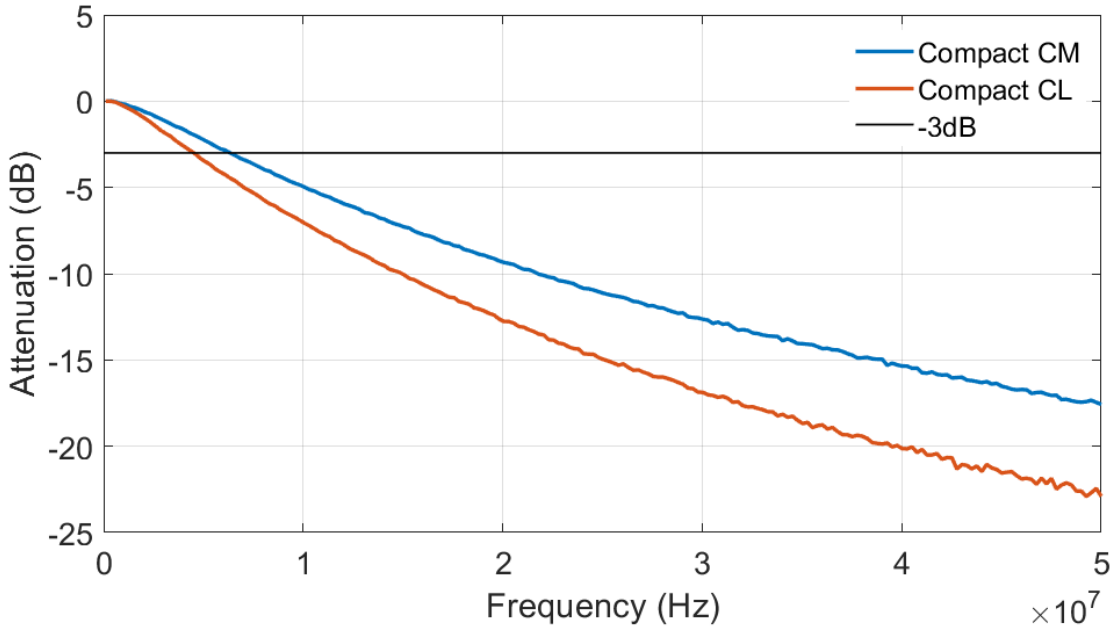



*Figure 14: Attenuation (dB) versus frequency (Hz) for Osram compact CM and CL LEDs with 80mA bias applied.*

To profile the bandwidth, a fixed bias current of $80mA$ was applied to the LEDs. A swept AC sinusoidal signal was injected from the network analyser over a range of frequencies (100kHz-50MHz) with a signal power of -12dBm (158.8mV pk-pk for 50-ohm load). The resulting signal was applied to the LED, and subsequently, the analyser measured the received signal. The result of the measurement can be seen in Figure 14. The -3dB bandwidth of the Compact CM and CL was measured to be 6.34MHz and 4.55MHz, respectively. From these results, the Compact CM was selected as the white light LED for the hybrid LED experiments.

### 3.3.2 PbS QDs

The PbS QDs with oleic acid ligands, used in this experiment were suspended in toluene at a 10mg/mL concentration and were from Quantum solutions based at King Abdullah University of Science and Technology. In solution, the QY was 68% and the emission spectrum Full Width at Half Maximum (FWHM < 140nm) centred at 1410nm as can be seen in Figure 15 [77]. Handled correctly, the emission properties and the high quantum yield were well suited to application within the hybrid LED project.

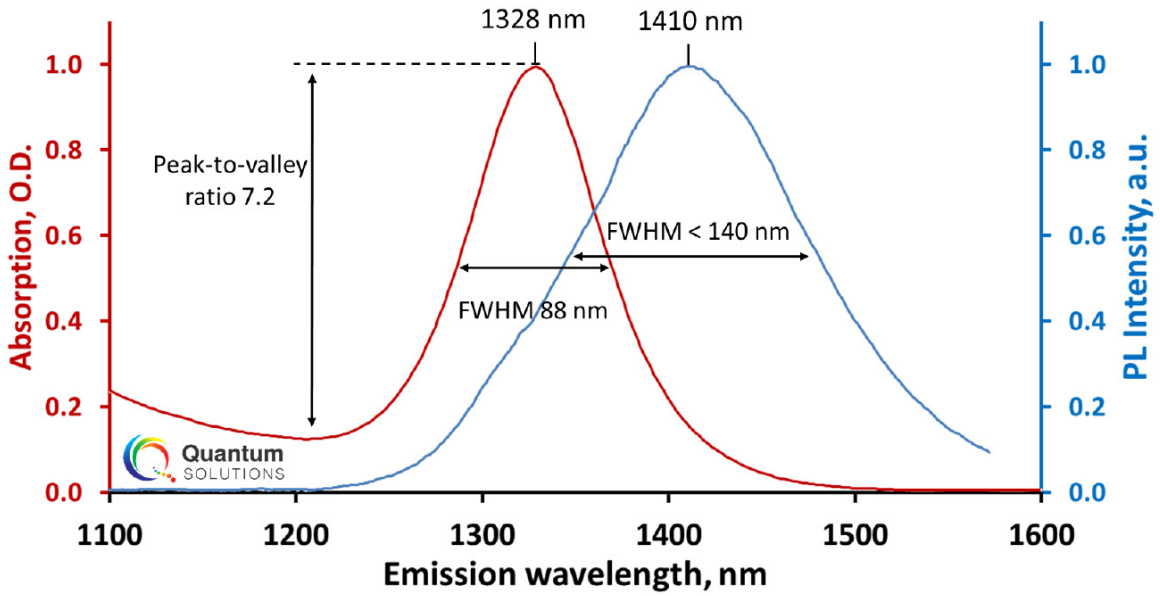



*Figure 15: Absorption and emission spectrum of Pbs QDS in toluene (10mg/mL) [77].*

### 3.3.3 Sample Fabrication

The QDs needed to be encapsulated in solid samples which could be placed in front of the chosen white light LED. This encapsulation will prevent photo-induced oxidative damage to the QDs, which occurs when exposed to light in the presence of molecular oxygen [73]. A suitable incorporation material should provide mechanical stability to the QDs, whilst not interfering with their optical properties. Additionally, the concentration and thickness of QDs in the samples should be optimised in order to maximise conversion efficiency and minimise reabsorption of the converted radiation.

To create the base solution, to which various plastic encapsulants would be added, 2mL of a 10mg/mL solution of 1400nm emission PbS QDs is used. To this, we then added 14mL of acetone and placed the solution in a centrifuge at 4000 rpm for 15 minutes to precipitate the QDs. After 15 minutes, the liquid supernatant was discarded, leaving the solid QDs. To easily incorporate the QDs into the resin, we introduced 100uL of Toluene and vortexed the solution for 10 minutes. Finally, we added an additional 20uL of Toluene and sonicated the solution for 10 minutes. This produced a very high concentration solution ($167\ mg/mL$) with the minimal toluene included, helping protect the QDs from interaction with oxygen in the air and making the solution easier to work.

A silicone mould was created to form the QD samples by which the liquid QD/resin solution could be added and left to cure. The silicone's non-stick and elastic properties allow for easy sample removal after curing. The silicone (negative) mould was created from a 3D-printed positive of the desired shape and size. To fabricate the samples, 0.1mm thick glass 5mm diameter coverslips were added into the mould before pouring the QD solution on top. The samples were then topped with an additional 5mm coverslip to provide two optical surfaces.

***Electrolube UR5634***

Initially, commercially available encapsulation resins were used. The first of these was the Electrolube UR5634 polyurethane resin. This was chosen as it was a water white clear 2-part 1:1 resin, typically used for potting LEDs and obtained from RS. A selection of concentrations was chosen for this test. Into the silicone mould a control (pure resin) was added along with a solution of QD and resin at $0.5mg/mL$, $5mg/mL$ and $50mg/mL$ and left for 24 hours to harden (Figure 16).



*Figure 16: Samples of various QD concentrations with UR5634 polyurethane resin.*

From this fabrication test, there were two main problems. The resin used was very viscous, which, when mixing in the QDs, introduced trapped air within the samples. Attempts were made to degas the samples, but due to the 20-minute gel time of the resin and high viscosity, this had a limited effect. In addition, as can be seen in Figure 16, the QDs are not homogenously dispersed within the samples as the QDs aggregated during the curing process.

***Optic-tec 5001***

A lower viscosity commercial resin which would allow for the escape of a larger amount of trapped air was needed. Optic-tec 5001 was chosen, which was optically clear with a longer gel time of around 1 hour. The first test with the resin was to incorporate it into the QDs in the same concentrations as with the previous resin. Unlike the previous test, this resin failed to mix homogeneously in the liquid phase before curing, which eliminated it from further experimentation using this method of fabrication.

Following this, it was decided to try out a new technique for sample production. Samples were instead fabricated, with the same concentration as the previous experiment, by coating a 5mm coverslip with different concentrations of QDs in toluene. The samples were left until the toluene evaporated, and a solid coating was left on the coverslip. This was then added to the bottom of the silicone mould, and the resin placed over the top of the coverslip, finally placing a coverslip over the resin. On visual inspection, these samples appeared sufficiently homogeneous to test the emission spectrum. From the results, the samples underwent a redshift in the peak emission spectrum from 1410nm to 1460-1480nm.

Furthermore, the FWHM of the spectra from the samples increased from around 140nm to between 360-370nm. One reason for this change in the emission spectrum could have occurred due to the QDs aggregating as the solvent evaporated from the coverslip. In addition, some damage may have been caused by keeping the samples in an air atmosphere, whereby the oxygen and ambient light may have contributed to damages of the QDs.

It was decided from these results that further investigation was required to reduce the redshift observed and as such other methods of fabrication were explored.

***UV-curing Isobornyl acrylate***

Consulting with Quantum Solutions, the supplier of the QDs, the use of Isobornyl acrylate (IBOA) with a photoinitiator (2-hydroxy-2-methylpropiophenone) was suggested based on experiments they had conducted using a very high-power UV source emitting at 365nm with an irradiance of 800mW/cm$^2$. The principle for this approach was to polymerise the encapsulate as quickly as possible, with the QDs incorporated, to reduce the effects of oxidisation and aggregation. As the QDs with oleic acid ligands have a non-polar molecular polarity, an encapsulate with the same polarity is required such as IBOA. This is because the QDs will be soluble in such an encapsulate, reducing the risk for aggregation.

For curing the IBOA samples, the only practical UV emitter we possessed was a Norland OPTI Cure 3 gun with an irradiance of $90mW/cm^2$, measured with a Newport 919P-003-10 Thermophile. An experiment was conducted to attempt to cure the QD/UV resin samples with a low concentration ($1mg/mL$) using the UV gun, but the samples did not cure after half-hour of UV exposure. It was possible however to cure resin only samples in the silicone mould. IBOA and photoinitiator were mixed in the ratio of 20:1 ($1\text{mL}: 50\mu\text{L}$) for this experiment, as suggested by Quantum solutions.

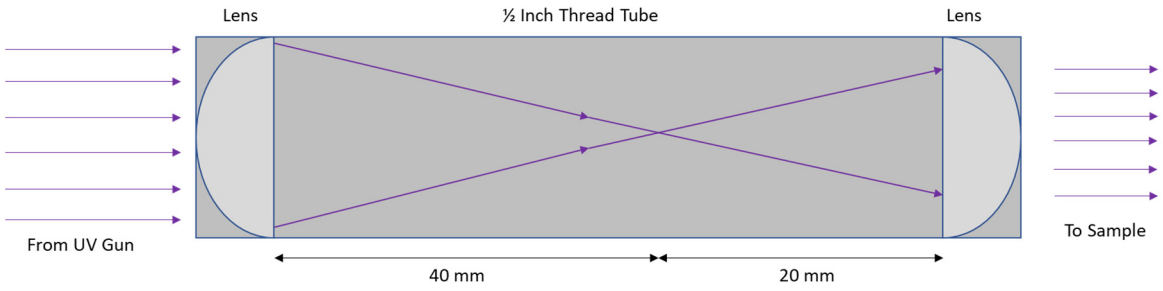



*Figure 17: Diagram of UV Gun optics.*

An idea to resolve the curing issue was to increase the irradiance of the UV gun using an optics system to focus the 10mm aperture of the gun to a 5mm diameter. This was achieved using two ½ inch UV Fused Silica Plano-Convex Lens (Thorlabs), one with a focal length

of 40mm and the other with a focal length of 20mm. The lenses were placed into the lens tube in the configuration as can be seen in Figure 17. Assuming that the UV gun has an irradiance of $90mW/cm^2$ and the output is collimated, the focus irradiance onto the sample would be a maximum of $459\ mW/cm^2$. This irradiance level was judged to be acceptable although short of the irradiance used in the experiment carried out by Quantum Solutions.

To mount the gun onto the optics and protect the user from concentrated UV radiation, a 3D printer surround was created, as shown in Figure 18. The experiment was rerun with the modifications to the UV gun. After several attempts, leaving the same concentration samples to cure under the UV gun for 30 minutes, we were still unable to achieve curing. The amount of photoinitiator was then increased to $150\mu L$ in an attempt to cure the samples. This method still failed to work, possibly due to a lower than modelled UV irradiance.




*Figure 18: Images of UV curer built to cure IBOA/QD samples.*

***Drop coating coverslips***

Throughout the fabrication process described so far, it became clear that making samples in the silicone mould was not practical and did not produce samples of the desired quality. Instead, samples were created by drop coating the 5mm coverslips with the QD-resin solutions for the remainder of the fabrication work.

Using drop coating, several non-polar polymers were examined as an encapsulate for the QDs. These were Polymethyl methacrylate (PMMA), polystyrene, Polyurethane, and polypropylene, which could be employed using the method of secondary dispersion. In addition, a UV curing resin, which is used in Direct Light Projection (DLP) 3D printing, was also considered as it was desirable to cure the samples as quickly as possible to avoid aggregation effects.

Secondary dispersion is whereby a polymer such as PMMA is dissolved in toluene or other solvents, incorporated with the QDs and left to set over approximately one day as the solvent evaporates [76]. From a search of the literature, this method of encapsulation can come with drawbacks such as dramatically reducing the QY achievable (by up to 70% [76]) and typically induce a redshift in the emission spectrum compared to before the encapsulation [78]. This is accredited to the effects of oxidation and aggregation of the QDs during the dispersion process [76]. These changes in optical properties are undesirable for this work. However, it was decided to test using the secondary dispersion technique as it was a conventional fabrication method used within the QD field.

DLP resins which are used in resin-based 3D printing, are constructed of a combination of monomer and oligomer combined with photo-initiator and photo absorber [84]. Most DLP resins used are predominantly non-polar, which suggested that the QDs would be soluble within most of these resins [75]. Due to the fast-curing time of these materials when exposed to UV light, typically within 20-30 seconds required for rapid printing, these materials were regarded as potentially useful for rapid encapsulation to avoid QD degradation. For this work, the Anycubic clear basic DLP resin was selected.

For the secondary dispersion and UV resin samples, $20\mu L$ of the prepared QD/toluene solution were added to 40uL of the respective resins and mixed thoroughly. This created

samples with a QD concentration of 56 mg/mL. The solutions were then degassed to remove oxygen and reduce the effects of photo-oxidation on the QDs. To create the samples, 5mm diameter glass coverslips were drop coated with the solutions using a pipette. As surface tension is relied upon to hold the solutions while curing, the samples cured with a convex meniscus.

For the DLP resin samples, a 405nm LED hand torch was used to cure a layer of the solution for 20 seconds. This was done at approximate $10\,cm$ distance, with an irradiance of $13.3\,mW/cm^2$. After the layer was cured, two additional layers were added. The idea behind this was that by creating a sample from multiple layers, the aggregation of the QDs could be minimised, which in turn could minimise a sample's emission redshift.

Polypropylene, despite several attempts, failed to disperse homogeneously into the toluene. The polystyrene and PMMA samples did homogeneously incorporate and were left to cure for 24 hours. As shown in Figure 19, the PMMA sample, although initially promising when in liquid form, aggregated when fully cured and was therefore unsuitable.




*Figure 19: Fabricated test samples of polystyrene, PMMA and UV curing resin.*

Using the successfully cured QD samples and a white-light LED, a hybrid LED was constructed, as seen in Figure 20. The samples were secured into a 10-degree beam angle aluminium-coated reflector using a 2-part Araldite Rapid epoxy glue, taking care to secure the samples flush with the base of the reflector. The reflectors were then secured to a 3D printed mount and positioned in front of the white LED. This construct will be referred to as the “Hybrid LED” in the following sections.

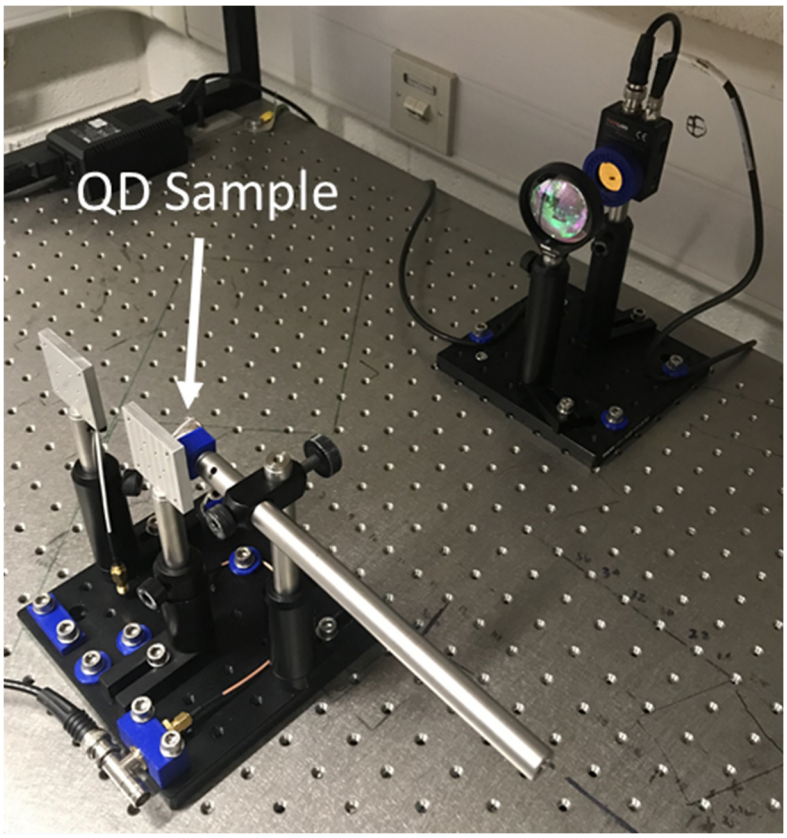



*Figure 20: Experimental set-up for power measurements.*

Figure 20 shows an experiment used to test the optical power of the samples. The LED was driven from an Agilent Arbitrary Waveform Generator (AWG) 81105A, sending a 100Hz sine wave signal. The signal was detected at 0.21m distance using a Thorlabs PDA20C/M Fixed Gain Amplified Detector with an active area of $3.14mm^2$. A Thorlabs LA1401-C 50.8mm diameter plano-convex lens with a focal length of 60mm was used as a collection optic. The gain of the receiver with a 50Ω termination is $1.75 \times 10^5$ $^{V}/_{A}$ and the approximate responsivity of the detector in this region is $1\ A/W$. A Thorlabs FEL1300 1300nm long-pass filter was deployed to reject shorter wavelength components of the light directly coming from the LED.

For the signal measurements, the samples were positioned in front of the white LED and adjusted to achieve the maximum pk-pk voltage. For the DLP resin sample, the measured pk-pk voltage of 2.36V translates to a power of $13.5\mu W$ compared to $8.6\mu W$ (1.51V) for

the polystyrene samples. Despite the relatively small difference in output power, the DLP UV-curing resin sample showed a relatively high photostability. In contrast, the polystyrene samples output power began to reduce significantly within minutes of operation. Taken together with its short curing time (≈20s), which would make such a sample more practical in a commercial environment, the DLP UV resin was deemed a suitable encapsulant for the QDs.

As the DLP resin sample did not appear to photobleach, the emission spectrum was measured and showed the resin affected the QDs emission properties minimally. The resin chosen for the project was the Anycubic photon clear Direct Light Projection resin because of these advantages. The emission spectrum of the DLP resin/QD solution is presented and discussed further in the following section.

## 3.4 CHARACTERISATION OF OPTICAL PROPERTIES

### 3.4.1 Emission spectrum at 1400nm

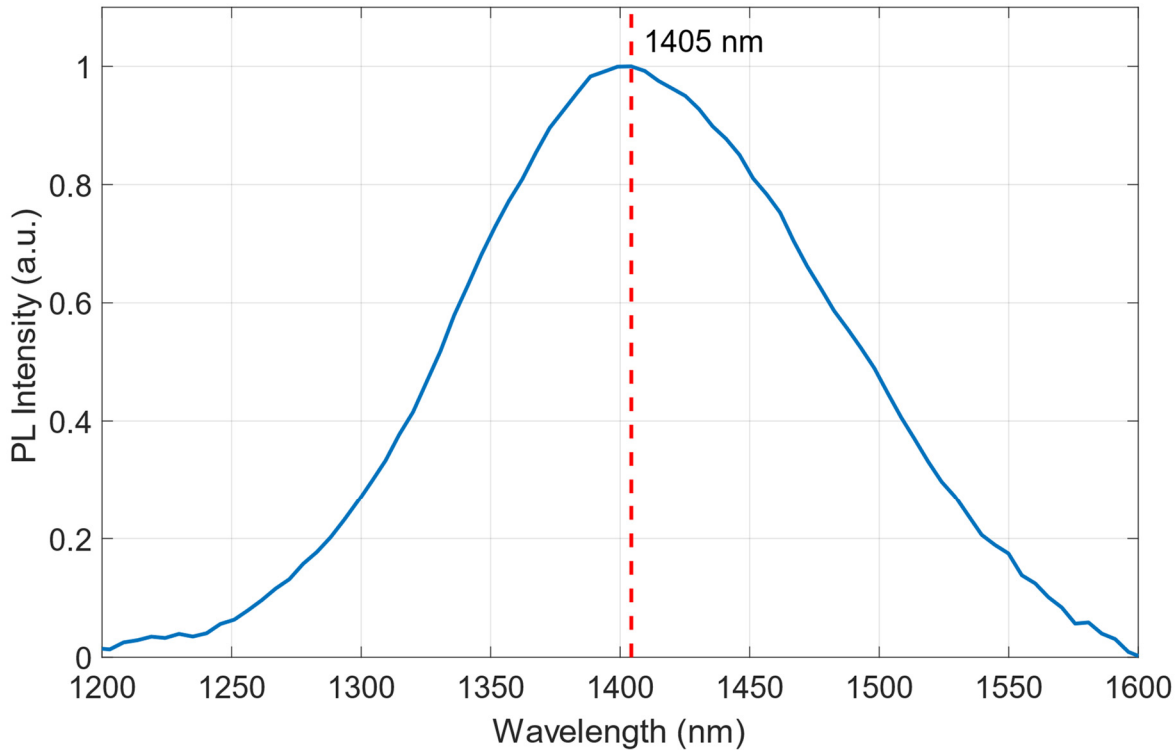



*Figure 21: Emission spectrum of the DLP QD sample when excited with a white light LED (Osram OSLON Compact CM).*

Figure 21 shows the emission spectrum of the DLP QD sample, measured when excited by the white light LED. (A separate measurement of the LED emission was made to verify there was negligible emission from the white LED at 1400nm.) The spectrometer used for this experiment was an Ocean Optics NIR Flame with 2m 600um diameter fibre and 74-VIS collimation lens.

The emission peak is centred around 1405nm and has a FWHM of approximately 175nm. The blue curve in Figure 15 shows the QD emission spectrum before encapsulation when suspended in toluene. There, the emission peak is at 1410nm with a FWHM of 125nm. Even though these measurements were conducted on two different calibrated spectrometers, the DLP resin has preserved the emission spectrum, with a blue shift of 5nm, which is within the resolution of the ocean optics spectrometer. The measurement also shows an

approximate broadening of the FWHM of 50nm between pre and post encapsulation. Overall, using the DLP resin seems to provide a useful encapsulation medium, even for high QD concentrations.

### 3.4.2 Illumination

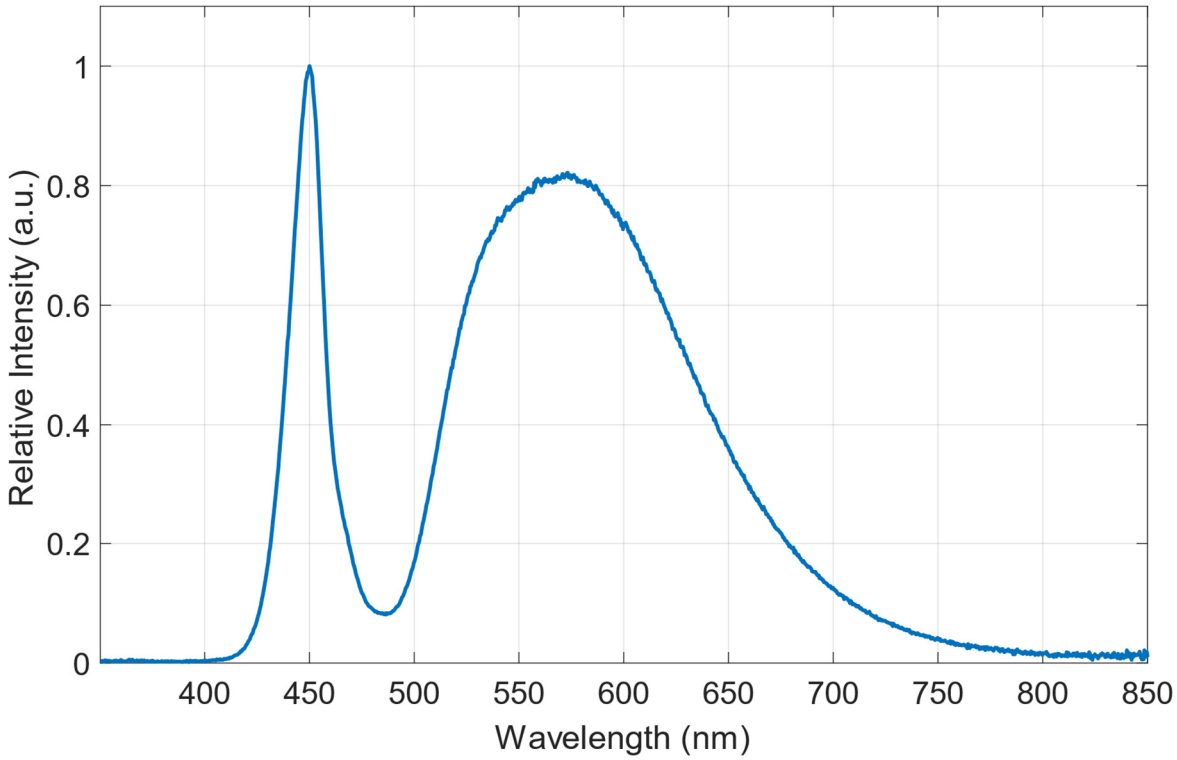



*Figure 22: Emission spectrum of the hybrid LED over the visible region.*

In addition to providing 1400nm and visible light communication links, the Hybrid LED was assessed for its illumination capability. The illuminance of the LED was measured using an Amprobe LM-100 light meter with built-in cosine corrector placed at the end of the reflector, 15mm away from the QD sample. The illuminance of the Hybrid LED on-axis was measured to be 13500 lux which corresponds to a luminous intensity of 3.04 cd.

In addition to luminous intensity, the colour coordinates of the hybrid LED were calculated. These would need to comply with vehicle safety standards to be suitable for automotive applications. The visible emission spectrum, shown in Figure 22, was measured using an Ocean optics OCEAN FX visible spectrometer with QP400-2-SR-BX fibre and

CC-3-UV-S cosine corrector. This system had been calibrated for absolute irradiance. These measurements were taken whilst sending an On-Off Keying signal (OOK) at 4Mb/s. Similar results were obtained for a 1MB/s OOK signal and also when the LED was driven using only a DC supply at 350 mA (a detailed explanation of the communication signal used and the experimental setup can be found in sections 3.5.1 and 3.5.3). The emission spectrum was converted to CIE 1931 standard observer coordinates using Equations 27-34 [88]. Were $\lambda$ is the wavelength (nm) and $L(\lambda)$ is the relative emission intensity of the hybrid LED.

$$X = \int L(\lambda)\bar{x}(\lambda)\Delta\lambda \qquad (27)$$

$$Y = \int L(\lambda)\bar{y}(\lambda)\Delta\lambda \qquad (28)$$

$$Z = \int L(\lambda)\bar{z}(\lambda)\Delta\lambda \qquad (29)$$

$$\overline{x(\lambda)} = 1.065e^{-\frac{1}{2}\left(\left(\frac{\lambda-595.8}{33.33}\right)^2\right)} + 0.366e^{-\frac{1}{2}\left(\left(\frac{\lambda-446.8}{19.44}\right)^2\right)} \qquad (30)$$

$$\overline{y(\lambda)} = 1.014e^{-\frac{1}{2}\left(\left(\frac{\ln\lambda-\ln 556.3}{0.075}\right)^2\right)} \qquad (31)$$

$$\bar{z}(\lambda) = 1.839e^{-\frac{1}{2}\left(\left(\frac{\ln\lambda-\ln 449.8}{0.051}\right)^2\right)} \qquad (32)$$

$$x = \frac{X}{X+Y+Z} \qquad y = \frac{Y}{X+Y+Z} \qquad (33)\ \&\ (34)$$

The CIE 1931 standard observation coordinates were determined for the hybrid LED to be $x = 0.3810, y = 0.3868$ and for the White LED alone the coordinates were $x = 0.3109$, $y = 0.3034$. These are plotted onto the CIE colour space in Figure 23 along with the CIE region permitted for daylight running lights according to the UNECE [67]. As highlighted by the blue and red marker, the colour coordinates of both the white light LED and the hybrid LED lay within the specified boundaries for daylight running lights.

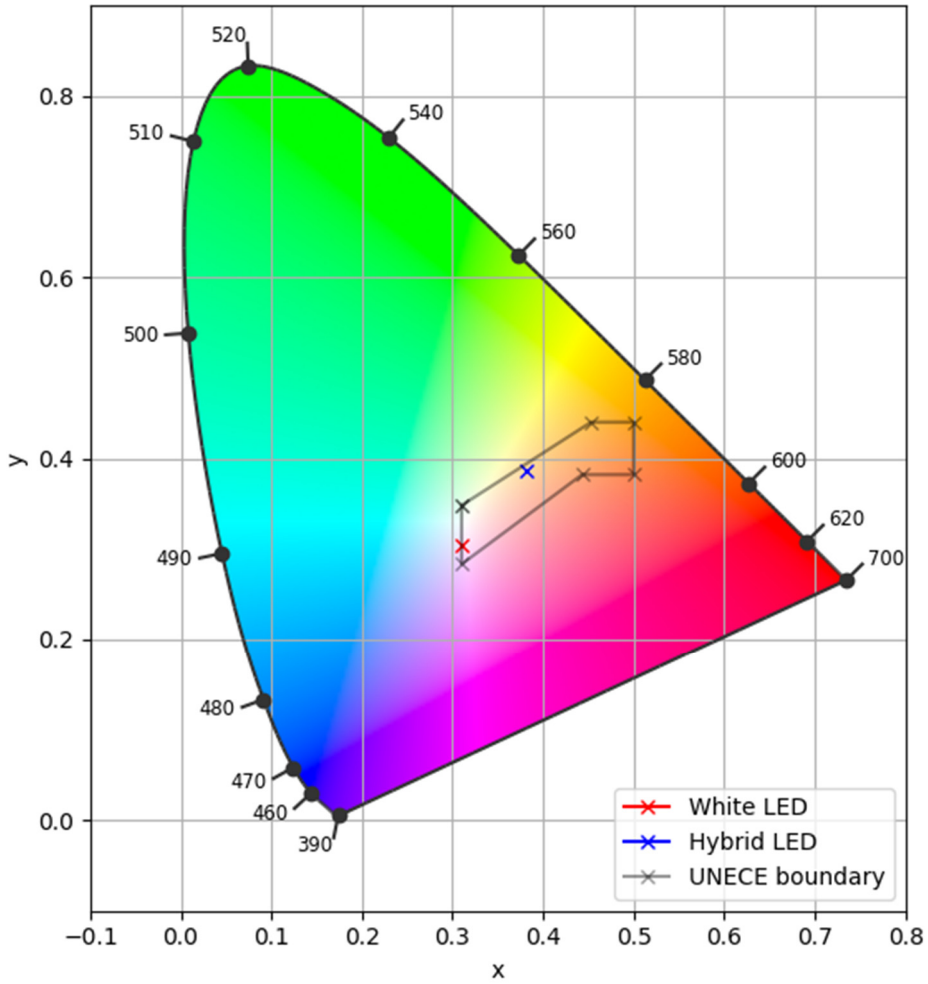



*Figure 23: CIE 1931 standard observer plot with UNECE permitted daylight running light region and marker for white light LED and hybrid LED CIE coordinates.*

### 3.4.3 Stability

The hybrid LED was assessed for photostability of the 1400nm emission from the QD sample. Many fluorescent materials suffer from photo-bleaching and other processes impairing their optical properties, making it essential to ensure the stability of the fluorescent compounds over time.

This test was performed with the experimental setup outlined in section 3.5.1. The changes in maximum voltage of a 100kHz sinusoidal signal measured by an oscilloscope (Keysight MSO7104B) were recorded over a period of 168 hours (one week). The averaging function of the oscilloscope was used with 65536 samples. The 100kHz sinusoidal wave with the

standard amplitude and offset (0.42V pk-pk and 2.81V) was generated with the Keysight 81150A Arbitrary Waveform Generator.

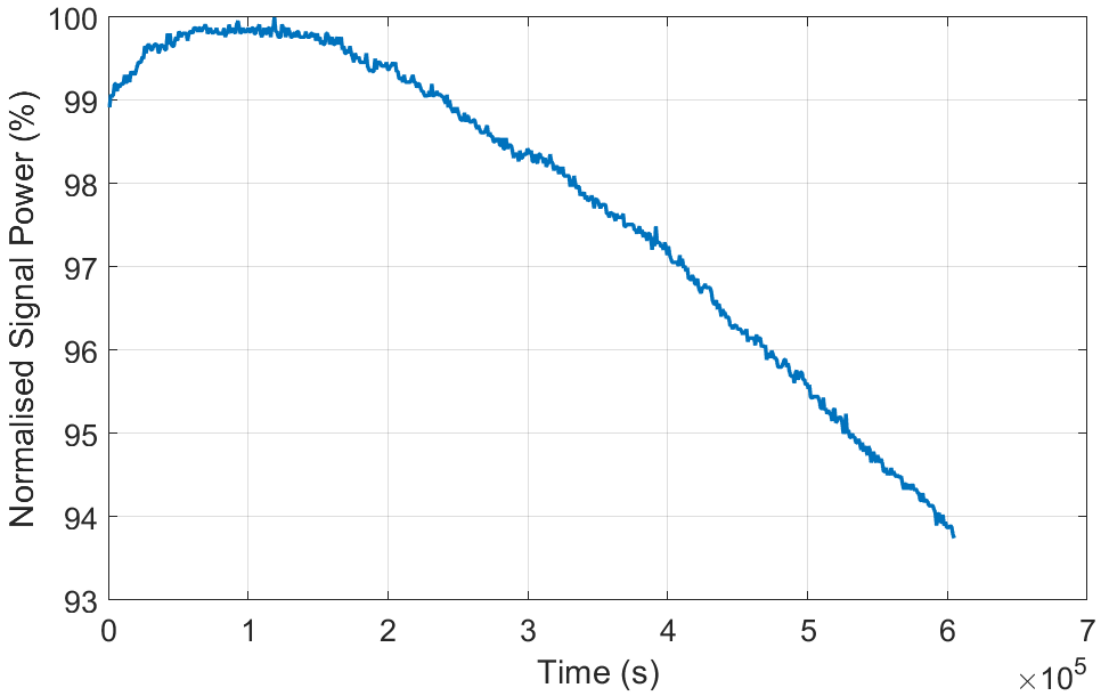



*Figure 24: Normalized Signal Power versus time of the hybrid LED 1400nm emission.*

Figure 24 shows power measurements, taken every 15 minutes, over one week. The data has been normalized to the maximum power. The results show a decrease in the collected power to 6.52% of the initial power output, which corresponds to $17.1nW$. The relatively small loss in output power over the timespan of this experiment shows that the DLP encapsulate resin used with the QDs provides reasonable long-term stability.

## 3.5 Characterisation of Communication Properties

### 3.5.1 Experimental set-up

To test the performance of the hybrid LED, an experiment was constructed as shown in Figure 25. The LED was driven by a Keysight 81150A Arbitrary Waveform Generator, delivering a maximum driver current of 440mA [83]. For the 1400nm link, the receiver used in the experiment was a Thorlabs PDA20C/M InGaAs fixed gain amplified receiver with a

3.14mm$^2$ detector area, Noise Equivalent Power (NEP) of $22\,pW/\sqrt{Hz}$ and 5MHz bandwidth [85]. An Edmund Optics 1400nm Centre Wavelength (CWL), 12nm FWHM, Optical Density (OD) $\geq 4$, 25mm interference filter was used at the receiver with a Thorlabs LA1401-C 50.8mm diameter plano-convex lens with a focal length of 60mm as a collection lens. This lens was chosen to maximise collection area whilst keeping the angle of incidence of light approaching the filter under 25 degrees. This ensured that the interference filter passband shift is within the 'quiet' region of the optical spectrum (which extends from 1410nm to a lower wavelength of 1350nm).

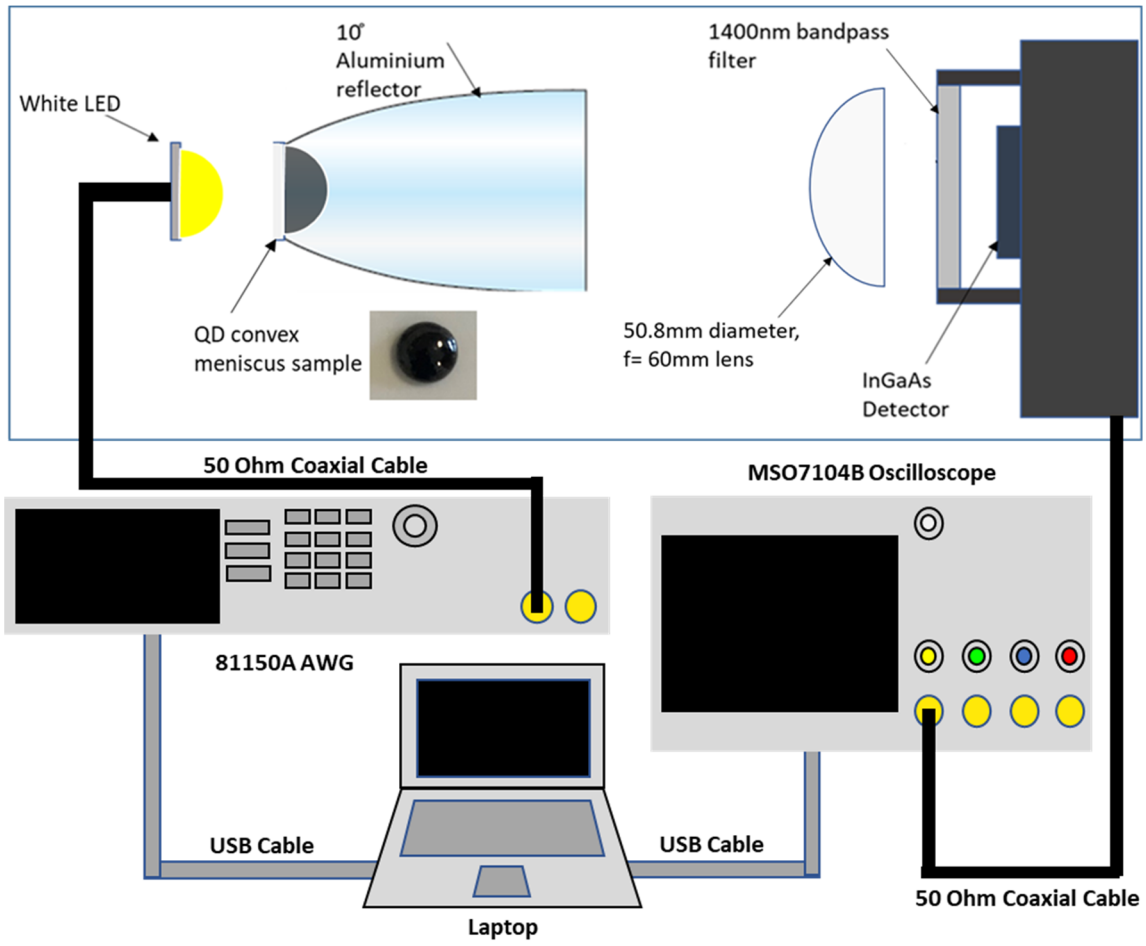



*Figure 25: Diagram of Hybrid LED Experimental Set-up.*

For characterization of the 450nm channel, an identical configuration was used but with the replacement of the PDA20C/M receiver with a Hamamatsu SI C12702-04 APD receiver

which has an active area of $7mm^2$, NEP of $3\ pW/\sqrt{Hz}$ at 450nm and a -3dB bandwidth of 80MHz [86]. In addition, the 1400nm filter was replaced with the Thorlabs FBH450-10 450nm filter with a 10nm FWHM. The receivers were connected to a Keysight MSO7104B oscilloscope which captured the received waveform.

In the following results, the electrical waveform that modulated the proposed LED had an amplitude and offset of 0.42V pk-pk and 2.81V. These values were measured across the white LED with a 1MΩ scope probe and were optimized to provide minimum signal distortion due to the limited dynamic range of the LED. The maximum voltage of the applied signal (3.02V) corresponds to the AWG's maximum supply current of 440mA. These values were used to obtain the following results unless otherwise specified.

### 3.5.2 Bandwidth Measurements

To conduct the bandwidth measurements, code was written to control the instruments using Keysight benchVue software. This swept the AWG through a series of sinusoidal waveforms of increasing frequency whilst adjusting the time base of the oscilloscope and recording the pk-pk voltage of the received signal. The sample average of the oscilloscope was set to 1024 to minimise noise, and the experiment was performed over a link distance of 0.25m.

***QD Frequency Response***

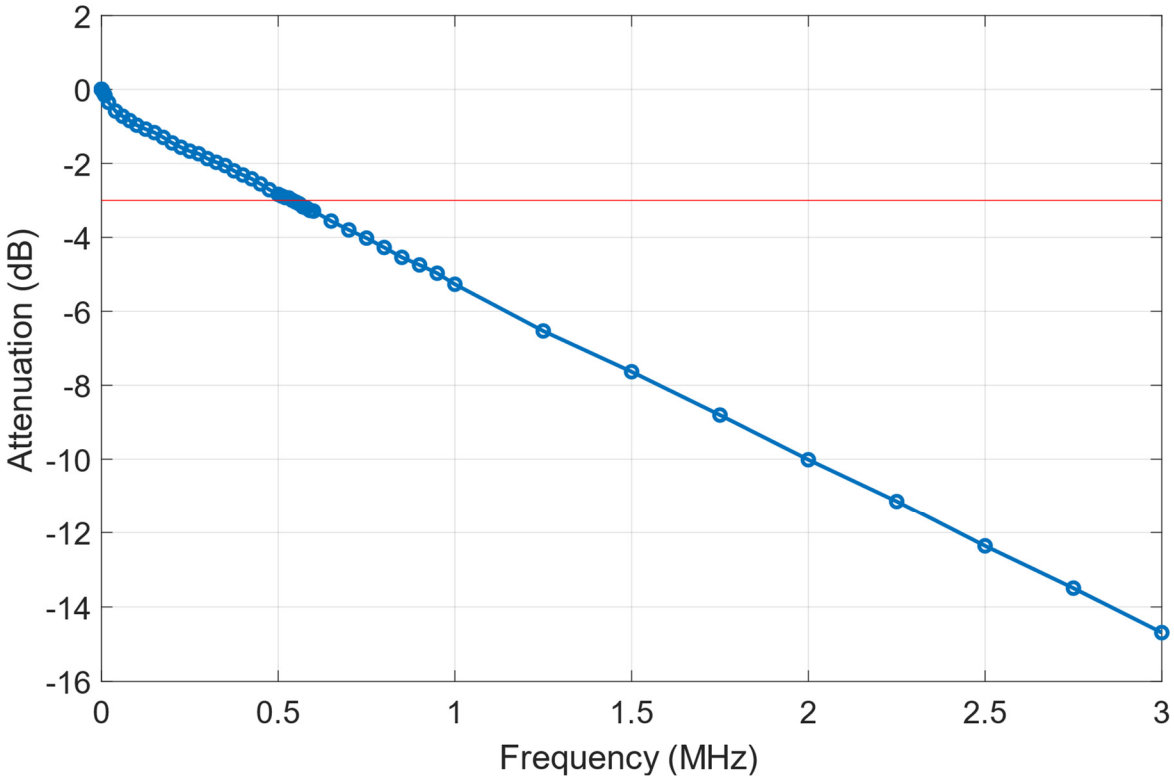



*Figure 26: Frequency response (electrical-electrical) of 1400nm component of light emitted from HybridLED.*

Figure 26 shows the frequency response of the QDs with an -3dB electrical-to-electrical bandwidth of 545 kHz for the 1400 nm channel.

***450nm LED Frequency Response***

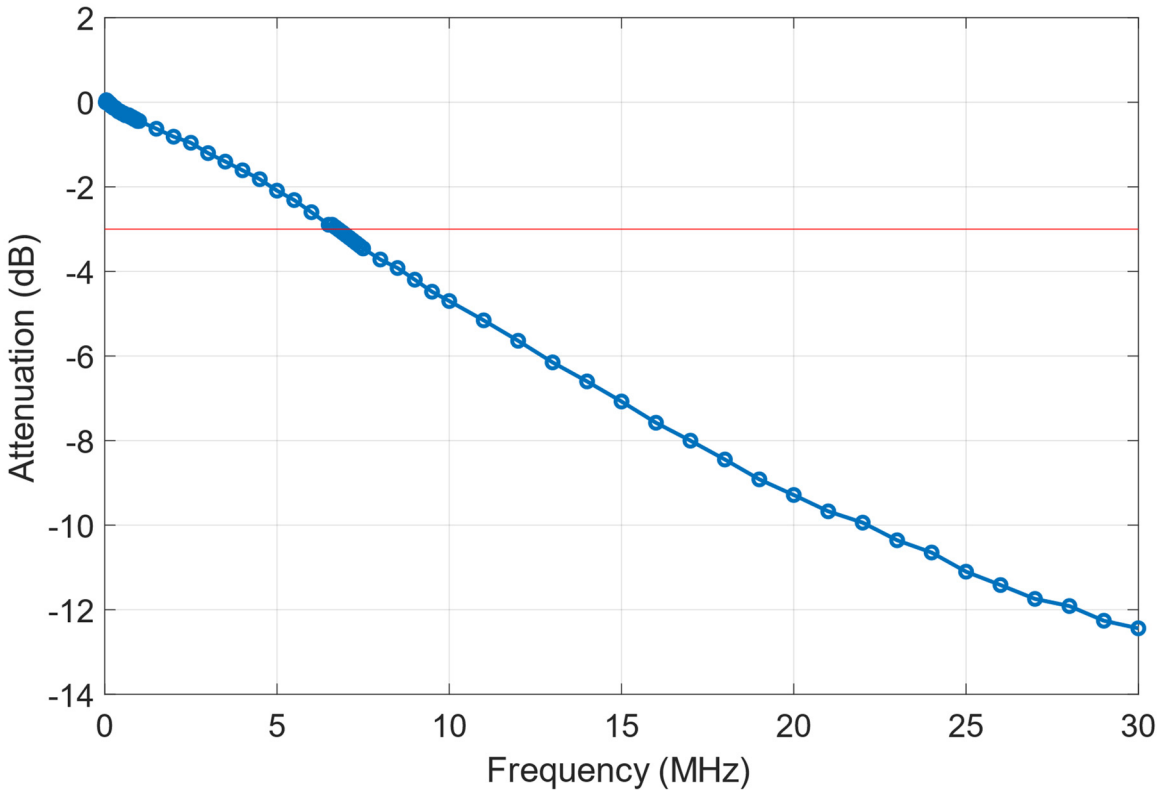



*Figure 27: Frequency response (electrical-electrical) of the 450nm component of light emitted from the hybrid LED.*

Figure 27 shows the frequency response of the 450nm component of the hybrid LED. The -3dB electrical-to-electrical bandwidth for the 450 nm channel was measured to be 7.6 MHz.

### 3.5.3 On-Off keying communication in dark conditions

Data packets containing a $2^{10}$ pseudo-random On-Off Keying (OOK) bit sequence were generated using a custom MATLAB script and transmitted across the link. The received data was filtered using a digital $6^{th}$ order Butterworth low pass filter with a -3dB bandwidth 1.4 times larger than the data rate of the signal. Decision Feedback Equalization (DFE) [89] was used on the 1400nm link to compensate for the low bandwidth of the QD conversion material. This was used with a forget factor of 0.98, and the forward tap and feedback taps were set to 4 and 2 respectively with samples per bit set to 2 (these values give the highest data rates at the forward error correction limit). The Bit Error Rate (BER) was estimated by

comparing transmitted and received data to detect errors in the bit sequence. Unless otherwise specified, the results presented in this work are the averaged BER for 100 data packets.

The BER was measured at different data rates for the link distances of 0.25, 0.50, and 0.75 m. Figure 6 shows the BER vs data rate for the 1400nm link with and without DFE. The maximum data rate achieved with a BER lower than the forward error correction limit (FEC) of $2.8 \times 10^{-3}$ was 1.75 Mb/s over 0.75 m for the 1400 nm channel without DFE. Using DFE, this could be increased to 2.0 Mb/s. A maximum data rate of 4.1 Mb/s was measured for the shortest distance, which could be increased to 5.6 Mb/s using DFE. Figure 7 shows a similar set of curves for the 450nm communication channel without DFE.

In this case, the maximum data rate was 41 Mb/s at a link distance of 0.75 m and 42.5 Mb/s at 0.25m. Over the measured 1400nm link distances the detected power varied from 0.17-0.29 µW and for the 450nm link distances the detected power varied from 4.73-5.70 µW.

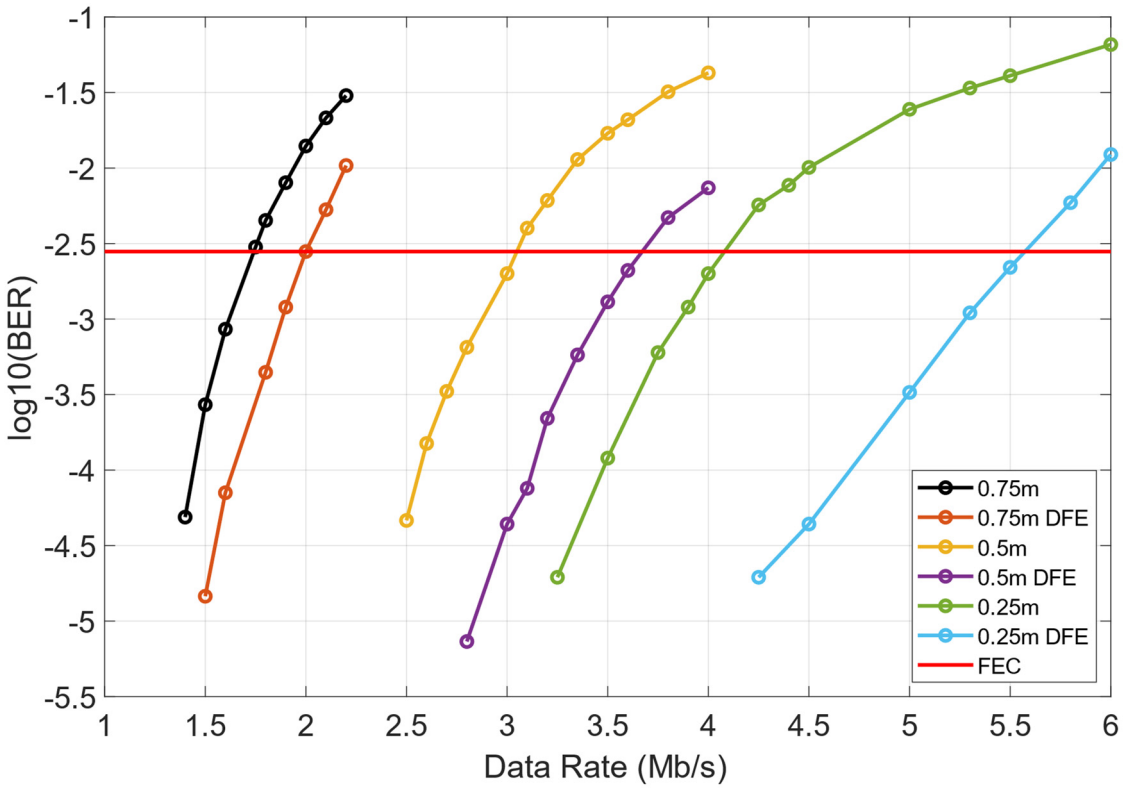


*Figure 28: BER versus data rate (Mb/s) of the 1400nm channel for 0.25m, 0.5, 0.75m links with and without DFE. Forward Error Correction (FEC)*

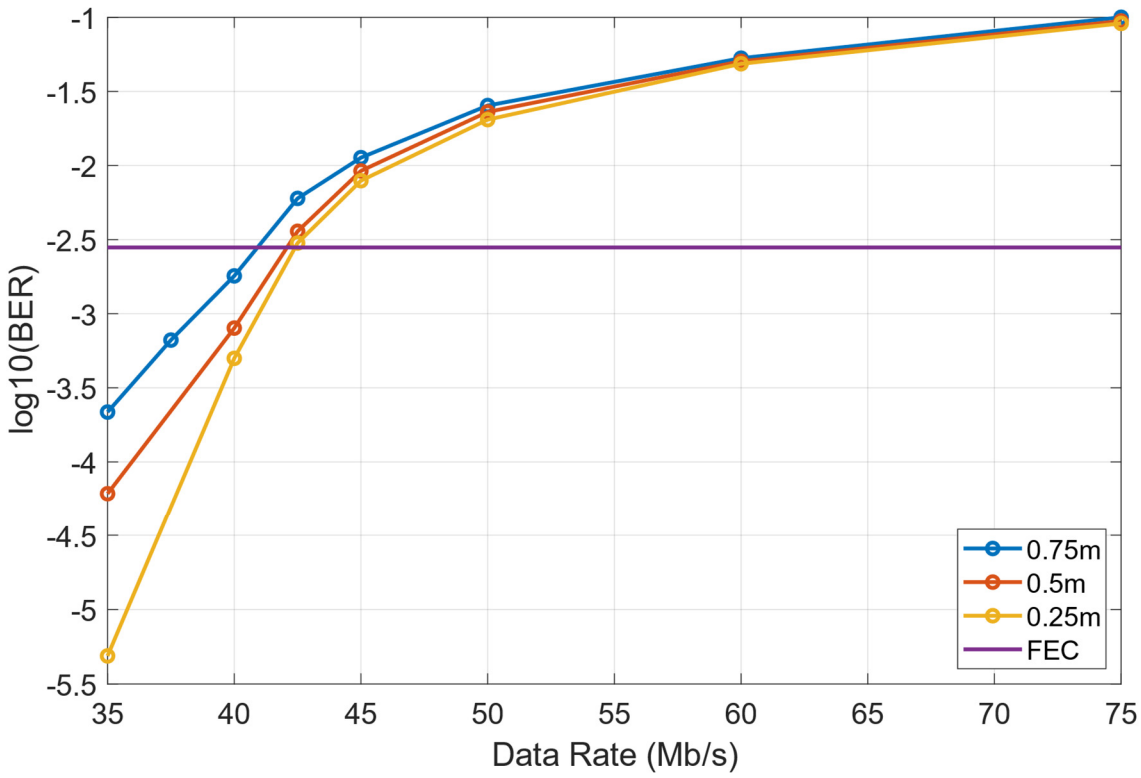



*Figure 29: BER versus data rate (Mb/s) of the 450nm channel for 0.25m, 0.5m, 0.75m links without DFE. Forward Error Correction (FEC)*

### 3.5.4 Sunlight effect on 1400nm and 450nm links

Based on the model presented in Chapter 2, the proposed communication link at 1400nm should be minimally affected by ambient sunlight and therefore provide an advantage over communication at 450nm. To assess the impact of ambient sunlight, the 1400nm and 450nm communication links were set up within a windowed lab over a 0.25m link distance. The experiments were conducted at a single data rate of 4Mb/s and 42.5Mb/s for the 1400nm and 450nm links respectively, with a BER below the FEC limit at 0.25m in dark conditions for both links. The BER for each of the links was collected 100 times with $2^{10}$ bit sequences in both darkroom and daylight conditions. During the experiment, the average sunlight illuminance was recorded periodically using a lux meter placed as closely as possible to the receiver without blocking the optical link.

To avoid incident sunlight below 1350nm being permitted through the 1400nm bandpass interference filter, the measurements were conducted only when the angle of incidence of the sunlight upon the filters was under 25°. Sunlight was permitted to directly illuminate the filter/receiver, bypassing the receiver collection lens. The FOV of the lens was too small to align sunlight directly into the receiver to conduct the experiment.

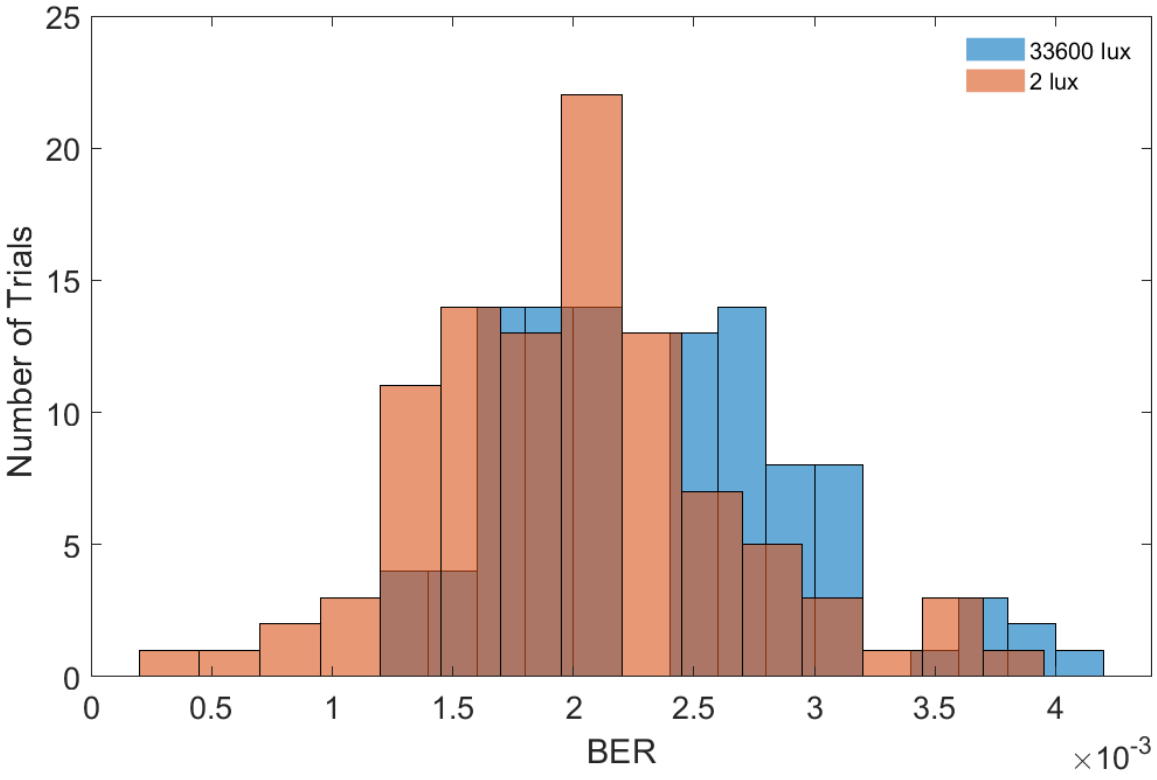



*Figure 30: BER histogram for darkroom (2 lux) and sunlight conditions (33600 lux) for the 1400nm link.*

Figure 30 shows a histogram of the BER of the 1400nm link with and without the presence of sunlight. The mean BER measured in a dark room (2lux) was $2 \times 10^{-3}$ with a standard deviation of $6.41 \times 10^{-4}$. At 33600 lux, the BER measured $2.4 \times 10^{-3}$ with a standard deviation of $7.25 \times 10^{-4}$. Since the mean BERs lie within the standard deviation of one another, these changes can be regarded as negligible.

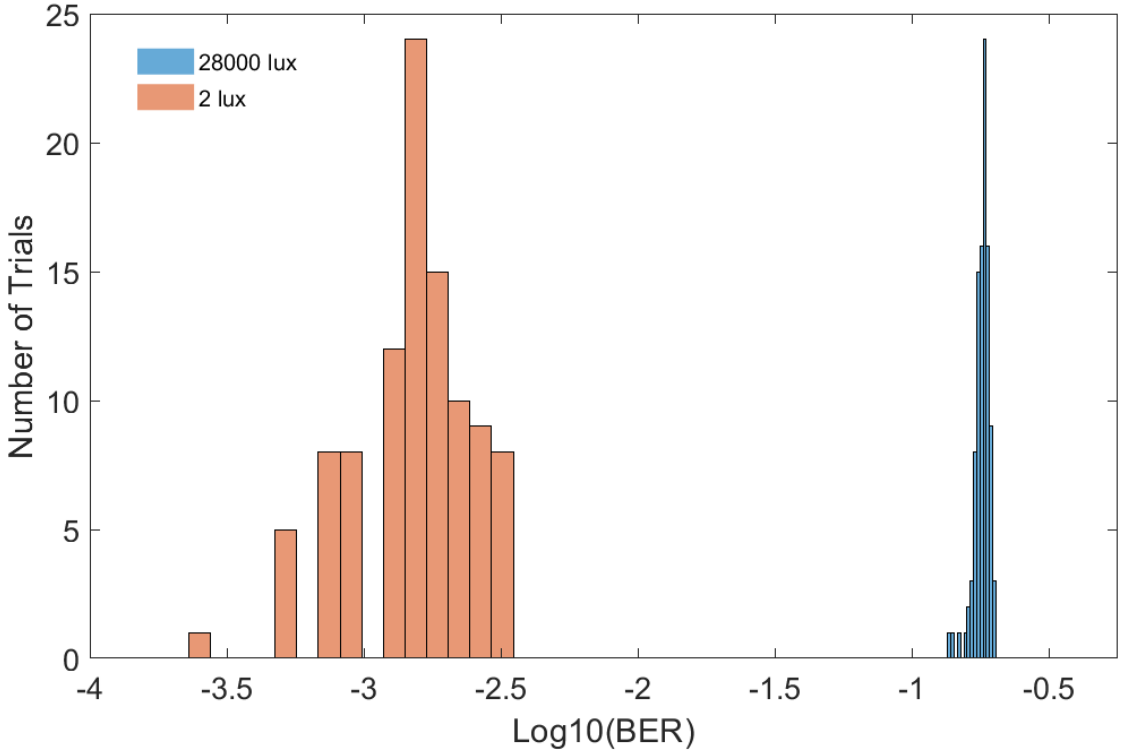



*Figure 31: BER histogram for darkroom (2 lux) and sunlight conditions (28000 lux) for the 450nm link.*

Figure 31 shows a histogram of the BER for the 450nm link with and without the presence of sunlight. The mean BER measured in a dark room (2lux) was $1.6 \times 10^{-3}$ with a standard deviation of $7.27 \times 10^{-4}$. At 28000 lux, the BER was measured at 0.18 with a standard deviation of $11.3 \times 10^{-3}$. It can be seen there is a substantial degradation in link performance for the visible link, but the 1400nm link performance is similar in sunlight as it is under darkroom conditions.

### 3.5.5 Characterising the ambient sunlight benefit at 1400nm

***Sunlight Power measurements***

To support that the observed robustness of the 1400nm link is due to an ambient light benefit, an experiment was set-up to measure the power ratio between the 450nm and 1400nm optical bands (Figure 32). Two Newport power meters, 843-R with an 11.3mm diameter SI visible detector head (818-SI) with a Thorlabs FB450-40 450nm CWL 40nm FWHM filter and a 1919-R with a 3mm diameter Germanium (Ge) Near-Infrared detector head (818-IR) with

an Edmund Optics 1400nm CWL, 12nm FWHM filter, were used for this experiment. Press-fit filter holders were made to house the 450nm and 1400nm filters over the respective detectors ensuring that the filters made a tight fit with the casings of the detector heads. A bracket was created to mount an Amprobe LM-100 hand-held lux meter alongside the two detectors to provide an illuminance measure. Power values from all detectors were obtained simultaneously using a camera to calculate the ratio between 450nm and 1400nm channels.




*Figure 32: Picture of the experimental set-up for 450nm and 1400nm power measurements, angled to match the incident angle of the sun.*

This experiment was conducted during mid-morning, where the temperature was between $4 - 9°C$ and the sky was clear. Critically, these are good conditions to test the minimum (worst case) ratio between 450nm and 1400nm irradiance, as in these conditions, there is a minimal amount of water in the optical path to absorb light in the 1400nm region. Throughout the experiment, the power levels were tested by adjusting the angle of the

experiment to match the sunlight incident angle as closely as possible. This ensured the shift in the passbands of the optical filters, which occurs as the collimated light is incident off-axis, was kept to a minimum.

The optical transmission spectra of the 450nm and 1400nm filters were measured to correct for different filter passbands, as shown in Figure 33. This was done using a Perkins-Elmer Lambda 750S spectrometer, and the interval step between measurements was set to 5nm as default. The transmission curve was then used to correct the obtained power measurements. For the visible silicon detector, the sensitive region is $350 - 1100nm$, and for the Germanium detector, this region is $780 - 1800nm$ [87], so only these regions were considered in the calculations.

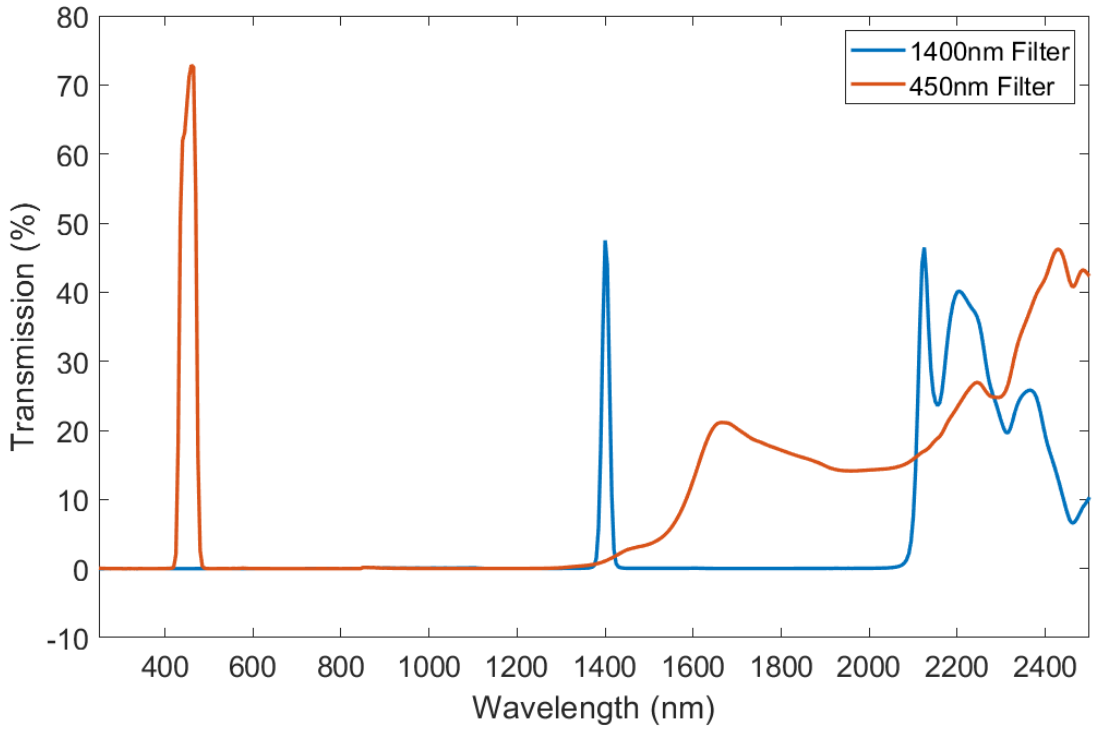



*Figure 33: Transmission (relative to calibrated source) of collimated radiation through 1400nm and 450nm filters.*

At an illuminance of 87300 lux, the power at 450nm and 1400nm was measured to be $2.3mW$ and $6.07\mu W$ respectively. Considering the areas of the two detectors (11.3mm diameter for the visible range and 3mm diameter for the IR detector) and filter transmission

(Figure 33), the ratio of the ambient sunlight power received in the 450nm and 1400nm bands is 9.6. This suggests a significant benefit in ambient light noise for the 1400nm over the 450nm channel.

Similar indoor measurements were made within the same lab that the Hybrid LED experiments were conducted. At 15240 lux, the power measurements for blue and 1400nm links were $103.5\mu W$ and $214.1nW$, respectively. The ratio of the 450nm to 1400nm power, again considering the filter transmission profiles and respective areas, for the indoor measurement came to 12.3. Compared to the outdoor measurements, the higher value of the ratio indicates a greater attenuation of light at 1400nm through the lab windows. This could have influenced the comparative performance of the two channels slightly favouring the 1400nm link. To experimentally verify the robustness of a 1400nm link in the outdoor environment, a high-power 1400nm source will be introduced and tested in Chapter 4.

***Theoretical Estimation of Ambient Light Noise***

For a theoretical estimate of the ambient light noise benefit, the power in the relevant optical bands was calculated by multiplying the Airmass 1.5 spectrum with the filter transmission and then scaling the product based on the illuminance.

When considering an illuminance level of 83400 lux and the respective detector areas of the two power meters, the model generates powers of $3.0mW$ for the blue channel and $1.08\mu W$ for 1400nm channel. When considering equivalent detector areas, the blue channel sunlight power is 196.5 times greater than that of the 1400nm channel. This is approximately a factor of 7.4 times larger than experimentally observed in the previous section, and can be attributed to a higher than expected power at 1400nm.

It is important to note that the ambient temperature on the day of the experiment was low (4-9°C), which means the water content of the atmosphere was small. Therefore, the

attenuation of light at 1400nm might have been less significant than the model assumes based on the airmass 1.5 spectrum (15°C [49]), and consequently, the observed 1400nm band power reading was greater.

***Noise considerations for 450nm and 1400nm links***

In the communications testing in section 3.5.4, the 1400nm link showed a robust performance in high ambient light conditions. In the 450nm link, in contrast, the BER increased significantly once ambient light was introduced. This section examines the cause of this in greater detail. The SNR of the photodiode links is given in Equation 35, with the individual parameters listed in Table 9 for both links.

$$SNR = 10\log_{10}\left(\frac{i_{sig}^2}{(i_{shot}^2 + 2ei_{amb} + i_a^2)B}\right) \quad (35)$$

*Table 9: Signal current and noise contributions for 450nm and 1400nm links.*

| Parameters | 450nm | 1400nm |
|---|---|---|
| Signal current $i_{sig}$ ($\mu A$) | 10.4 | 0.3 |
| Signal shot noise $i_{shot}^2$ ($A^2$/Hz) | $3.6 \times 10^{-24}$ | $9.6 \times 10^{-26}$ |
| Ambient light shot noise $2ei_{amb}$ ($A^2$/Hz) | $3.9 \times 10^{-22}$ | $2.2 \times 10^{-23}$ |
| Amplifier noise $i_a^2$ ($A^2$/Hz) | $3.6 \times 10^{-23}$ | $5.3 \times 10^{-22}$ |

In the 450nm link, the ambient light noise term dominates, being at least an order of magnitude larger than all other noise components. As a result, the BER distribution significantly changed upon introducing ambient light to the 450nm link, as shown in Figure 31.

In contrast, the 1400nm link has an ambient light noise term, which is a factor of 20 smaller than the amplifier shot noise of the receiver, showing the link is limited by the amplifier current noise. Consequently, its performance was not affected significantly by ambient light (Figure 30).

Efforts to improve the performance of the 1400nm link for the existing signal power level should focus on the receiver noise performance. The ambient sunlight equivalent current noise is 4.7 $pA/\sqrt{Hz}$, indicating substantial reductions in the receiver noise is possible before ambient sunlight noise becomes significant.

## 3.6 DISCUSSION

### 3.6.1 Communication at 450 nm and 1400 nm

The -3dB bandwidth of the QDs was found to be 545kHz. This is roughly one order of magnitude smaller than the blue channel bandwidth of 7.6MHz. Taken together with the significantly lower output power in the 1400nm channel, the achievable data rate under the FEC limit was considerably lower than in the blue channel (1.75 Mb/s for 1400nm compared to 42 Mb/s for 450nm over a link distance of 0.75m). Both these results indicate that for high-speed communication, the blue channel would be more suitable. Such communication could include map sharing, video calls, and other services where a larger amount of data needs to be transferred.

A sunlight-robust 1400nm link could be used within the automotive environment for safety-critical, low data rate signals such as stop and turn signals. The vehicle safety communications consortium, consisting of BMW, Ford, VW and others, estimates that a minimum data rate of 9 kb/s would be necessary for the transmission of safety-critical data between vehicles, a rate achievable by a QD based link [79].

As a critical challenge, the range of the 1400nm channel link distance needs to be increased towards 100 meters, which requires a much greater signal power. At the transmitter, the QD concentration and sample thickness could be optimised to maximise the output signal of the 1400nm link. Higher sample concentration and thicknesses would increase the probability of a photon emitted by the LED being absorbed by a QD and re-emitted at 1400nm. This

could increase the output signal intensity and possibly the maximum achievable range of the link. However, at very high concentrations, secondary absorption processes will impair the emission power and therefore, the communication performance. In an ideal scenario, the QD concentration and layer thickness would be optimised to provide a maximum output at 1400nm. Additionally, the advent of new NIR fluorescent materials could improve the performance of a 1400nm link.

Future optimisation attempts should consider that the impairment of the blue channel and the illumination qualities of the hybrid LED should be kept to a minimum. In addition, the receiver used for the 1400nm link experiment was not optimised, and further gains in range would be achieved using a low bandwidth receiver for the 1400nm link, tailored for the minimum data rates required for safety applications. As standard in daylight running lights, the use of multiple hybrid LEDs could improve the link power. This option is discussed in detail for illumination purposes in section 3.6.3

### 3.6.2 Robustness to sunlight

As outlined in section 3.5.5, the SNR of the 450nm channel is dominated by the ambient light noise. This is reflected in an increase of the BER of two orders of magnitude upon introducing sunlight to the link. In contrast, the SNR of the 1400nm channel is receiver amplifier noise limited, making it robust to ambient sunlight, which was shown experimentally in this chapter. Consequently, the 1400nm channel would highly benefit from a lower noise receiver. As indicated by the calculated noise contributions, by reducing the receiver amplifier current noise, significant improvements to the SNR could be made without compromising the link robustness to ambient sunlight.

### 3.6.3 Illumination

As the hybrid LED is intended to be used as part of the lighting infrastructure in an automotive environment, one of its essential tasks is to provide illumination for visibility and safety.

The UNECE requires a minimum luminous intensity for a daylight running light of 400cd on axis [67]. For the hybrid LED, the luminous intensity was measured to be 3.04cd. Thus, to meet the standard, a large number of the current LEDs would be required. By increasing the number of LEDs required to meet the luminous intensity standard, the available power in the 1400nm link would in practice be substantially higher and could allow for communication over larger distances and at higher data rates. Optimisation of the QD layer could additionally improve the illumination parameters. Future work into this field could focus on optimising parameters such a plate thickness and QD concentration.

In addition, from the visible emission spectrum of the hybrid LED as shown in Figure 23, the CIE colour coordinates have been translated from the white LED from $x = 0.3810, y = 0.3868$ to $x = 0.3109, y = 0.3034$. This occurs as the Pbs QDs have much greater blue light absorption than components of the white light of a larger wavelength. This means that the proportion of blue light is decreased, producing a source with a warmer colour temperature. Despite the warmer colour temperature of the hybrid LED, the values of the CIE coordinates are within the permitted limits set by the UNECE legislation for daylight running lamps, therefore making the colour composition practical for the automotive environment [67].

### 3.6.4 Functional Encapsulation using DLP resin

Finding a suitable encapsulation material for the QDs proved to be a crucial challenge for the success of this body of work. The employed DLP UV curing resin allowed for the

fabrication of solid samples containing the QDs while preserving their optical properties. As such, the emission peak was observed at 1405nm, which suggests that minimal aggregation or degradation occurred.

The stability measurements performed in this work observed a reduction in signal power by approx. 6.5% over one week (~168h). Encapsulation of the QDs within the DLP UV resin is a good starting point for further research experiments. To be practically used in an automotive environment, the lifetime of the QDs would have to be characterised over timespans several orders of magnitude larger than performed in this work, to match the lifetime of typical lighting infrastructure. Improvements could focus on the encapsulation process, as well as introducing protective agents to the sample.

### 3.6.5 Vehicular deployment

Due to the lead content of the PbS QDs employed in this work, the hazards presented to human health, wildlife, and the environment have to be considered carefully prior to the application in the automotive environment. With the development of more suitable visible to NIR fluorescent materials and the refinement of fabrication techniques, the technology could be brought into the commercial market. Such fluorescent materials could be directly incorporated with the phosphors used for white LED coatings or visible QDs, placed directly onto the base LED.

## 3.7 CONCLUSION

This chapter has presented the fabrication and testing of a novel Hybrid LED source for optical communication providing both visible and 1400nm channels as well as illumination. The preliminary investigation has shown a maximum data rate of 2Mb/s can be achieved over 0.75m for a 1400nm link. Furthermore, the source facilitates a 450nm channel at

41Mb/s over the same link distance. Importantly, the 1400nm link could be maintained in ambient light conditions without being significantly impaired.

The Hybrid LED visible colour coordinates lay within the colour guidelines for automotive applications. This suggests that if providing sufficient intensity, a composite of multiple hybrid LEDs could be used for illumination in vehicles.

Regarding the Hybrid LED fabrication, the DLP UV-curing resin provided a practical way of encapsulating the QDs into solid layers and ensured the preservation of their optical qualities. As such, the emission peak of the QDs remained unchanged and maintained a good photostability over 168h of continuous operation.

With these hybrid LEDs, the proposed communication approach would be implemented in a low complexity system providing two communication channels and illumination suitable for the automotive environment.

# 4. CHAPTER: 1400NM TRANSMITTER

## 4.1 OVERVIEW

This chapter focuses on the employment of commercially available components to create a 1400nm transmitter. As explained in Chapter 3, a significant drawback of the hybrid LED is the low power output in the 1400nm channel, limiting the achievable range and data rate of a 1400nm link. The use of InGaAsP NIR LEDs allows for the increase in output power and therefore, an increase in the achievable link distance and data rates. To build the transmitter, four InGaAsP LEDs were used as 1400nm sources on a custom-designed Printed Circuit Board (PCB), encased within a 3D-printed housing. In this chapter, the circuit design and PCB layout are discussed. Experiments assessing the communication performance of the transmitter and the link robustness in ambient light are then described.

## 4.2 TRANSMITTER DESIGN

### 4.2.1 Choice of Source

The source for a 1400nm link would ideally have the following features:

- A **high output power** to allow for large link budget communication over long distances.
- A **large modulation bandwidth** to allow for high data rates in the link.
- Given the angular dependency of bandpass filters, a **sufficiently large optical emission bandwidth** to provide practical FOVs for an automotive link

To fulfil these requirements, two options for the 1400nm source were considered and are briefly discussed below.

***Laser diode***

The use of a laser diode as a 1400nm transmitter could offer the benefits of high output power and can possess a modulation bandwidth into the GHz range [90]. Their major disadvantage is caused by a narrow optical bandwidth (<10nm), which is known to be subject to thermal drift (0.1 – 0.5 nm/°C) [91]. In conjunction with the angular dependence of the passband of interference filters (see section 2.2.5 in chapter 2), a 1400nm link based on a laser diode transmitter would be confined to a narrow FOV and carefully controlled conditions. Laser diodes, therefore, were deemed to be impractical and were ruled out from this investigation.

***InGaAsP LED***

LEDs have been commonly employed in VLC links, and offer a reasonable modulation bandwidth. In this work, components were chosen and the transmitter designed to allow data transmission with a channel bandwidth of 5MHz. This was set by the InGaAs receiver (Thorlabs PDA20C/M, 3.14mm$^2$ active area), which would be used within the experiments [85].

High power LEDs emitting at 1400nm are not commercially available. An InGaAsP LED (LED1450L, Thorlabs) emitting at 1450nm with an output power of 5mW at 50mA [92] was used. Due to its broad optical bandwidth, the LED also emits in the 1400nm region of interest. Furthermore, a proportion of the signal will be transmitted through the bandpass filters, even at large angles of incidence.

### 4.2.2 Circuit Design

To get the maximum power from the LEDs whilst reducing the risk of damage, it was decided to use a current-driven circuit as this provides greater control over the LEDs than its voltage-driven equivalent.

Different circuit topologies for the transmitter were considered. Driving each LED individually by separate circuitry offers good performance but with high complexity. In addition, connecting the LEDs in parallel was also considered, but current consumption is high, and there is potential for thermal runaway of individual LEDs. Instead, a design with the LEDs in series was selected.

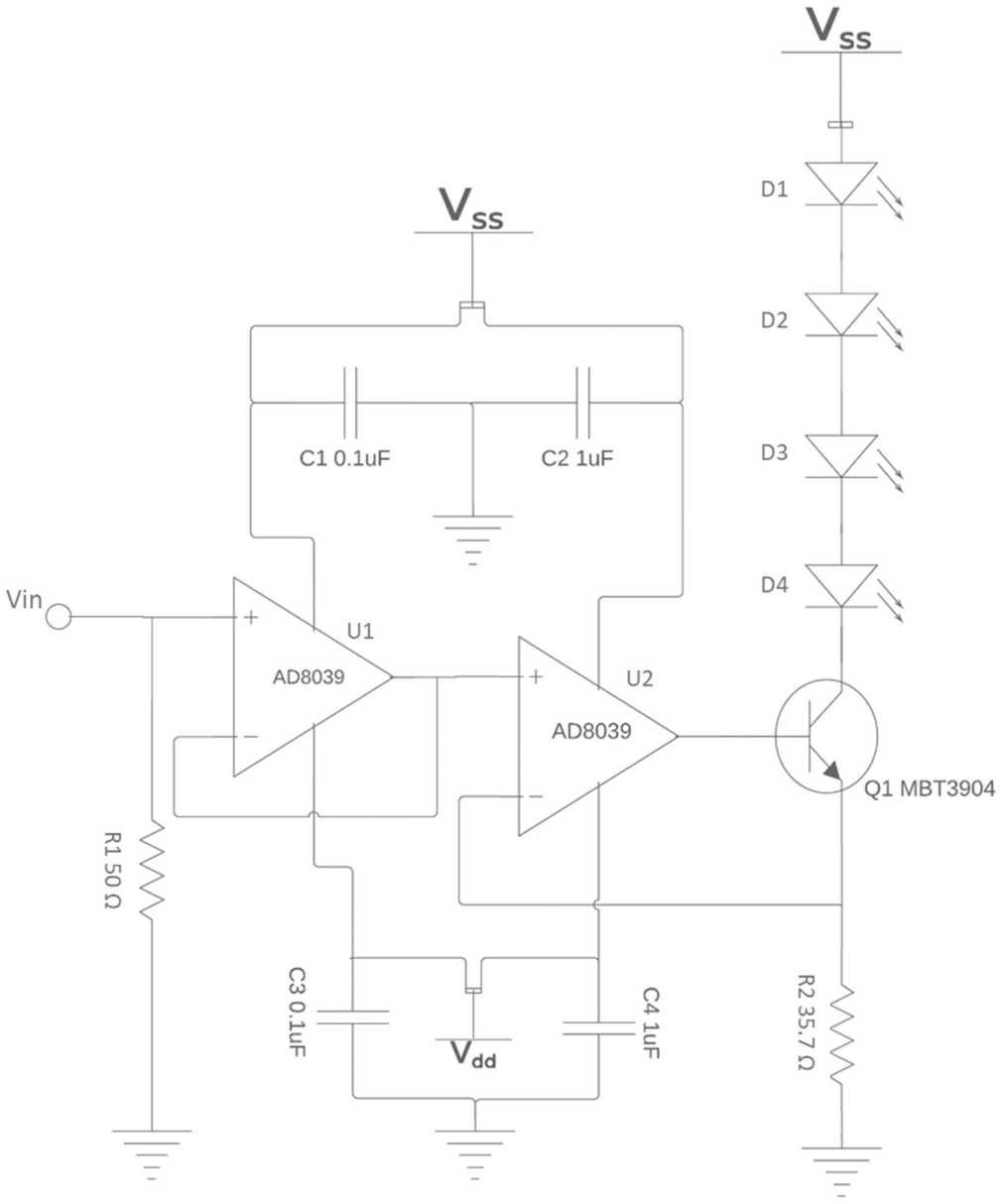



*Figure 34: Circuit Diagram of 1400nm Transmitter.*

Figure 34 shows the circuit, based on the current source design in [93]. The operation uses a bipolar junction transistor (Q1) as a current gate whilst using an AD8093A Operational amplifier (U2) to provide negative feedback to the base of Q1 by measuring the voltage drop across a 35.7-ohm resistor (R2). The circuit was constructed to not exceed a current of 100mA through the LEDs, which is their continuous current limit [92]. The operational amplifier U1 is wired in a buffer configuration with the resistor R1 placed between the input and ground providing a 50 Ω input impedance.

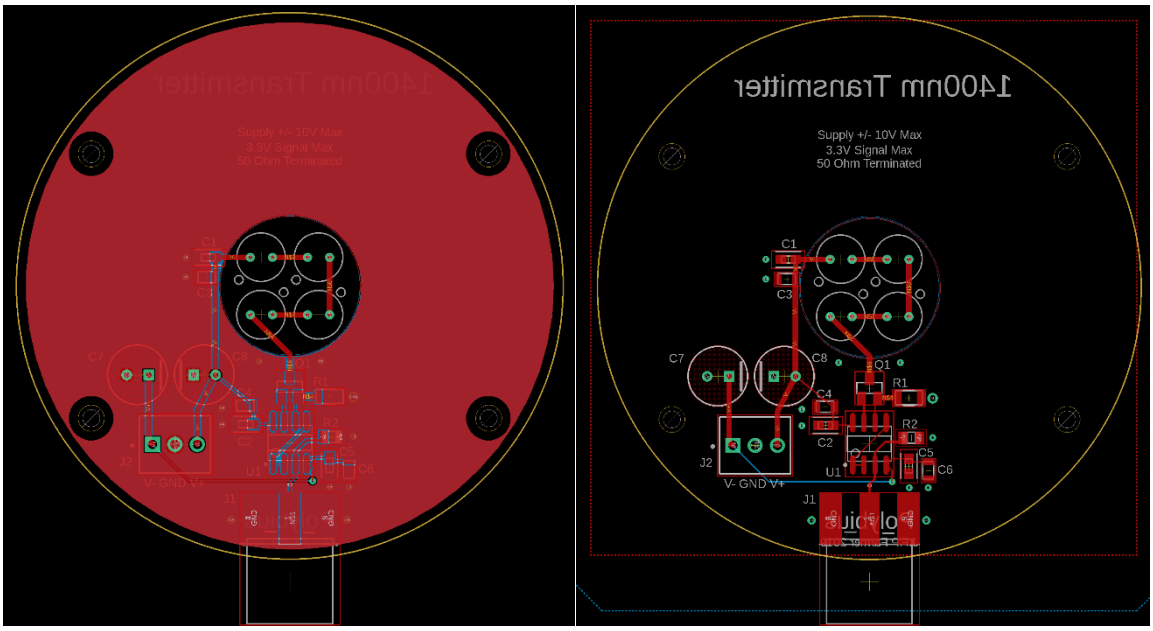



*Figure 35: Pictures of PCB design with ground fill included (left) and excluded (right).*

The design of the transmitter PCB is shown in Figure 35. Careful attention was paid to reducing parasitic capacitance and inductance, which could be introduced by long traces in the signal paths. In addition, care was taken to provide, a ground return for each signal which followed, as near as possible, the original signal path. This is to, where possible, provide the path of least inductance to the signals [94]. Finally, the layout was designed so that the LEDs would be placed in the centre of the board with the signal coaxial connector and power connections (supplying +-5V) along the bottom of the board for ease of access.

### 4.2.3 Protective Casing

To protect and securely hold the LED transmitter, and to prevent touching of the electronics causing potential electrostatic discharge damage, a case was 3D printed from Polylactic Acid (PLA) as can be seen in Figure 36. This was designed on Autodesk fusion 360 CAD software and 3D printed on a Creality CR-10S with a 0.2mm layer height.

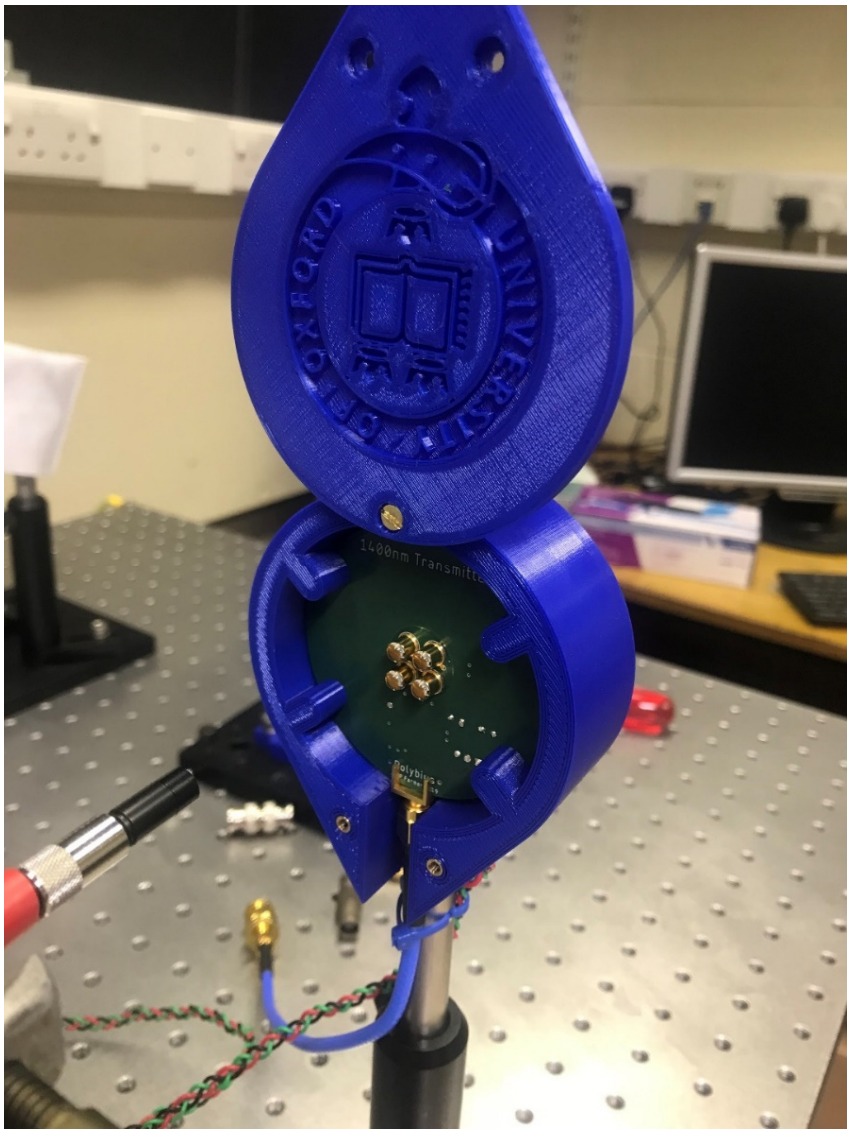



*Figure 36: Picture of complete transmitter with 3D printed surround.*

## 4.3 PERFORMANCE

### 4.3.1 Safety testing

To evaluate the risk to human health, the source was characterized under the lamp standard (BS EN 62471:2008) to provide a risk group for the LED transmitter. To do so, the absolute spectral irradiance was determined at 200mm distance from the source following the standard. The measurement was conducted at the maximum transmitter power by applying a 3.1V DC signal from the Keysight AWG 81150A.

The spectrometer used for this profiling was an Ocean Optics NIR Flame, which was factory calibrated for absolute irradiance measurements, with a 600um diameter fiber and CC-3-UV-S cosine corrector. The absolute irradiance spectrum (see Figure 37) was imported into the Eyelight Optical safety platform software suite. This software characterised the source irradiance according to the lamp standard as risk group 0 (exempt), which is defined as presenting no photobiological hazard.

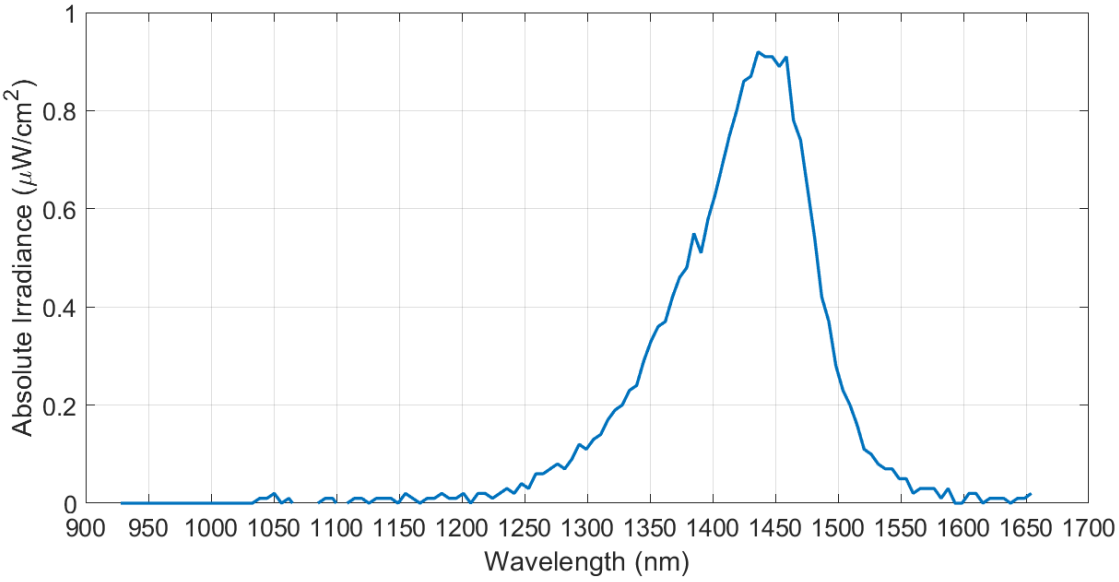



*Figure 37: Absolute Irradiance of 1400nm transmitter at full power (distance = 200mm).*

### 4.3.2 Power measurement

The output power measurement of the transmitter was performed using a Newport 843-R power meter connected to a Newport 919P-003-10 thermophile sensor, with a 10 mm diameter active area and sensitivity between 0.19-11 µm. As with the risk group characterisation, a DC voltage from the 81150A AWG was applied. It was set so that the DC drawn from the transmitter was 50mA to match the test conditions in the LED1450L datasheet. The transmitter was placed as closely as possible to the thermophile sensor (approx.15mm distance). An output power of 4.94mW was measured with a 50mA current drawn, approximately 25% of the expected power, as given in the datasheet [92]. On reflection, after the experimental work was completed, it was found that resistor R2 in Figure 34 limited the voltage drop across the LEDs and consequently the current through the array. With the reduced current through the LEDs, the power emitted by the array was greatly limited. Using a resistor value for R2, which is an order of magnitude smaller, would allow for voltage compliance sufficient to provide the necessary current.

### 4.3.3 Bandwidth

The bandwidth measurement of the transmitter used the PDA20C/M InGaAs receiver (Thorlabs). This receiver was the only available for detection in the 1400nm region, which possessed a sufficient collection area to observe the transmitted signal. Since the transmitter was expected to have a bandwidth similar to the receiver, the attenuation versus frequency data was first measured for the receiver only. The signal source used to characterise the receiver was a 1370nm laser with a bandwidth of 1GHz (Roithner Lasertechnik SPL1370-2-9-PD). The measurement was performed as described in chapter 3 for the hybrid LED (for setup, see Figure 38A). The laser was then exchanged by the transmitter, and the measurement was repeated to determine the transmitter bandwidth (Figure 38B). The measured and inferred attenuation can be seen in Figure 39.

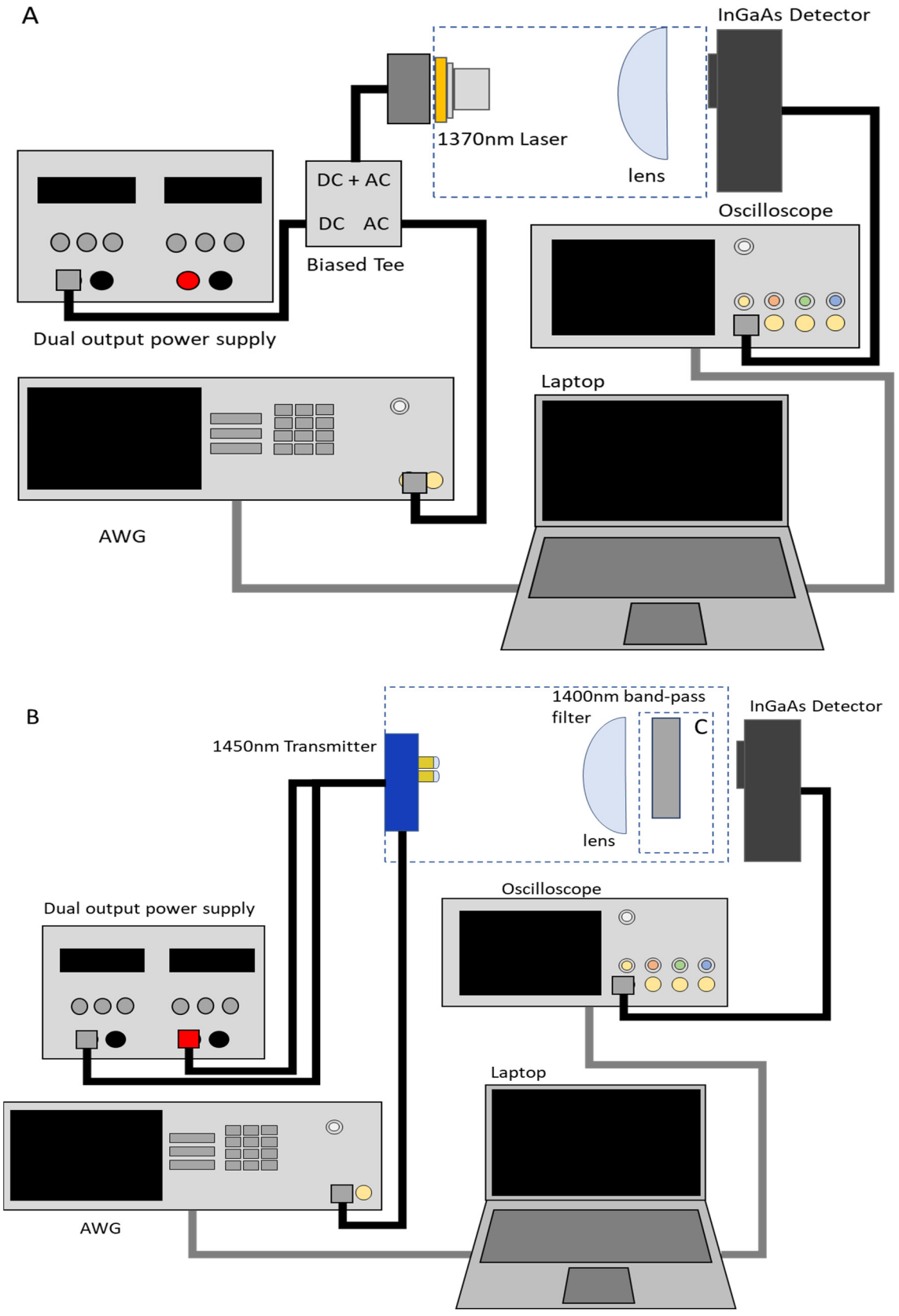



*Figure 38: Diagram of the experimental setups for A: Profiling of the receiver, B: Profiling of the transmitter, and C: Communication test (with the addition of a 1400 bandpass filter).*

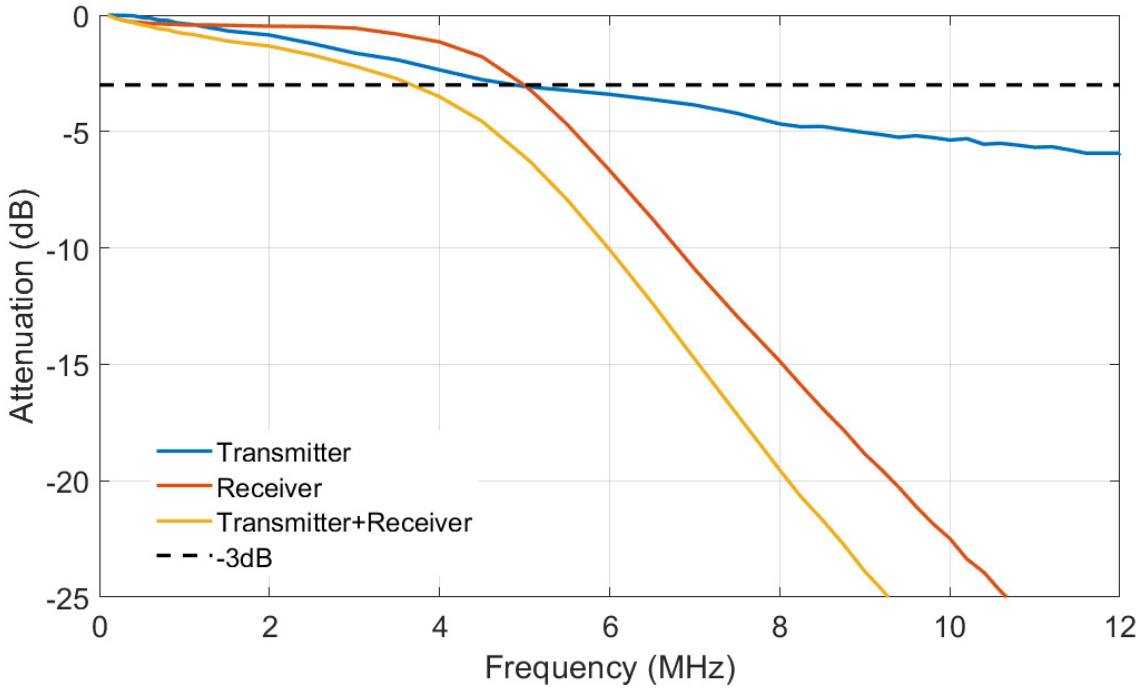



*Figure 39: Attenuation (dB) versus Frequency (MHz) for the receiver, receiver and transmitter combined and transmitter.*

The measured -3dB bandwidth of the receiver (orange curve) is 5.0 MHz, which was within the tolerance of the receiver datasheet. The yellow curve shows the attenuation measured with transmitter and receiver together. In order to obtain the transmitter attenuation, represented by the blue curve, the receiver-only measurements (red) were subtracted from the joint curve. This shows that the transmitter bandwidth is 4.9 MHz. It is worth noting that changes to the circuit outlined in 4.3.2 could increase the transmitter bandwidth which arises from the increased current through the LED sources.

### 4.3.4 Communication Performance

The communication performance using the 1400nm transmitter was first characterised in an indoor environment with dark conditions (no ambient light noise present). A communication test was performed over distances of 1.25m to 5m (see Figure 40). The setup used for this can be seen in Figure 38C, with a 1400nm filter inserted after the collection lens. The experimental procedure is outlined in sections 3.5.1 and 3.5.3. The BER was measured at

different data rates for the various link distances, and the plot of this data can be seen in Figure 41. Over the shortest distance of 1.25m, a data rate of 15.8 Mb/s could be achieved, and with longer distances, the maximum data rate decreased down to 4.5 Mb/s at 5.0m. In comparison, the hybrid LED facilitated a data rate of 1.75 Mb/s over a distance of 0.75m using the same optics and receiver.



*Figure 40: Picture of the experimental set-up for 5m link.*

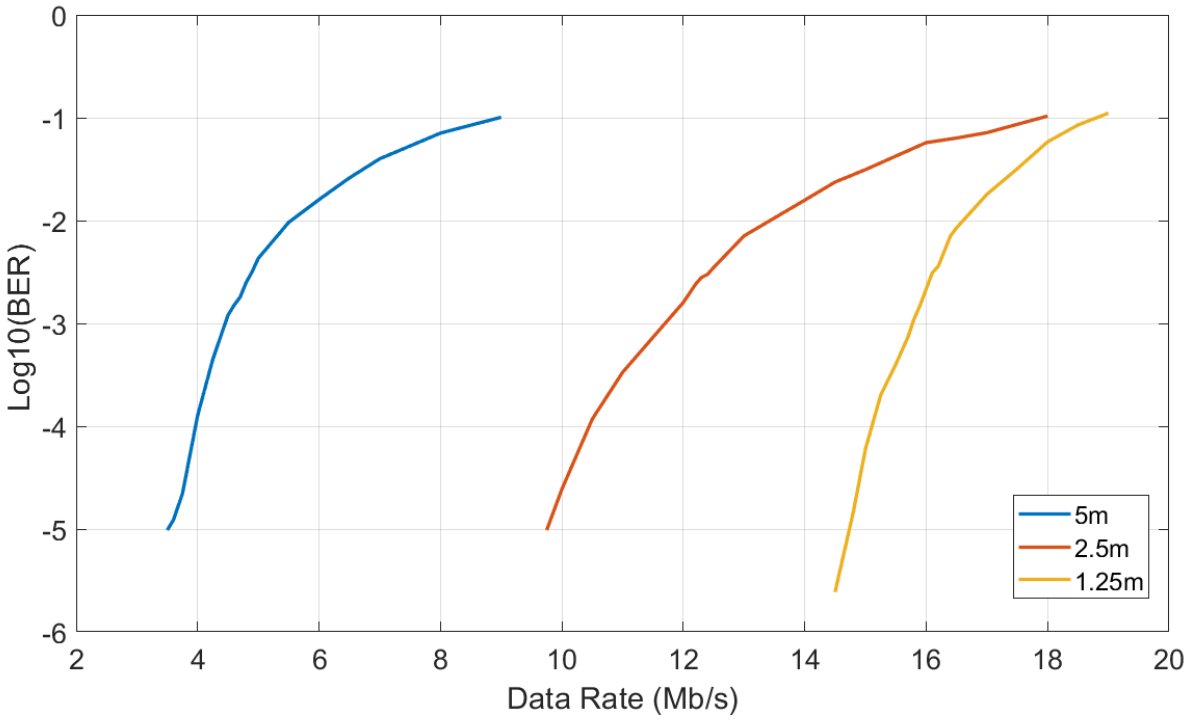



*Figure 41: Log10(BER) versus data rate (Mb/s) over various link distances.*

### 4.3.5 Ambient light mitigation



*Figure 42: Experimental set-up for outdoor 1400nm link experiment. AWG and laptop not shown in image.*

To assess ambient light mitigation, the communication link was set-up again under ambient light conditions on an outdoor platform. To ensure that sunlight could illuminate the receiver throughout the experiment, it was begun just before sunrise, with the receiver placed approximately perpendicular to the sun's trajectory. The experimental setup was initially equivalent to the one used in the indoor environment, as shown in Figure 42, with the link distance set to 5m.

An issue with this set-up was that the collection optic limits the FOV of the detector/lens system to approx. 45° full angle, which, in conjunction with the movement of the sun and the limitations of the outdoor space, would make the alignment of the incident sunlight onto the receiver extremely difficult. In addition, with direct sunlight levels of 81,000 lux obtainable, this would damage the interference filter. As such, the lens was lowered not to obscure the link, and the distance was reduced to 0.25m so that a 1400nm communication link could be achieved without requiring the collection lens. The collected power at the receiver over this reduced link distance was $0.6\mu W$. On-Off keying was used in this experiment to transmit a 4096-bit sequence at a data rate of 10Mb/s, and the BER at various sunlight levels was collected 100 times.

The distributions of the BER from this experiment can be seen in Figure 43. In dark conditions (2.4 lux), the mean BER in 100 trials was $9.4 \times 10^{-4}$, with a standard deviation of $5.1 \times 10^{-4}$. In direct sunlight conditions, the increased ambient light induces a rise in mean to $1.7 \times 10^{-3}$ with a standard deviation of $5.9 \times 10^{-4}$. As such, the observed variations between dark and direct sunlight are within $2\sigma$ of each other.

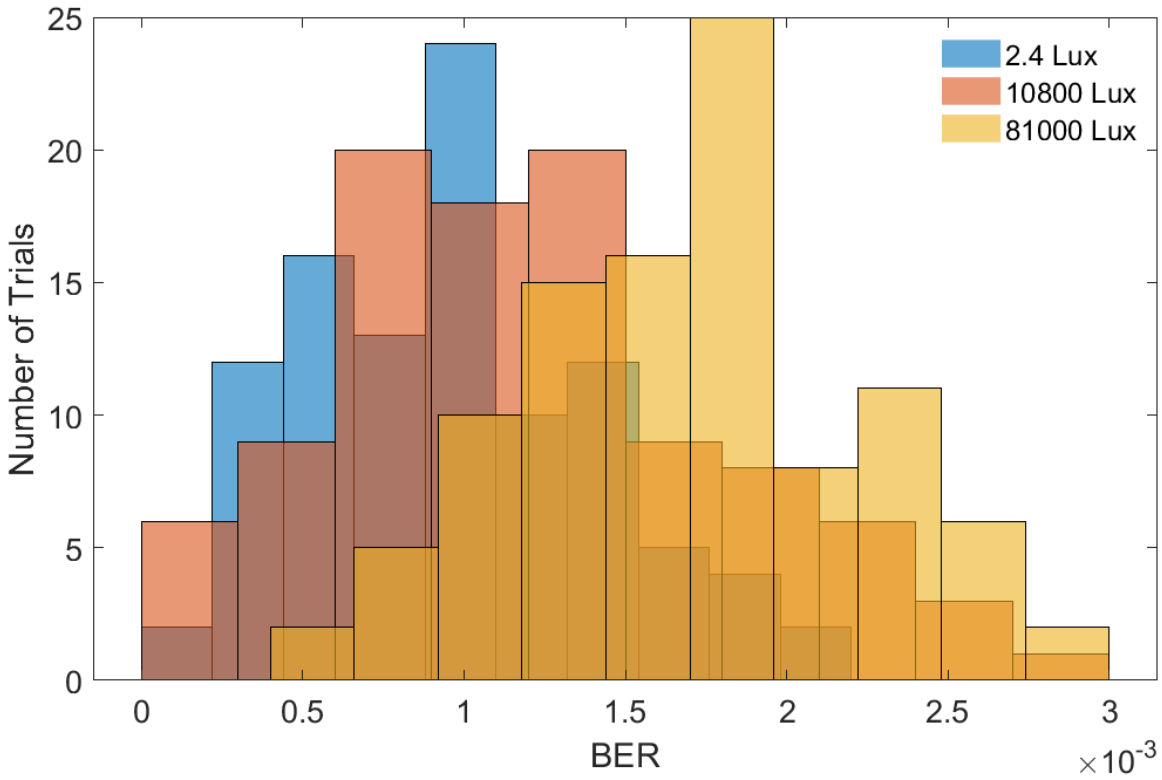



*Figure 43: BER histograms for night (2.4 lux), typical daylight (10800 lux) and direct sunlight (81000 lux) conditions for the 1400nm link over a link distance of 0.25m.*

## 4.4 Discussion

The transmitter constructed in this chapter used readily available commercial parts and aimed at facilitating a communication link at 1400nm over long ranges. From the results conducted in dark-room conditions, it can be seen that a good communication data rate of 4.8Mb/s can be achieved up to 5m. Compared to the previously discussed hybrid LED, this is a significant improvement in both the range and data rate achievable.

Importantly, with the transmitter presented in this chapter, a 1400nm link could be demonstrated outdoors, under direct sunlight conditions approaching the highest illuminance expected in the automotive environment. Figure 43 shows that the link can be maintained without saturation of the receiver or severe impairment to the performance of the link. Taken together with the knowledge acquired using the hybrid LED in Chapter 3, this further increases confidence that 1400nm links allow for sunlight robust

communication. Thus, it is addressing one of the major challenges optical communication faces in the automotive environment.

As suggested by the vehicle safety consortium, discussed in Chapter 2, a minimum data rate of 9kb/s would be expected for the transmission of safety-critical data between vehicles, which could easily be facilitated by the transmitter [8]. Based on the results outlined in this work, a 9kb/s link could be achieved over distances much greater than 5m, for the link system outlined in this chapter. This makes a transmitter based on commercially available LEDs a promising alternative to the hybrid LED proposed earlier. Although the transmitter comes at the cost of an additional light source, which adds to the complexity of the lighting system of vehicles, it could provide a better link performance than the employment of arrays of hybrid LEDs.

For further improvement of the proposed 1400nm link, the power emitted by the source is a crucial factor. As mentioned in Chapter 3, an array of LEDs could be used, for example, together with daylight running lights. Because of the angular dependency of bandpass-filters, which for lasers restrict the receiver FOV, lasers have not been used in this thesis as sources in the 1400nm link. For visible wavelengths, there are filters which minimise passband shifts. With these filters becoming commercially available for the NIR range, lasers could become promising alternatives for LEDs as 1400nm sources. Their higher output power in conjunction with large modulation bandwidths promises to offer long-range communication at high data rates.

## 4.5 CONCLUSION

This chapter introduced a low-cost 1400nm transmitter, based on commercially available components. A 1400nm link using this transmitter was demonstrated over large distances and was also established outdoors. Together with the results obtained with the hybrid LED

in chapter 3, the work in this chapter adds to an increasingly strong case for the deployment of 1400nm links. Such links could address one of the dominant challenges in the field of automotive optical communication, the mitigation of ambient sunlight.

# 5. CHAPTER: FABRICATION METHOD FOR NIR FLUORESCENT CONCENTRATORS

## 5.1 INTRODUCTION

As discussed in the previous chapters, improving signal power and transmitter bandwidth are ways by which the achievable link distances and data rates of a 1400nm link could be improved. In addition, properties of the receiver, such as receiver noise and collection area, are also of critical importance. Using an etendue-limited collection optic to focus more light onto the sensor area comes at the cost of a small FOV, limiting the mobility of the system.

This chapter focuses on the development of a fluorescent concentrator as part of the receiver optics, which is non-etendue-limited and could combine a large FOV with a high signal gain.

In this chapter, the receiver optics of a 1400nm link is examined, focusing on the potential use of a Near-Infrared fluorescent concentrator (NIRFC) as a collection optic. A brief background on fluorescent concentrators (FCs) is given. This chapter then focuses on developing a rapid fabrication method for FCs using resin-based 3D printing. This method is first established for an FC operating in the visible range before expanding the concept towards NIRFCs.

### 5.1.1 Optics of Fluorescent concentrators

Conventional collection optics are etendue limited, meaning that for a given detector area, there is a trade-off between collection area and FOV of the optical system [95]. In the field of optical communication, it is desirable to maximise the collection area of a receiver whilst achieving a large FOV [95]. One way to circumvent Etendue is to employ the use of a fluorescent concentrator as a collection optic [95], such as shown in Figure 44.

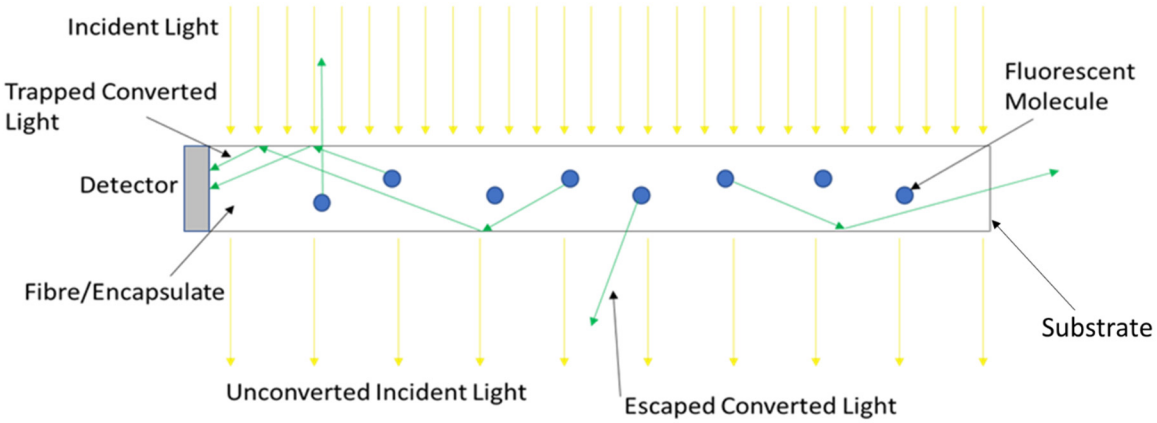



*Figure 44: Ray propagation in a fluorescent concentrator [102].*

The concentrator operates as follows. Firstly, light is incident onto the largest surface of the FC, and a proportion is absorbed by the fluorescent material [96]. After the absorption of an incident photon, the excited fluorescent molecule, after some period, emits a redshifted photon in a random direction [97]. Critically, a proportion of these photons are emitted at an angle so that they are trapped in the transparent substrate via total internal reflection [96]. The critical angle for total internal reflection is set by the refractive index of the fluorescent and the substrate material, and the external environment. A proportion of the trapped light then propagates to a detector located at the edge of the concentrator [97].

There are several loss mechanisms which limit the efficiency of FCs. Firstly, only a certain proportion of the incident light is absorbed by the concentrator. The absorption follows the Beer-Lambert Law and is dependent on the concentration and the extinction coefficient of the fluorescent material and the layer thickness. Of these absorbed photons, only a certain fraction is re-emitted via fluorescence, which is characterised by the Quantum yield (QY) of the fluorescent material [96]. In addition, a proportion of the fluorescent photons will escape the concentrator, as they are not contained by total internal reflection [96]. Finally, depending on the extent of the Stokes' shift, the effective shift between absorption and

emission spectra peaks, a proportion of trapped, down-converted photons will be reabsorbed [97].

The figure of merit to evaluate the performance of FCs is the gain G, as given in Equation 36 [98]. It takes into account the probability of entering the FC $\eta_{enter}$, the probability of light being absorbed $\eta_{abs}$, the quantum yield QY, the probability of a converted photon reaching the detector $\eta_{det}$, and the geometric gain $G_{geo}$. The latter is the ratio of input to output area of the FC (Equation 37).

$$G = \eta_{enter} \times \eta_{abs} \times QY \times \eta_{det} \times G_{geo} \quad (36)$$

$$G_{geo} = \frac{A_{in}}{A_{out}} \quad (37)$$

### 5.1.2 Fluorescent concentrators in optical communication

The development of fluorescent concentrators began in the 1970s, intending to collect sunlight for energy harvesting whilst reducing the required size of solar cells [96]. To date, the majority of research conducted on fluorescent concentrators has been for solar energy harvesting applications. In 2014, fluorescent concentrators were first discussed for employment in optical communication [95]. The modelled FC was based on visible absorbing and emitting CdSe QDs with a ZnS shell and operated at data rates of up to 1Gb/s using OOK. In the simulation, the FC achieved an optical gain of 50 times greater than the geometric gain of etendue-limited CPCs with a comparable field of view [95].

One of the first experimental proofs-of-concept was published in 2016. This work was focused on creating a slab concentrator by fixing the fluorescent material Coumarin 6, mixed in various concentrations with a UV curing resin N0658, between two glass microscope slides [99]. In this work, the group showed that it was possible to achieve a maximum optical gain of 12, whilst also providing a full width at half-maximum FOV of 120° [99]. In comparison, for the best conventional optics, a compound parabolic concentrator (CPC),

with the same FOV, a maximum theoretical optical gain of 3 would be expected [98]. Furthermore, the concentrator possessed a -3dB bandwidth of 41MHz dictated by the fluorescent material employed [99].

In addition, at a similar time, the group in [100] used a series of high bandwidth fluorescent doped fibres, tied together at one end, which were coupled into an Avalanche Photodiode (APD) to create a fluorescent concentrator-based receiver [100]. With such a receiver, the group achieved an optical gain of 12.3 at a -3dB bandwidth of 91MHz [100].

Since this development, much work has been conducted on expanding the functionality of FCs used for VLC. This ranges from creating a dual fluorescent concentrator that can facilitate wavelength division multiplexing [101] to examining the use of fluorescent concentrators as fast Multiple-Input-Multiple-Output receivers [102]. In addition, White light LEDs, as opposed to monochromatic sources, have been used for FC-based communication at a data rate of 38Mb/s using OOK [103]. In [104], a high data rate (300Mb/s) OOK communication over 2m with a receiver Full FOV of 120 degrees has been demonstrated.

Whilst most applications of FCs, including energy harvesting, use fibre and slab-based designs with a homogeneous distribution of the fluorescent material, different distributions of the conversion material have been explored. The model presented in [105] suggests that cladding a plastic optical fibre in a fluorescent material could approximately double the optical gain compared to that of a square slab-based concentrator, with equal collection area and total volume. The work conducted in [106] examined the practicality and performance of such fluorescent clad fibres demonstrating a high optical conversion efficiency.

In addition to the cladding of optical fibres, asymmetrical fibre concentrators have been proposed [107]. In this design, one side of the fibre is asymmetrically shaped. It focuses the

incident light, which is assumed to be collimated, into the fluorescently doped core. The work suggests that such an FC could have a higher optical gain than a fibre with a round or square profile [107].

Apart from optimising fluorescent fibre concentrators, there is work on improving the efficiency of slab-based devices. As part of this, a variety of both QDs and fluorescent molecules dispersed in several different substrates have been tested [96]. The use of multiple layers with different conversion materials has been shown to improve the observed gain [108, 109].

Applications of FCs in the NIR range have mainly aimed at harvesting sunlight more efficiently than visible counterparts, as over 60% of the total sunlight irradiance is at wavelengths greater than 600nm [110]. The fluorescent materials used for these NIR concentrators included NIR-emitting Ytterbium chelates [111], heavy-metal-free ZnS-coated $CuInSe_xS_{2-x}$ QDs [112, 113], and PbS, CdS or CdSe QDs [97, 114, 115]. To date, there has been no research on using them for optical communication.

## 5.2 METHODS

### 5.2.1 Concentrator Fabrication

Although a great deal of work has been conducted using the simple shapes of the slab and fibre-based concentrators, little has currently been published exploring more complex topologies, which might significantly improve fluorescent concentrator performance. This chapter thus, in part, focusses on establishing 3D printing as an FC fabrication method, which will provide the opportunity to rapidly prototype more complex geometries. To minimise the amount of fluorescent material required for the production, a transparent substrate was printed from photo-curable resin and then coated with the fluorescent material suspended in the same resin.

***Substrate Printing***

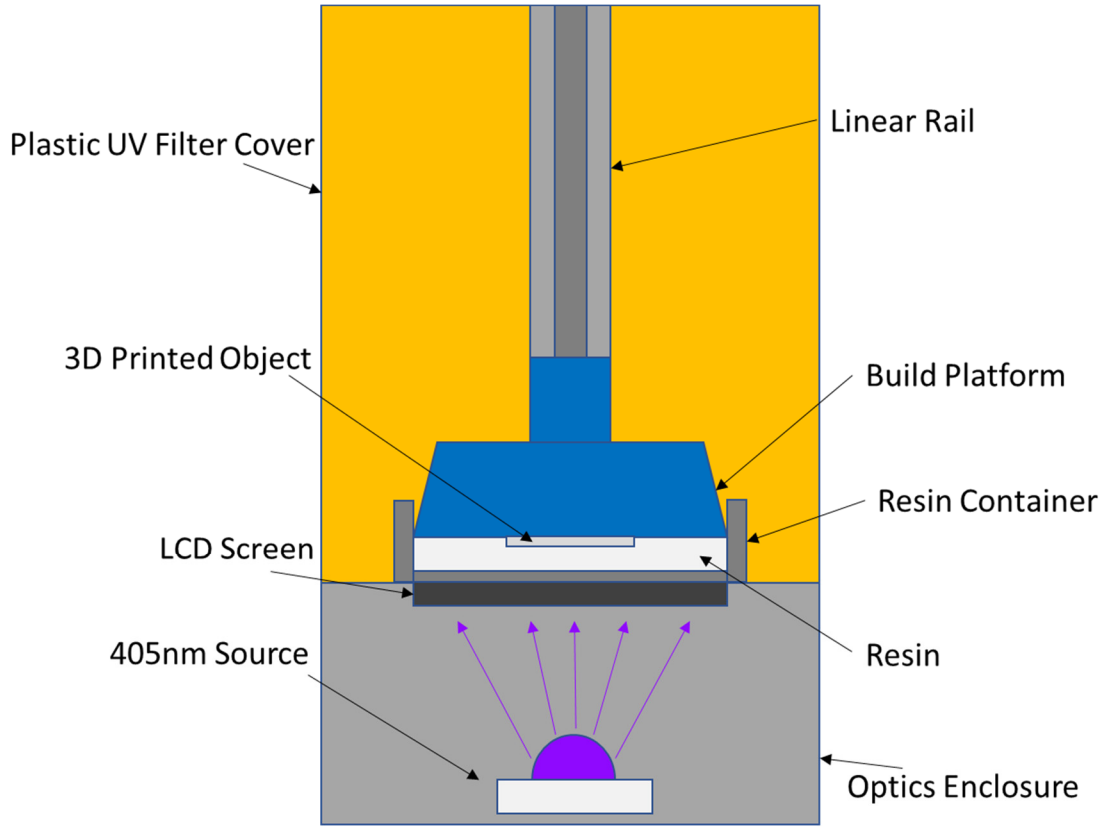



*Figure 45: Cross-section through a DLP printer.*

A resin-based Direct Light Projection 3D printer (Anycubic photon DLP printer) was used to produce custom geometry substrates for fluorescent concentrators. Figure 45 shows a cross-section of the printer, whereby the substrate was built in layers of 25 microns. Each layer is constructed by exposing a 405nm cross-sectional image of the part into the resin container to cure the resin. The build platform is then lifted by one layer, and the process repeated until the part is completed.

The shapes were designed using Autodesk Fusion 360 and sliced into a series of layers using Anycubic Photon Slicer. The printer then exposes these images into the photo-curing resin. Layer by layer, the designed shape is constructed as it is slowly extracted from the resin container. The finished part is then removed from the plate and cleaned in Isopropyl alcohol, followed by a final stage of curing to harden the part under a 405nm source. For the

characterisation of visible fluorescent concentrators, substrates were printed to the size of a microscope slide (75mm x 25mm x 1mm). NIR concentrator substrates were sized to fit the receiver and printed at varying lengths (25mm, 50mm and 75mm x 12.7mm x 1mm). The print time of each substrate was approximately 3 minutes.

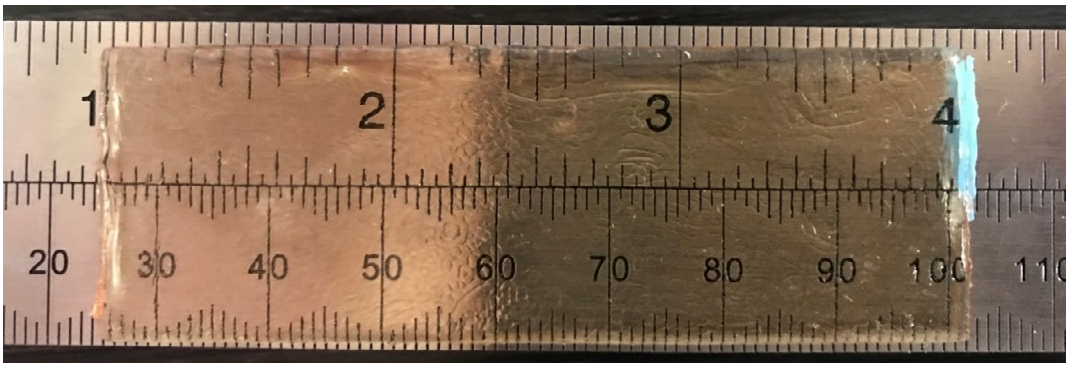



*Figure 46: Clear DLP printed substrate for fluorescent slab concentrator.*

A transparent DLP resin substrate was initially fabricated to evaluate optical clarity and the mechanical properties of the cured resin. As shown in Figure 46, the sample presented a high transparency, although artefacts resulting from the curing process did add distortion areas to the surface.

***Absorption Characterisation***

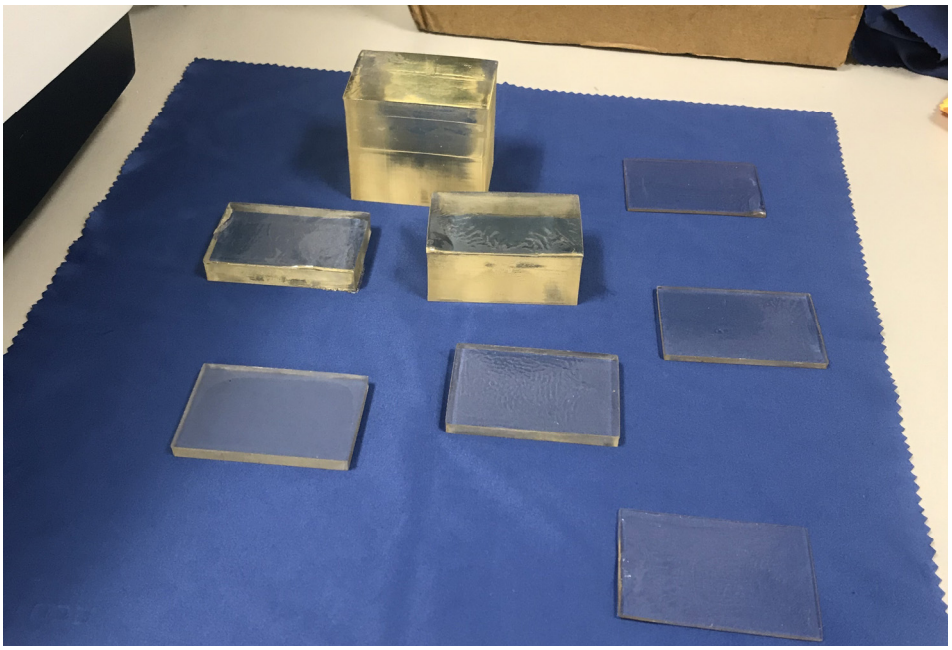


*Figure 47: Set of various substrates of thickness 1-50mm*

To evaluate the absorption characteristics of the resin, substrates of different thicknesses were fabricated from 1-50mm (see Figure 47). The absorption spectrum of the DLP resin was determined using a Lamda 750S spectrometer (Perkin-Elmer). The spectra were measured using deuterium and tungsten halogen lamps at a step size of 5 nm at a slit width of 20nm. The obtained transmission data was corrected against a background spectrum without the samples in place.

***Visible and NIR Fluorescent Coating***

For visible concentrators, 10mg of Coumarin 7 powder was incorporated into 2mL of DLP resin, producing a solution with a concentration of 5 mg/mL. The 3D printed substrate was drop coated with the fluorescent dye/resin solution by spreading it evenly across the surface with a toothpick and finally curing it with a 405nm source for 2 minutes for each side. The fluorescent layer was applied to both sides of the slab.

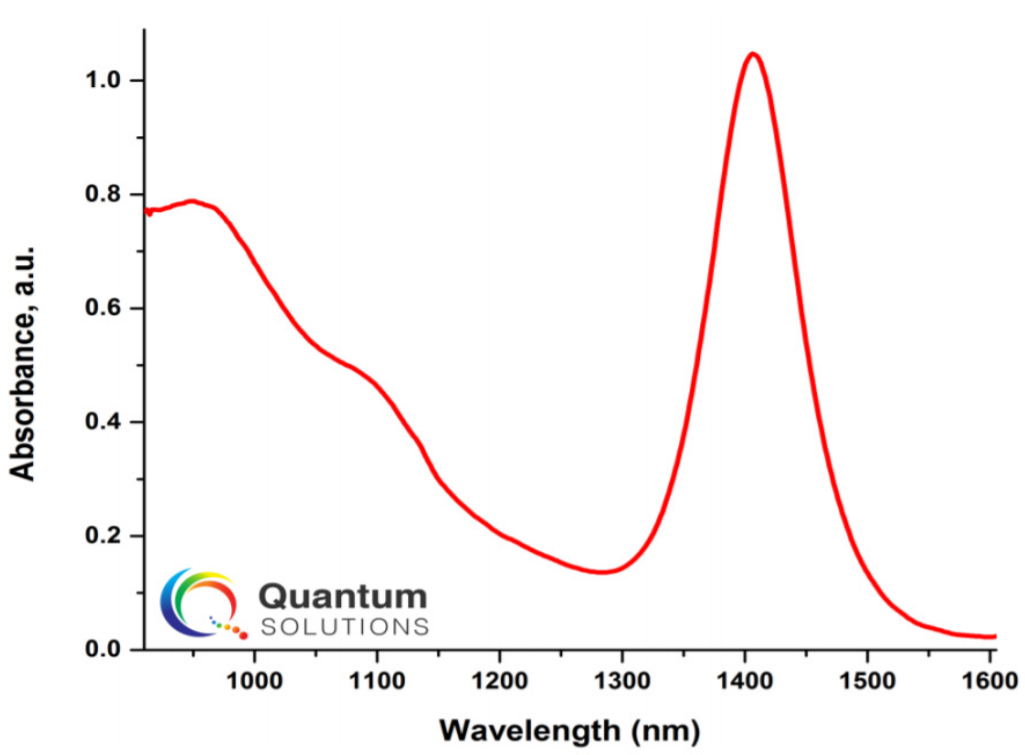



*Figure 48: Absorption spectrum of PbS QDs used for NIR concentrators [78].*

NIRFCs were coated in PbS QDs suspended in the DLP resin. The QDs were purchased from Quantum Solutions and were created to have an absorption peak at 1400nm, as shown in Figure 48 [78]. The QDs were supplied suspended in the solvent toluene at a concentration of 10mg/mL. The QDs were incorporated into the resin, as per the method outlined in Chapter 3 (3.3.2). The concentrations of the resin/QD solution was varied from 1mg/mL to 5mg/mL, and this was in turn applied to the various resin substrates by drop coating and solidified using a UV curer as explained previously.

As can be seen in the absorption spectrum in Figure 48, the QDs absorb in the near infra-red but in addition the UV and visible regions. To ensure this does not compromise the SNR of a link, the employment of a filter would be highly beneficial when using the FC as receiver collection optic.

### 5.2.2 Visible concentrator bandwidth and signal gain measurements

The experimental set-up for the bandwidth measurements can be seen in Figure 49. A 405nm Thorlabs L405P20 20mW laser was used to uniformly illuminate the FC through a Thorlabs Engineered diffuser and 50mm condensing lens. Light from the source illuminates the FC, and the fluorescence photons are detected at an angle of 90° using a Hamamatsu APD module C5658 with a diode diameter of 0.5mm and 1GHz bandwidth. The source was driven from a bias tee supplied with a DC signal from an Aim-TTi EX752M 75V 2A 300W dual output power supply and a swept AC signal from an HP 8712 ET RF network analyser.

The AC signal applied was a 1MHz sine wave with a power of 6dBm, and the DC component was set to $5V$, corresponding to a bias current of 43mA. For the gain measurement, the receiver was disconnected from the network analyser and connected to the Keysight MSO7104B oscilloscope. The received peak-peak voltage was then measured with the FC

in place. For reference, the signal over the same distance is also measured without the FC, and with the receiver directly facing the source.

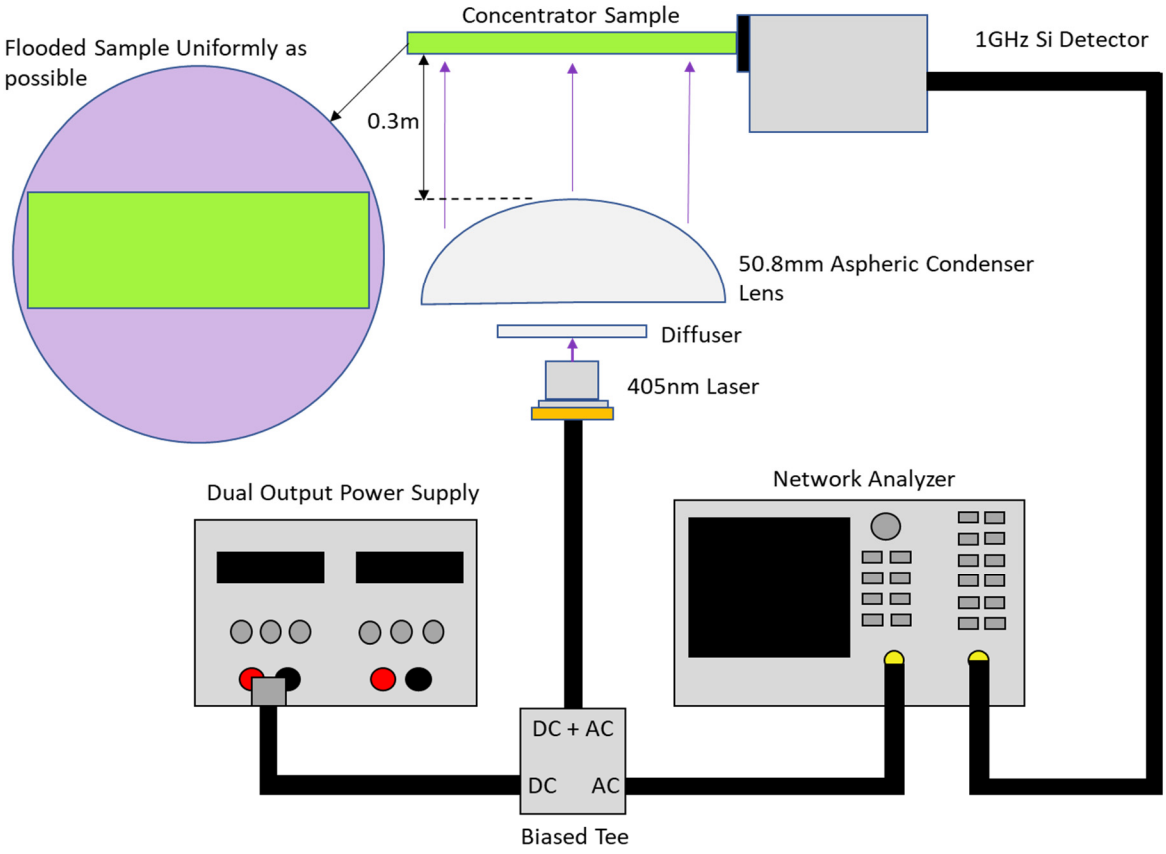



*Figure 49: The bandwidth measurement experimental set-up for the visible FC.*

### 5.2.3 1400nm Illumination

To generate a suitable source to test the NIRFCs, the design of the transmitter in chapter 3 was modified to modulate one 1450nm InGaAsP LED (see Figure 50). The output power test was measured using a Newport 919P-003-10 thermophile and a Newport 843-R power meter. The source emitted 1.9mW at 50mA.

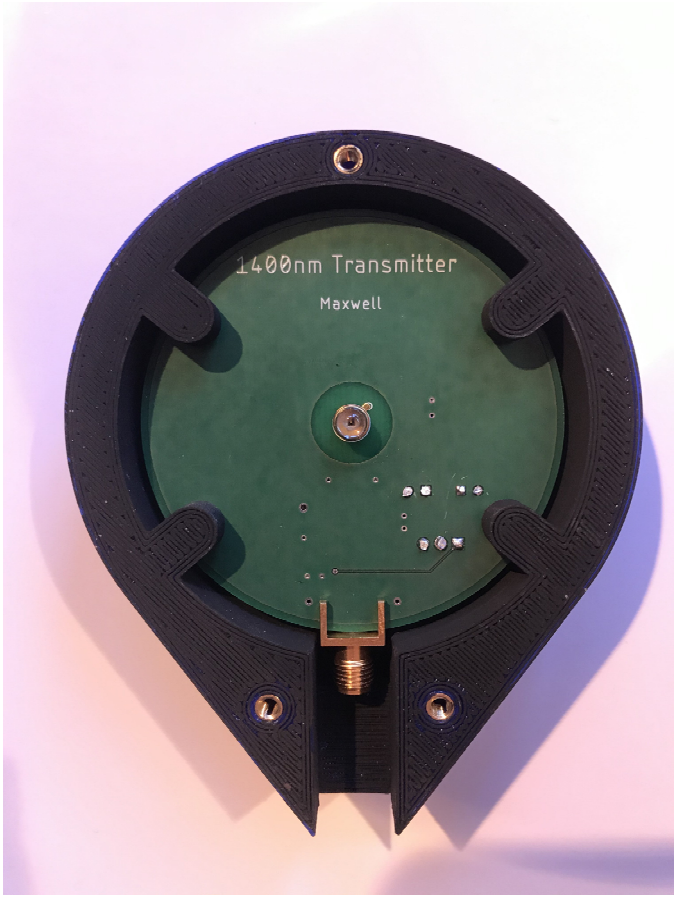



*Figure 50: Image of single 1400nm transmitter used for the NIRFC characterisation.*

## 5.3 RESULTS

### 5.3.1 Substrate Characterisation

The transparent substrate for the FCs was manufactured from the same DLP resin as employed in chapter 3 to encapsulate the QDs. It preserved the QDs' emission properties to a high degree and was therefore deemed a good choice for the substrate material.

The encapsulation in chapter 3 consisted of a relatively thin layer of resin, where the absorption properties would not significantly affect the QD emission. However, the optical path through the FC would be significantly longer and the signal affected to a greater extent by absorptive processes in the substrate material. To characterise their transmission properties, substrates of various thicknesses were printed, and their transmission spectra were measured. The spectra can be seen in Figure 51.

The DLP resin provides good transmission across all samples in the 450-1100nm region. Below 405 nm, a steep decline in the transmission is observed, presumably due to absorption by the photoinitiator in the resin. The absorption characteristics are consistent throughout all tested thicknesses and are well described by the Beer-Lambert-Law (see fitting in Figure 52). For the proposed NIR optical concentrator, absorption at 1500nm, the QD emission peak, was of particular importance. For the signal travelling through the concentrator, the optical path is assumed to be similar to the concentrator length.

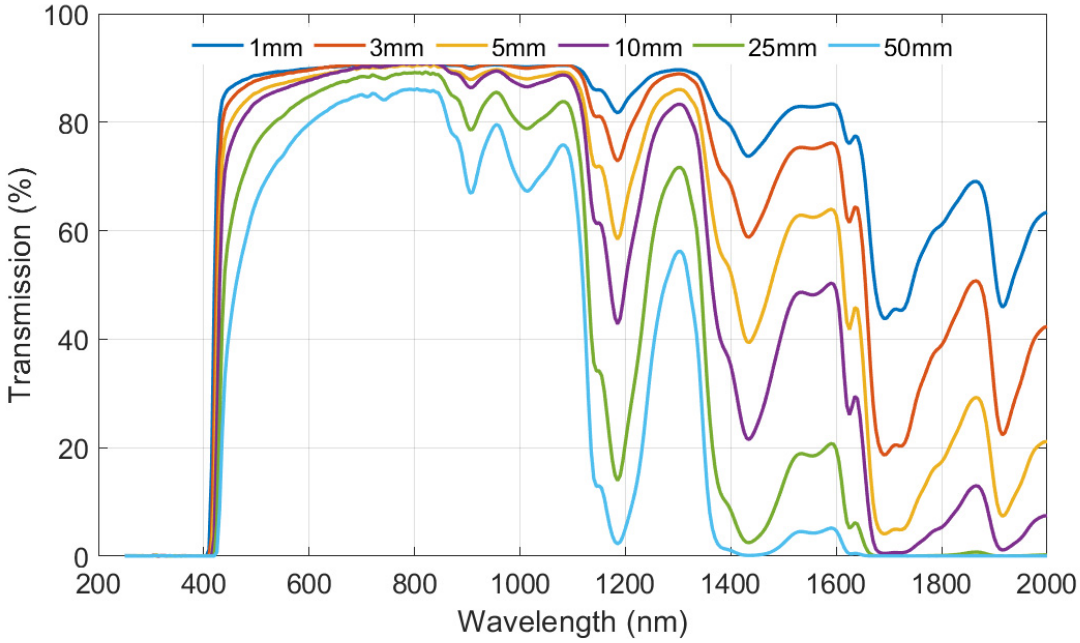



*Figure 51: Transmission (%) versus Wavelength (nm) for resin samples of a 1-50mm thickness.*

Figure 52 shows cross-sections through the data in Figure 51 for selected wavelengths. For 1500nm, a thickness of 10mm reduced the transmission to 50% and above a thickness of 30mm, less than 10% of the signal is transmitted. The transmission through the DLP resin at visible wavelength between 450-1100nm is significantly higher. At 480nm, the emission wavelength of Coumarin 7, paths of 50-70mm will still transmit above 50%. This makes the DLP resin a very promising substrate material for FCs operating in the visible range.

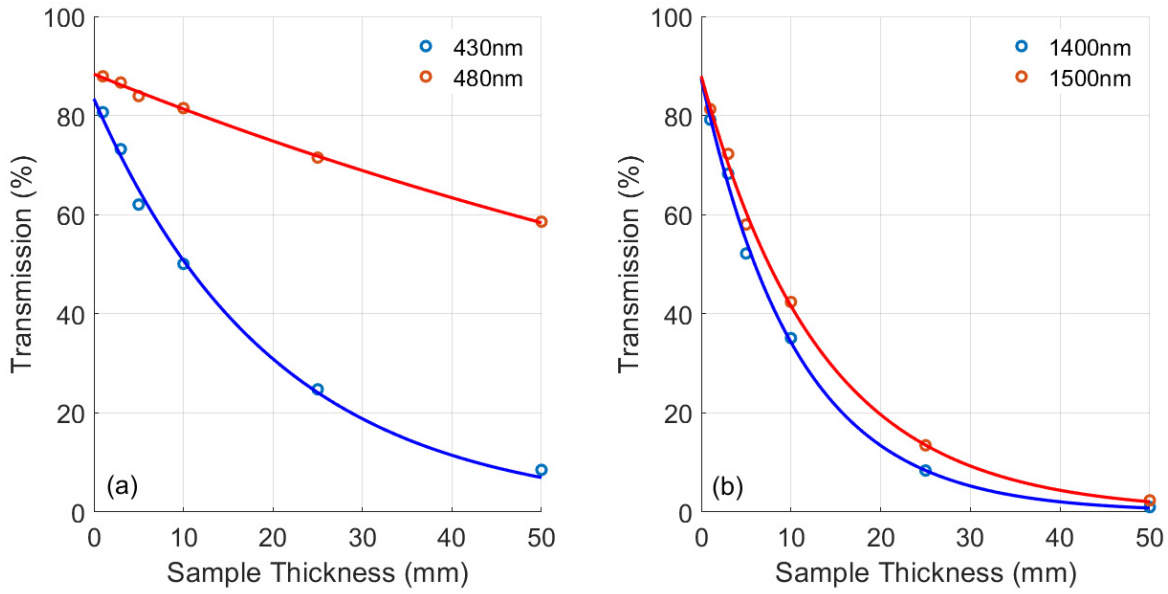



*Figure 52: Resin transmission versus sample thickness for absorption (blue) and emission wavelengths (red) of (a) Coumarin 7 and (b) PbS QDs, including Beer lambert law fitting.*

For both materials, the transmission at the emission wavelength is higher than at the absorption. Therefore, it is desirable to convert the incoming signal directly at the FC surface, with the transmission for the fluorescence photons being higher than for the incoming. This was another reason to adopt coated concentrators, where a thin layer of highly concentrated fluorescent material is applied to the transparent substrate.

### 5.3.2 Visible Concentrators using Coumarin 7

Because of the transmission properties of the DLP resin, for the initial establishment of the fabrication method, the use of visible fluorescent materials was considered to offer practical, safe, and inexpensive prototyping. This had the additional advantage that the coating process can be easily visually evaluated and optimised before a NIRFC is fabricated.

For this, several visible fluorescent materials were explored. These were chosen due to being non-polar, and this was therefore suggestive of solubility in the DLP resin, allowing for the homogeneous incorporation. The only tested material which was homogenously soluble in the DLP resin was (3-(2-Benzimidazolyl)-7-(diethylamino)coumarin), also known as Coumarin 7. This material is used for applications such as fuel and oil dying in automotive

applications and is comparatively inexpensive. Thus, an initial concentrator was fabricated using Coumarin 7.

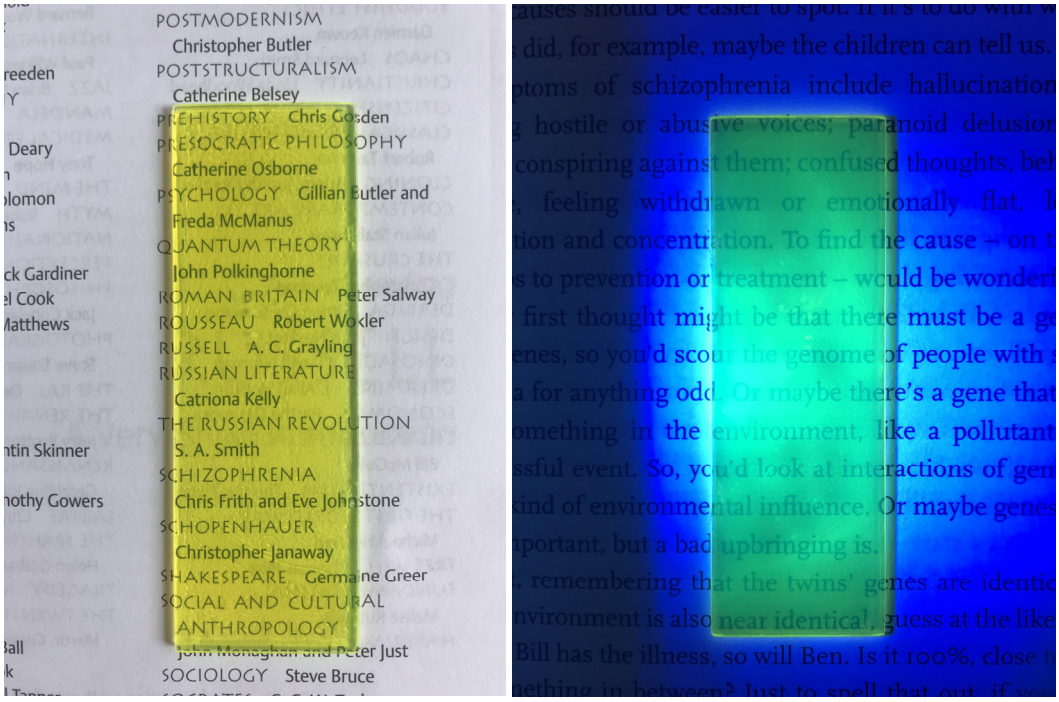



*Figure 53: Images of completed fluorescent concentrator with and without illumination from a 405nm source.*

The 3D-printed slab substrate was coated in a 5mg/mL solution of Coumarin 7 and DLP resin and cured under a 405nm lamp. The resulting concentrators can be seen in Figure 53. Compared to the substrate alone, Figure 46, the optical clarity could be maintained after the drop-coating process, and fluorescence observed when illuminated by a 405nm source (right). Notably, the edges showed a brighter fluorescence, suggesting that it has light-concentrating properties.

More complex shapes were also created, which were coated by dragging the substrate through the fluorescent solution. Two examples of this work are shown in Figure 54, producing a fibre concentrator and a spiral topology. These examples illustrate how 3D printing can fabricate topologically complex custom FCs, which offer flexibility in design and could improve signal gains compared to planar concentrators.

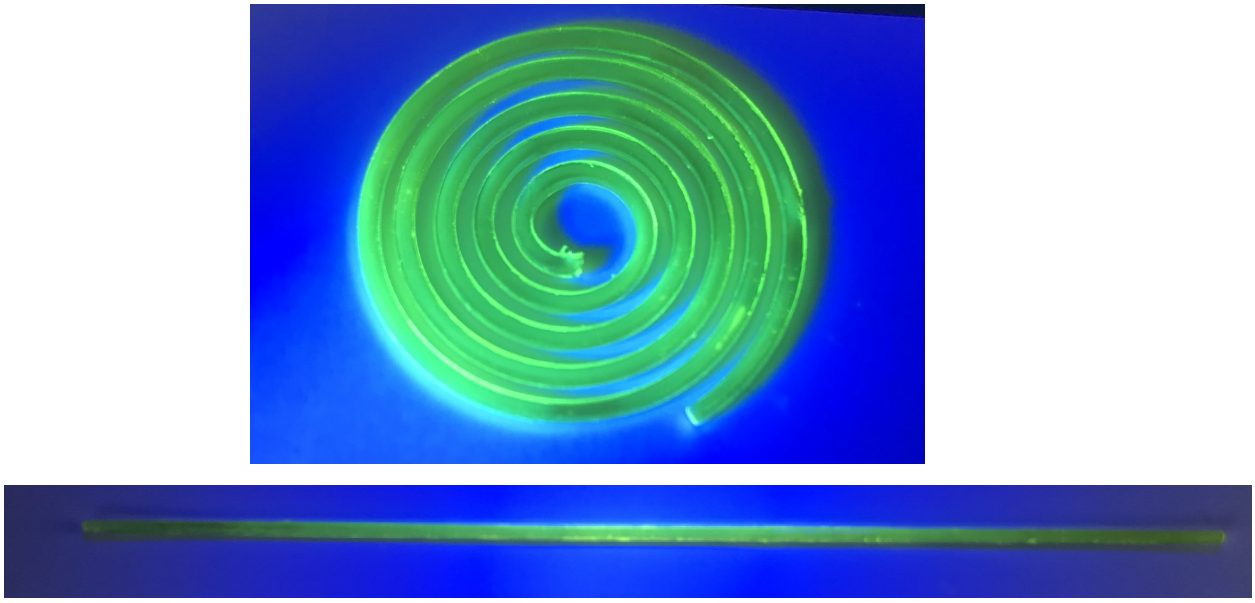


*Figure 54: Spiral and fibre-based fluorescent concentrators.*

### 5.3.3 Visible Concentrator bandwidth and signal gain

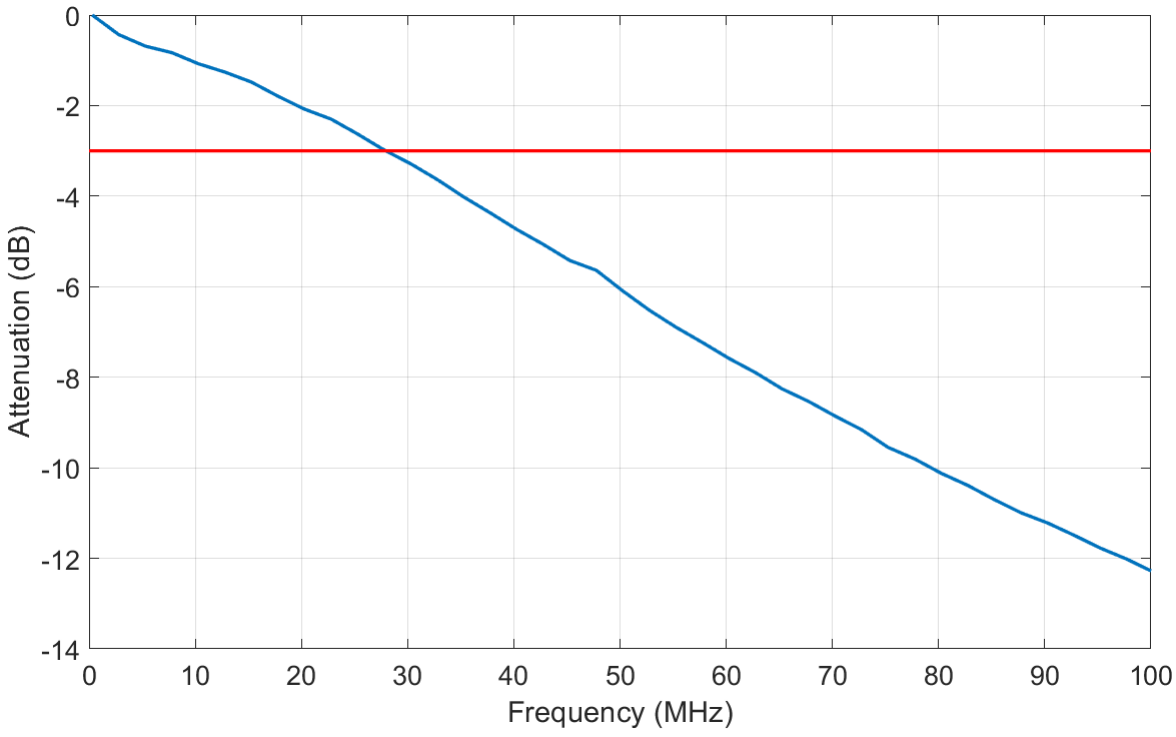



*Figure 55: Attenuation versus Bandwidth for 3D printed visible Fluorescent Concentrator.*

Following the fabrication, an experiment was conducted to evaluate the performance of the rectangular visible concentrator. Firstly, the -3dB bandwidth of the material was measured

by placing the concentrator against the detector and illuminating it with the laser source, as shown in Figure 49. The -3dB bandwidth was measured to be 27.8MHz, as can be seen in Figure 55. In comparison, using Coumarin 6 as a fluorescent material suspended in a clear resin (NOA68, Norland) at a concentration of $1\ mg/mL$, which has been used it the Oxford group's previous work on fluorescent concentrators, had a bandwidth of $41MHz$ [99].

In addition to the bandwidth, the signal gain for the FC was measured. This is the ratio of the signal collected with the employment of the concentrator to that of the signal measured by shining light directly onto the detector over the same link distance (30cm). Using the rectangular concentrator shape, as seen in Figure 53, a signal gain of 4 could be achieved. The experiments performed with the visible concentrator shows that 3D-printed FCs can provide a promising bandwidth and signal gain useful for optical communication.

### 5.3.4 NIR Concentrators

***Transmitter Characterisation***

The transmitter was designed according to the circuit layout presented in Chapter 4 but using only one LED. The bandwidth of the transmitter was profiled, as seen in Figure 56, where the -3dB intersection is at 3.5MHz. As measured in Chapter 3, the bandwidth of the QDs in the resin encapsulant was 545kHz, much less than the transmitter bandwidth. The peak output power of the transmitter was 1.9mW at 50mA.

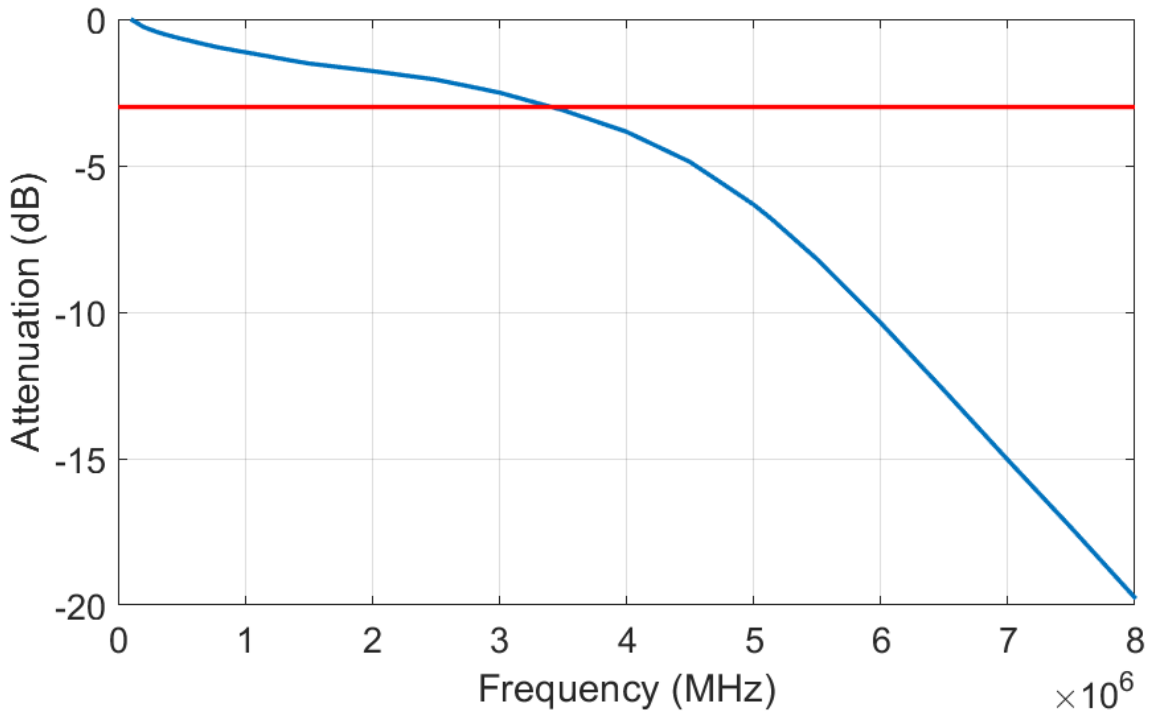



*Figure 56: Attenuation versus Frequency (MHz) for a single LED transmitter with -3dB line (Red).*

***NIRFC testing***

The substrates were printed at a width of 12.7mm to fit directly onto the detector, which is recessed into the receiver. A series of different lengths were fabricated (25mm, 50mm and 75mm) with a thickness of 1mm.

The fluorescent QD coating was applied at different concentrations, ranging from 1 mg/mL to 5mg/mL. It was challenging to produce homogeneous samples at the various concentrations. During curing, the QDs within the applied solution typically exhibited some clumping, despite illuminating the samples uniformly with a UV curer. From this work, the samples with the greatest homogeneity were at a concentration of $3mg/mL$.

To test the generated NIRFCs, an experiment to determine the signal gain was conducted when comparing each sample to a bare detector placed at a fixed distance (0.3m) from the transmitter. A 100kHz sine wave with an amplitude of 3.1Vpk-pk and an offset of 1.6V was applied to the system using an Agilent AWG 81105A. The Thorlabs PDA20C/M collected

the received signal from the NIRFC and was connected to a Keysight MSO7104B oscilloscope.

In this setting, no signal could be detected at the receiver. The link distance was reduced to 21cm, but only stray light reflected from objects nearby was detected. Other samples with increased concentrations of PbS QDs at 4 $mg/mL$ and 5 $mg/mL$ were tested, but again no signal could be detected.

Several effects could have contributed to this: Firstly, the conversion efficiency, which is determined by the extinction coefficient of the substrate at 1400nm, along with the QY and concentration of the QDs. Secondly, given the low transmission of the DLP resin for light at 1500nm, it was also expected that any signal would be significantly attenuated whilst passing through the substrate. Finally, the large-area detector employed in this experiment exhibited a significant noise floor, from which any potential signal could not be distinguished even with oscilloscope averaging.

## 5.4 DISCUSSION

### 5.4.1 Functional 3D Printed Fluorescent Concentrator

The proposed 3D printing-based fabrication method allowed the production of substrates with high optical clarity. For the visible Coumarin 7-coated concentrator, a signal gain of 4 was measured. For comparison, a commonly used solid CPC with a FOV of 120°, would provide a signal gain of 3 [98]. Within the limits and imperfections in the fabrication process, a 3D-printed optical concentrator can provide a higher signal gain, serving as a proof-of-principle at this stage. The work presented in this section is, to best of the author's knowledge, the first demonstration of a working 3D printed fluorescent concentrator.

In order to improve performance in the future, optimisation work on the fabrication process as well as the shape and illumination source used is possible. Importantly during the 3D

printing fabrication, the sample edges were not polished before the experiment was conducted, which if executed, would most likely increase the signal gain making such a method of fabrication increasingly attractive. In addition, the 3D printed concentrator signal gain is likely higher than the measured result, as a 405nm laser source was used for illumination. 405nm, as can be seen in Figure 51, is not the optimum wavelength to interrogate the concentrator due to the low transmission of the substrate used.

In addition, from studies of coumarin 7 in ethanol, the absorption spectrum peak is around 430nm, although this could vary slightly depending on the encapsulate medium used [116]. The DLP resin transmission improves significantly when the incoming radiation is at a wavelength of ≥430nm (Figure 51). By using a 430-450nm source instead of 405nm, the signal gain would be increased.

Regarding surface quality, it can be seen in Figures 53 that the sample possessed a good homogeneity without fluorophore aggregation. However, there were some surface artefacts created from the non-curing process. This could be resolved by decreasing the intensity of 405nm light whilst curing over a longer time period and attempting to illuminate the sample more uniformly during curing.

By exploring the fabrication of various shapes, the versatility of the 3D printing-based fabrication method could be shown. The production of a spiral has so far been the most complex topology created using this method. Even though this shape could be fabricated using other methods, the production time for the substrate of approximately 5 minutes and the achieved precision in this work is superior to casting in moulds or using comparable techniques. Theoretically, 3D printed concentrators could be fabricated with a much higher level of complexity, whereby additive fabrication is the only feasible production method.

Overall, this work shows great promise for the future of fluorescent concentrator fabrication, laying the groundwork for considerably more ambitious designs.

### 5.4.2 NIR Fluorescent Concentrators

In the NIRFC work conducted, it was not possible to distinguish a signal from the noise level. The lack of signal gain could be attributed to two major issues:

Although the clear Anycubic photon resin has good optical transmission in the visible to NIR range (450nm-1100nm), the transmission further into the NIR is significantly reduced, especially in the 1500nm region at the peak of the QD emission spectrum. This suggests that a large proportion of the signal is absorbed whilst propagating through the FC. Creating a NIRFC using QDs which emit at 1300nm (absorption at approx. 1200nm) could circumvent this issue due to the high transmission even for large sample thicknesses (50mm transmission of 55%). For a 1400nm communication link using a NIRFC, other 3D printer resin materials, which might offer better optical performance in this region, could significantly improve performance.

Additionally, a low conversion efficiency of the fluorescent layer could contribute to a signal too low to be detected. To increase the signal, the QD concentration in the coating of the NIRFC could be increased. However, this could interfere with the creation of homogeneous layers. The concentrator coated in 3mg/mL QD suspension was reasonably homogeneous, but no signal was detected. When increasing the QD concentration, most samples exhibited an aggregation of QD matter on the substrate during the curing process. As mentioned in Chapter 3, aggregation of the QDs could vary the optical properties of the QD and therefore the efficiency of the fluorescent conversion. Optimising the conversion efficiency could be a critical step towards realising a NIRFC.

## 5.5 CONCLUSION

The work in this chapter has outlined an investigation towards the fabrication and testing of NIRFCs to be used in the receiver of a 1400nm link.

Using Coumarin 7 as fluorescent material, a fluorescent concentrator operating in the visible range could be produced. It exhibited a good signal gain of 4 without optimisation of the material, fluorophore concentration or concentrator shape. With a bandwidth of around 30 MHz, the 3D-printed concentrators are, with optimisation, promising candidates for employment in VLC links.

By employing QDs emitting at 1500nm, the working principle was expanded into the NIR range. However, it was not possible to collect a signal from these FCs, which can partly be attributed to the high absorption of the substrate material, and possibly also the inhomogeneity of the QD layer applied. With the optimisation of the substrate material and further development of curing techniques, it seems highly probable that 3D printed NIRFCs could be realised.

This chapter has presented a versatile fabrication technique for creating fluorescent concentrators for optical communication. To the best of the author's knowledge, this is the first time FCs have been fabricated using 3D printing. The technique allows for the custom fabrication of complex geometries, which could also provide the option of manufacturing FCs to fit a specific setup or device, which will be spatially constrained. Furthermore, it allows for a high turnover of prototypes, and could thus be a critical factor in optimising current FC technology. To date, FC topologies have been limited to relatively simple shapes, most commonly fibres or slabs. With the use of 3D printing, the spatial complexity of an FC is no longer limiting realisation. In future work, significantly higher gains could be reached by employing optimised topologies.

# 6. CHAPTER: CONCLUSION AND FUTURE WORK

## 6.1 CONCLUSION

This work has presented an investigation into the use of 1400nm optical communication in the automotive environment. The rise of autonomous and semi-autonomous vehicles offers the opportunity to address the large number of fatalities and costs associated with accidents involving human error. In order to establish a collective network of cars, which is able to exhibit swarm-intelligence in various traffic situations, a reliable and practical communication system is required. Optical Wireless Communication (OWC) is a promising candidate for a safe, reliable, and practical automotive communication system, which would need to address the following challenges:

1. Creating a robust link which tolerates high ambient light conditions which can also be subject to rapid change. In addition, such link requires robustness to adverse weather conditions such as fog and rain.
2. Providing a communication link over typical inter-vehicular distances up to 100s of meters
3. Providing data rates that allow for the transmission of safety-critical data, possibly also extended applications (multimedia, map sharing)
4. Providing mobility with a FOV that is suitable to allow for typical vehicular movement between sender and receiver.

This thesis addresses the named challenges by suggesting the operation of an optical link at 1400nm. The strong absorption of sunlight by water vapour at close to 1400nm creates a wavelength band where optical links can operate with substantially lower ambient sunlight noise than in the visible region. By providing sunlight-robust communication, a 1400nm link would also provide relief to the other issues discussed.

The developed link budget model in chapter 2 provided the groundwork to assess a communication system operating at 1400nm based on automotive lighting infrastructure. According to the simulations, this link could exhibit a high robustness to ambient sunlight, whilst still being reliable in adverse weather conditions.

For the experimental implementation in chapter 3, a custom hybrid LED was designed and developed, which facilitates two optical links in parallel, one of which is at 1400nm and was tested under high ambient light conditions. To the best of the authors' knowledge, this is the first time that both a visible and NIR link (1.75Mb/s at 1400nm and 41Mb/s at 450nm) have been facilitated within the same source.

Using a second, dedicated NIR transmitter in chapter 4, the range of communication of the 1400nm link could be expanded to 5m at a data rate of 4.5Mb/s. Notably, this transmitter could facilitate the link in an outdoor environment in direct sunlight conditions without saturation of the receiver or substantial changes to the BER. Taken together, the experiments performed in these chapters provided evidence that sunlight-robust optical communication links at 1400nm can be achieved, making this optical band promising for future automotive communication technologies.

Finally, in chapter 5, consideration was given to using FCs to improve the 1400nm link performance at the receiver. Using 3D-printing, a visible proof-of-concept FC was fabricated, which provided a signal gain of 4. The work in this chapter demonstrated the potential of 3D-printing to produce FCs with custom topologies and configurable fluorescence properties. By increasing the collected signal power, FCs could contribute to increasing link distances and data rates of a 1400nm link, whilst not limiting the FOV.

In summary, this thesis has outlined the conception and development of a sunlight robust communication system at 1400nm. This addresses the major challenge of ambient light

mitigation and would allow for the improvement of mobility, data rate and link distance. With a 1400nm-region communication system, autonomous and semi-autonomous vehicles could be equipped with a practical, reliable and secure communication system, contributing to road safety and traffic management.

## 6.2 FUTURE WORK

From work discussed in this thesis, there are several points across the various chapters which could be expanded upon in the development of a 1400nm communication system.

For an improved modelling of the 1400nm link, experimental determination of the extinction coefficient of the atmosphere at 1400nm would be beneficial. This could be achieved by setting up a 1400nm link in a several-meter-long chamber, in which the humidity and temperature can be carefully controlled. Such an experiment could verify the effects of the various atmospheric conditions modelled in this thesis.

Future developments of the hybrid LED and the fluorescent concentrator will have significant overlap. For improvement of the conversion efficiency, other fluorescent and substrate/embedding materials could be evaluated. The resin should not show significant absorption in the NIR, to allow for optimal signal transmission in the NIRFC and the Hybrid LED. For the choice of fluorescent material, particular attention should be given to a high QY, as well as high photostability, low toxicity and low environmental hazard. In the hybrid LED, the emission properties could be improved by applying the fluorescent material directly to the LED, together with the already employed phosphors, which compose the white light emission.

General improvements to the FC fabrication method may include other techniques for incorporating the fluorescent material, including dip-coating and the homogeneous

incorporation directly into the substrate. Additionally, 3D printing offers a high degree of flexibility regarding the FC geometry, and an investigation could be conducted to exploit this feature, leading to further improvement of the optical gain over current topologies.

Towards a higher level of technology readiness, and to improve data rates and link distances, laser-based systems could be evaluated as an alternative to LED sources. By investigating bandpass filters with low angular dependency, the limited FOV of a laser-based system could be increased. In addition, independent of the source employed, future research in automotive OWC will need to demonstrate the ability to facilitate multiple users, for example, by using FDM schemes with multiple-transmitters-single-receiver links.

# REFERENCES

[1] Save LIVES - A road safety technical package. Geneva: World Health Organization; 2017. ISBN: 9789241511704

[2] "Road Safety Factsheet - Road Crashes Overview", ROSPA, 2017. [Online]. Available: https://www.rospa.com/rospaweb/docs/advice-services/road-safety/road-crashes-overview.pdf [Accessed: 25- June- 2020].

[3] " The World's Most Experienced Driver™", Waymo, 2017. [Online]. Available: https://waymo.com/tech/ [Accessed: 2- July- 2020].

[4] "Autopilot", Tesla.com, 2017. [Online]. Available: http://www.tesla.com/en_GB/autopilot [Accessed: 2-July-2020].

[5] L. Murray, "Look no hands! [Transport Testing Driverless Cars]," in Engineering & Technology, vol. 12, no. 2, pp. 42-45, March 2017

[6] S. H. Yu, O. Shih, H. M. Tsai, N. Wisitpongphan and R. D. Roberts, "Smart automotive lighting for vehicle safety," in IEEE Communications Magazine, vol. 51, no. 12, pp. 50-59, December 2013.

[7] D. Karunatilaka, F. Zafar, V. Kalavally and R. Parthiban, "LED Based Indoor Visible Light Communications: State of the Art," in IEEE Communications Surveys & Tutorials, vol. 17, no. 3, pp. 1649-1678, thirdquarter 2015.

[8] A. Căilean and M. Dimian, "Current Challenges for Visible Light Communications Usage in Vehicle Applications: A Survey," in IEEE Communications Surveys & Tutorials, vol. 19, no. 4, pp. 2681-2703, Fourthquarter 2017.

[9] A. Cailean, M. Dimian and A. Done, "Enhanced design of visible light communication sensor for automotive applications: Experimental demonstration of a 130 meters link," 2018 Global LIFI Congress (GLC), Paris, 2018, pp. 1-4

[10] S.-A. Avătămăniței, A.-M. Căilean, A. Done, M. Dimian, V. Popa, and M. Prelipceanu, "Design and Intensive Experimental Evaluation of an Enhanced Visible Light Communication System for Automotive Applications," Sensors, vol. 20, no. 11, p. 3190, Jun. 2020.

[11] Satoshi Okada, Tomohiro Yendo, Takaya Yamazato, Toshiaki Fujii, Masayuki Tanimoto and Yoshikatsu Kimura, "On-vehicle receiver for distant visible light road-to-vehicle communication," 2009 IEEE Intelligent Vehicles Symposium, Xi'an, 2009, pp. 1033-1038

[12] T. Yamazato et al., "The Uplink Visible Light Communication Beacon System for Universal Traffic Management," in IEEE Access, vol. 5, pp. 22282-22290, 2017

[13] Y. Kaymak, S. Fathi-Kazerooni and R. Rojas-Cessa, "Indirect Diffused Light Free-Space Optical Communications for Vehicular Networks," in IEEE Communications Letters, vol. 23, no. 5, pp. 814-817, May 2019

[14] S. Han, C. Wang, G. Li and N. Chi, "A 427.5 Mbps Automotive Headlight Visible Light Communication System Utilising 64QAM-DMT Modulation with Software Pre-equalization," 2019 IEEE/CIC International Conference on Communications in China (ICCC), Changchun, China, 2019, pp. 169-172

[15] Jin Sung Yooun, Choi Dongnyeok, Kim Byung Wook, "Optical Vehicle to Vehicle Communications for Autonomous Mirrorless Cars.", in Journal of Multimedia information System, Vol. 5, no. 2, pp. 105-110, June 2018

[16] I. Takai, T. Harada, M. Andoh, K. Yasutomi, K. Kagawa and S. Kawahito, "Optical Vehicle-to-Vehicle Communication System Using LED Transmitter and Camera Receiver," in IEEE Photonics Journal, vol. 6, no. 5, pp. 1-14, Oct. 2014

[17] IEEE Standard for Local and metropolitan area networks--Part 15.7: Short-Range Optical Wireless Communications," in IEEE Std 802.15.7-2018 (Revision of IEEE Std 802.15.7-2011) , vol., no., pp.1-407, 23 April 2019

[18] A. Cailean and M. Dimian, "Impact of IEEE 802.15.7 Standard on Visible Light Communications Usage in Automotive Applications," in IEEE Communications Magazine, vol. 55, no. 4, pp. 169-175, April 2017

[19] "Vehicle safety communications project task 3 final report," CAMP Vehicle. Safety Communication. Consortium, Tech. Rep. DOTHS 809 859, Mar. 2005.

[20] IEEE Standard for Information technology-- Local and metropolitan area networks--Specific requirements-- Part 11: Wireless LAN Medium Access Control (MAC) and Physical Layer (PHY) Specifications Amendment 6: Wireless Access in Vehicular Environments," in IEEE Std 802.11p-2010 (Amendment to IEEE Std 802.11-2007 as amended by IEEE Std 802.11k-2008, IEEE Std 802.11r-2008, IEEE Std 802.11y-2008, IEEE Std 802.11n-2009, and IEEE Std 802.11w-2009) , vol., no., pp.1-51, 15 July 2010

[21] A. Cailean, B. Cagneau, L. Chassagne, V. Popa and M. Dimian, "A survey on the usage of DSRC and VLC in communication-based vehicle safety applications," 2014 IEEE 21st Symposium on Communications and Vehicular Technology in the Benelux (SCVT), Delft, 2014, pp. 69-74

[22] T. Yamazato et al., "Image-sensor-based visible light communication for automotive applications," in IEEE Communications Magazine, vol. 52, no. 7, pp. 88-97, July 2014

[23] I. Takai, S. Ito, K. Yasutomi, K. Kagawa, M. Andoh and S. Kawahito, "LED and CMOS Image Sensor Based Optical Wireless Communication System for Automotive Applications," in IEEE Photonics Journal, vol. 5, no. 5, pp. 6801418-6801418, Oct. 2013

[24] Y. Goto et al., "A New Automotive VLC System Using Optical Communication Image Sensor," in IEEE Photonics Journal, vol. 8, no. 3, pp. 1-17, June 2016

[25] M. Atta and A. Bermak, "A 160 m visible light communication link using hybrid undersampled phase-frequency shift on-off keying and CMOS image sensor", Optics Express, vol. 27, no. 3, p. 2478, 2019.

[26] T. Saito, S. Haruyama and M. Nakagawa, "A New Tracking Method using Image Sensor and Photo Diode for Visible Light Road-to-Vehicle Communication," 2008 10th International Conference on Advanced Communication Technology, Gangwon-Do, 2008, pp. 673-678

[27] Satoshi Okada, Tomohiro Yendo, Takaya Yamazato, Toshiaki Fujii, Masayuki Tanimoto and Yoshikatsu Kimura, "On-vehicle receiver for distant visible light road-to-vehicle communication," 2009 IEEE Intelligent Vehicles Symposium, Xi'an, 2009, pp. 1033-1038

[28] B. Béchadergue, C. Dominguez, A. Pesala, P. Chandra, G. Allegretto and S. Richer, "Vehicle-to-Vehicle Optical Wireless Communication with the Smart Corner ™ Automotive Headlamp," 2019 Global LIFI Congress (GLC), Paris, France, 2019, pp. 1-5

[29] A. Căilean, B. Cagneau, L. Chassagne, M. Dimian and V. Popa, "Novel Receiver Sensor for Visible Light Communications in Automotive Applications," in IEEE Sensors Journal, vol. 15, no. 8, pp. 4632-4639, Aug. 2015

[30] N. Lourenço, D. Terra, N. Kumar, L. N. Alves and R. L. Aguiar, "Visible Light Communication System for outdoor applications," 2012 8th International Symposium on Communication Systems, Networks & Digital Signal Processing (CSNDSP), Poznan, 2012, pp. 1-6

[31] G. Singh, A. Srivastava and V. A. Bohara, "Impact of Weather Conditions and Interference on the Performance of VLC based V2V Communication," 2019 21st International Conference on Transparent Optical Networks (ICTON), Angers, France, 2019, pp. 1-4

[32] M. Karbalayghareh, F. Miramirkhani, M. Safari and M. Uysal, "Vehicular Visible Light Communications with SPAD Receivers," 2019 IEEE Wireless Communications and Networking Conference (WCNC), Marrakesh, Morocco, 2019, pp. 1-5

[33] R. W. Zaki, H. A. Fayed, A. Abd El Aziz, and M. H. Aly, "Outdoor Visible Light Communication in Intelligent Transportation Systems: Impact of Snow and Rain," Applied Sciences, vol. 9, no. 24, p. 5453, Dec. 2019.

[34] Y. Kim, W. Cahyadi and Y. Chung, "Experimental Demonstration of VLC-Based Vehicle-to-Vehicle Communications Under Fog Conditions", IEEE Photonics Journal, vol. 7, no. 6, pp. 1-9, 2015.

[35] M. Ijaz et al., "Experimental validation of fog models for FSO under laboratory controlled conditions," 2013 IEEE 24th Annual International Symposium on Personal, Indoor, and Mobile Radio Communications (PIMRC), London, 2013, pp. 19-23

[36] M. Elamassie, M. Karbalayghareh, F. Miramirkhani, R. C. Kizilirmak and M. Uysal, "Effect of Fog and Rain on the Performance of Vehicular Visible Light Communications," 2018 IEEE 87th Vehicular Technology Conference (VTC Spring), Porto, 2018, pp. 1-6

[37] K. Joshi, N. Roy, G. Singh, V. A. Bohara and A. Srivastava, "Experimental Observations on the Feasibility of VLC-Based V2X Communications under various Environmental Deterrents," 2019 IEEE International Conference on Advanced Networks and Telecommunications Systems (ANTS), GOA, India, 2019, pp. 1-4

[38] M. Ijaz, Z. Ghassemlooy, H. Le Minh, S. Rajbhandari and J. Perez, "Analysis of fog and smoke attenuation in a free space optical communication link under controlled laboratory conditions," 2012 International Workshop on Optical Wireless Communications (IWOW), Pisa, 2012, pp. 1-3

[39] E. Eso, A. Burton, N. B. Hassan, M. M. Abadi, Z. Ghassemlooy and S. Zvanovec, "Experimental Investigation of the Effects of Fog on Optical Camera-based VLC for a Vehicular Environment," 2019 15th International Conference on Telecommunications (ConTEL), Graz, Austria, 2019, pp. 1-5

[40] M. Z. Chowdhury, M. K. Hasan, M. Shahjalal, M. T. Hossan and Y. M. Jang, "Optical Wireless Hybrid Networks: Trends, Opportunities, Challenges, and Research Directions," in IEEE Communications Surveys & Tutorials, vol. 22, no. 2, pp. 930-966, Secondquarter 2020

[41] E. Zadobrischi, S. Avătămănitei, A. Căilean, M. Dimian and M. Negru, "Toward a hybrid vehicle communication platform based on VLC and DSRC technologies," 2019 IEEE 15th International Conference on Intelligent Computer Communication and Processing (ICCP), Cluj-Napoca, Romania, 2019, pp. 103-107

[42] European Commission, Motorways, European Commission, Directorate General for Transport, February 2018.

[43] J. Jeong, C. G. Lee, I. Moon, M. Kang, S. Shin and S. Kim, "Receiver angle control in an infrastructure-to-car visible light communication link," 2016 IEEE Region 10 Conference (TENCON), Singapore, 2016, pp. 1957-1960

[44] R. Yang, X. Jin, M. Jin and Z. Xu, "Experimental Investigation of Optical OFDMA for Vehicular Visible Light Communication," 2017 European Conference on Optical Communication (ECOC), Gothenburg, 2017, pp. 1-3

[45] S. Avătămăniţei, A. Căilean, E. Zadobrischi, A. Done, M. Dimian and V. Popa, "Intensive Testing of Infrastructure-to-Vehicle Visible Light Communications in Real Outdoor Scenario: Evaluation of a 50 meters link in Direct Sun Exposure", 2019 Global LIFI Congress (GLC), Paris, France, 2019, pp. 1-5

[46] Hoa Le Minh et al., "80 Mbit/s Visible Light Communications using pre-equalised white LED," 2008 34th European Conference on Optical Communication, Brussels, 2008, pp. 1-2

[47] L. Hanzo, H. Haas, S. Imre, D. O'Brien, M. Rupp and L. Gyongyosi, "Wireless Myths, Realities, and Futures: From 3G/4G to Optical and Quantum Wireless," in Proceedings of the IEEE, vol. 100, no. Special Centennial Issue, pp. 1853-1888, 13 May 2012,

[48] M. A. Atta and A. Bermak, "A Polarisation-Based Interference-Tolerant VLC Link for Low Data Rate Applications," in IEEE Photonics Journal, vol. 10, no. 2, pp. 1-11, April 2018

[49] American Society for Testing and Materials (ASTM), ASTM G173-03(2012), "Standard Tables for Reference Solar Spectral Irradiances: Direct Normal and Hemispherical on 37° Tilted Surface", ASTM International, West Conshohocken, PA, 2012

[50] S. D. Lord, A new software tool for computing Earth's atmospheric transmission of near-and far-infrared radiation. Ames Research Center, 1992

[51] Ghassemlooy Z, Popoola W, Rajbhandari S. "Optical wireless communications: System and Channel Modelling with MATLAB". Boca Raton, FL: Taylor & Francis; 2013, pp. 77-120

[52] Thorlabs, "Light Emitting Diode Technologies: Radiometric vs. Photometric Units", Aug. 2007

[53] UNECE, World Forum for Harmonization of Vehicle Regulations, "Addendum 6: Regulation No. 7, Uniform provisions concerning the approval of front and rear position lamps, stop-lamps and end-outline marker lamps for motor vehicles (except motor cycles) and their trailers", 2012.

[54] M. Conner, "Light spectrum/spectrometer charts and raw data for common lights Designing with LEDs", Designing with LEDs, 2017. [Online]. Available: http://www.designingwithleds.com/light-spectrum-charts-data/. [Accessed: 13- Dec- 2016].

[55] P. Ji, H. M. Tsai, C. Wang and F. Liu, "Vehicular Visible Light Communications with LED Taillight and Rolling Shutter Camera," in Proc. IEEE 79th Veh. Technol. Conf. (VTC Spring), Seoul, 2014, pp. 1-6.

[56] H. Aoyama and M. Oshima, "Visible light communication using a conventional image sensor," 2015 12th Annual IEEE Consumer Communications and Networking Conference (CCNC), Las Vegas, NV, 2015, pp. 103-108.

[57] M. Jafar, D. C. O'Brien, C. J. Stevens and D. J. Edwards, "Evaluation of coverage area for a wide line-of-sight indoor optical free-space communication system employing coherent detection [optical wireless communications]," in IET Communications, vol. 2, no. 1, pp. 18-26, January 2008.

[58] Yang, Dave & El Gamal, Abbas. (1999). "Comparative analysis of SNR for image sensor with widened dynamic range". Proc. SPIE. 3649.

[59] National Optical Astronomy Observatory. "Recommended Light Levels (Illuminance) for Outdoor and Indoor Venues", Nov 2015.

[60] T.Y. Elganimi" Performance Comparison between OOK, PPM and PAM Modulation Schemes for Free Space Optical (FSO) Communication Systems: Analytical Study" in International Journal of Computer Applications, vol. 79, no. 11, Oct. 2013.

[61] Edmund Optics Inc., "Compound Parabolic Concentrators (CPCs)", Edmundoptics.com. [Online]. Available:https://www.edmundoptics.com/optics/optical-lenses/specialty-lenses/compound-parabolic-concentrators-cpcs/3213/. [Accessed: 12- Dec- 2016].

[62] Met Office, “National Meteorological Library and Archive Fact sheet 3 — Water in the atmosphere”, Mar 2012 [Revised Dec 2018]

[63] J. van Boxel. “Numerical model for the fall speed of raindrops in a rainfall simulator”. I.C.E. Special Report, 1998/1, pages 77-85.

[64] Roberto Sabatini, Mark Richardson, “Novel atmospheric extinction measurement techniques for aerospace laser system applications”, Infrared Physics & Technology, Volume 56, 2013, Pages 30-50,

[65] J. Taylor and H. Yates, "Atmospheric Transmission in the Infrared," J. Opt. Soc. Am. 47, 223-226 (1957).

[66] J. Taylor and H. Yates, "Atmospheric Transmission in the Infrared," U. S. Naval Research Laboratory, Washington, D.C., NRL report 5453, June 8, 1960

[67] UNECE, World Forum for Harmonization of Vehicle Regulations, " Regulation No. 87, Revision 2 Uniform provisions concerning the approval of daytime running lamps for power-driven vehicles", 2009

[68] Hamamatsu, “InGaAs PIN Photodiodes: G12180 Series”, Jul. 2018

[69] Hamamatsu, “Si PIN Photodiodes: S3071 Series”, Nov. 2014

[70] T. Erdogan and L. Wang, “Semrock VersaChrome Tunable Bandpass Filters,” Semrock, Rochester, NY, USA. Jan. 2010

[71] Redshirt Imaging, “Fast, Low Noise, Camera System for Biological Research” FastCMOS-128X datasheet. May. 2013 [Revised Jun. 2013].

[72] Ghassemlooy, Z., Popoola, W. and Rajbhandari, S. (2013). “Optical wireless communications: System and Channel Modelling with MATLAB”. Boca Raton, Fla.: CRC Press, p.449.

[73] J. Peterson and T. Krauss, "Photobrightening and photodarkening in PbS quantum dots", Physical Chemistry Chemical Physics, vol. 8, no. 33, p. 3851, 2006.

[74] Bera, D., Qian, L., Tseng, T. and Holloway, P. (2010). Quantum Dots and Their Multimodal Applications: A Review. Materials, 3(4), pp.2260-2345.

[75] Wegner, K. and Hildebrandt, N. (2015). Quantum dots: bright and versatile in vitro and in vivo fluorescence imaging biosensors. Chemical Society Reviews, 44(14), pp.4792-4834.

[76] C. Cheng, J. Li and X. Cheng, "Photoluminescence lifetime and absorption spectrum of PbS nanocrystal quantum dots", Journal of Luminescence, vol. 188, pp. 252-257, 2017

[77] Quantum Solutions, “Emission spectra” Lead Sulfide (PbS) Quantum Dots: Technical Data Sheet, Jun. 2019

[78] Quantum Solutions, “Certificate of Analysis: Lead Sulfide PbS Quantum Dots” QD-LS-1400-em datasheet, Nov. 2018

[79] Chow, W. and Jahnke, F. (2013). On the physics of semiconductor quantum dots for applications in lasers and quantum optics. Progress in Quantum Electronics, 37(3), pp.109-184.

[80] Di Bartolo, B. (2012). Introduction to Fluorescence Spectroscopy with Applications to Biological Systems. NATO Science for Peace and Security Series B: Physics and Biophysics, pp.91-117.

[81] OSRAM "OSLON® Compact CM" LUW CEUN.CE, Nov 2019

[82] OSRAM "OSLON® Compact CL" LUW CEUP.CE, Nov 2018

[83] Keysight Technologies, "Keysight 81150A and 81160A Pulse Function Arbitrary Noise Generators" 81150A datasheet, Aug. 2018

[84] Zhang, J. and Xiao, P. (2018). 3D printing of photopolymers. Polymer Chemistry, 9(13), pp.1530-1540.

[85] Thorlabs, "Large Area InGaAs Amplified Photodetector: PDA20C / PDA20C/M Operation Manual" PDA20C/M datasheet, Jan. 2012

[86] Hamamatsu, "APD Modules: C12702 Series" C12702-04 datasheet, Sep. 2017

[87] Newport "Typical spectral responsivity of Newport's low power detectors" 818 Series Calibrated photodiode Sensors, May 2015

[88] C. Wyman, P. Sloan and P. Shirley, "Simple Analytic Approximations to the CIE XYZ Color Matching Functions", Journal of Computer Graphics Techniques, vol. 2, no. 2, 2013.

[89] Ghassemlooy, Z., Popoola, W. and Rajbhandari, S. (2013). "Optical wireless communications: System and Channel Modelling with MATLAB". Boca Raton, Fla.: CRC Press, pp.323-341

[90] F. Zafar, M. Bakaul and R. Parthiban, "Laser-Diode-Based Visible Light Communication: Toward Gigabit Class Communication," in IEEE Communications Magazine, vol. 55, no. 2, pp. 144-151, February 2017.

[91]: ILX Lightwave, "An Overview of Laser Diode Characteristics", Feb 2012

[92] Thorlabs, "High-Power IR LED with Ball Lens, 1450 nm" LED1450L datasheet, Mar. 2019 [Revision D].

[93] Horowitz, P. and Hill, W., 2015. The Art of Electronics. 3rd ed. Cambridge University Press, p.227-229.

[94] Ott, H., 2009. Electromagnetic Compatibility Engineering. Hoboken: John Wiley & Sons.

[95] S. Collins, D. C. O'Brien, and A. Watt, "High gain, wide field of view concentrator for optical communications," *Optics Letters*, 19-Mar-2014.

[96] M. Rafiee, S. Chandra, H. Ahmed, and S. J. McCormack, "An overview of various configurations of Luminescent Solar Concentrators for photovoltaic applications," *Optical Materials*, 26-Mar-2019.

[97] Y. Zhou, D. Benetti, Z. Fan, H. Zhao, D. Ma, A. O. Govorov, A. Vomiero, and F. Rosei, "Near Infrared, Highly Efficient Luminescent Solar Concentrators," *Wiley Online Library*, 31-Mar-2016.

[98] Rahmat Mulyawan, Ariel Gomez, Hyunchae Chun, Sujan Rajbhandari, Pavlos P. Manousiadis, Dimali A. Vithanage, Grahame Faulkner, Graham A. Turnbull, Ifor D. W. Samuel, Stephen Collins, Dominic O'Brien, "A comparative study of optical concentrators for visible light communications," Proc. SPIE 10128, Broadband Access Communication Technologies XI, 101280L (28 January 2017)

[99] P. P. Manousiadis, S. Rajbhandari, R. Mulyawan, D. A. Vithanage, H. Chun, G. Faulkner, D. C. O'Brien, G. A. Turnbull, S. Collins, and I. D. Samuel, "Wide field-of-view fluorescent antenna for visible light communications beyond the étendue limit," *Optica*, vol. 3, no. 7, p. 702, 2016.

[100] T. Peyronel, K. J. Quirk, S. C. Wang, and T. G. Tiecke, "Luminescent detector for free-space optical communication," *Optica*, 19-Jul-2016.

[101] P. P. Manousiadis, H. Chun, S. Rajbhandari, D. A. Vithanage, R. Mulyawan, G. Faulkner, H. Haas, D. C. Obrien, S. Collins, G. A. Turnbull, and I. D. W. Samuel, "Optical Antennas for Wavelength Division Multiplexing in Visible Light Communications beyond the Étendue Limit," *Advanced Optical Materials*, vol. 8, no. 4, p. 1901139, 2019.

[102] R. Mulyawan, H. Chun, A. Gomez, S. Rajbhandari, G. Faulkner, P. P. Manousiadis, D. A. Vithanage, G. A. Turnbull, I. D. W. Samuel, S. Collins, and D. Obrien, "MIMO Visible Light Communications Using a Wide Field-of-View Fluorescent Concentrator," *IEEE Photonics Technology Letters*, vol. 29, no. 3, pp. 306–309, Jan. 2017.

[103] A. Riaz, G. Faulkner, and S. Collins, "A Fluorescent Antenna for White Light Visible Light Communications," *2019 Global LIFI Congress (GLC)*, 2019.

[104] C. Quintana, H. Chun, R. Mulyawan, G. Faulkner, S. Collins, D. C. Obrien, E. Xie, J. J. D. Mckendry, E. Gu, M. D. Dawson, P. P. Manousiadis, D. A. Vithanage, G. A. Turnbull, and I. D. Samuel, "Ultra-wide coverage VLC system with alignment-free receiver," *2018 Global LIFI Congress (GLC)*, 2018.

[105] T. Wang, B. Yu, B. Chen, Z. Hu, Y. Luo, G. Zou, and Q. Zhang, "A theoretical model of a cylindrical luminescent solar concentrator with a dye-doping coating," *Journal of Optics*, vol. 15, no. 5, p. 055709, 2013.

[106] S. F. H. Correia, P. P. Lima, P. S. André, M. R. S. Ferreira, and L. A. D. Carlos, "High-efficiency luminescent solar concentrators for flexible waveguiding photovoltaics," *Solar Energy Materials and Solar Cells*, 18-Mar-2015.

[107] E. H. Banaei and A. F. Abouraddy, "Design of a polymer optical fiber luminescent solar concentrator," *Wiley Online Library*, 17-Dec-2013.

[108] J. C. Goldschmidt, M. Peters, A. Bösch, H. Helmers, F. Dimroth, S. W. Glunz, and G. Willeke, "Increasing the efficiency of fluorescent concentrator systems," *Solar Energy Materials and Solar Cells*, 03-Dec-2008.

[109] Ha, Su-Jin; Kang, Ji-Hwan; Choi, Dong Ho; Nam, Seong Kyung; Reichmanis, Elsa; Moon, Jun Hyuk (2018): Upconversion-Assisted Dual-Band Luminescent Solar Concentrator Coupled for High Power Conversion Efficiency Photovoltaic Systems. ACS Publications. Collection.

[110] Shim, H., Kim, H., Kim, J., Kim, S., Jeong, W., Kim, T. and Kim, J., 2012. Enhancement of near-infrared absorption with high fill factor in lead phthalocyanine-based organic solar cells. Journal of Materials Chemistry, 22(18), p.9077.

[111] A. Sanguineti, A. Monguzzi, G. Vaccaro, F. Meinardi, E. Ronchi, M. Moret, U. Cosentino, G. Moro, R. Simonutti, M. Mauri, R. Tubino, and L. Beverina, "NIR emitting ytterbium chelates for colourless luminescent solar concentrators," *Physical Chemistry Chemical Physics*, 16-Mar-2012.

[112] F. Meinardi, H. McDaniel, F. Carulli, A. Colombo, K. A. Velizhanin, N. S. Makarov, R. Simonutti, V. I. Klimov, and S. Brovelli, "Highly efficient large-area colourless luminescent solar concentrators using heavy-metal-free colloidal quantum dots," *Nature News*, 24-Aug-2015.

[113] C. Li, W. Chen, D. Wu, D. Quan, Z. Zhou, J. Hao, J. Qin, Y. Li, Z. He, and K. Wang, "Large Stokes Shift and High Efficiency Luminescent Solar Concentrator Incorporated with CuInS 2 /ZnS Quantum Dots," *Nature News*, 08-Dec-2015.

[114] N. D. Bronstein, "Material and Optical Design Rules for High Performance Luminescent Solar Concentrators," *eScholarship, University of California*, 14-Sep-2016.

[115] N. D. Bronstein, Y. Yao, L. Xu, E. O'Brien, A. S. Powers, V. E. Ferry, A. P. Alivisatos, and R. G. Nuzzo, "Quantum Dot Luminescent Concentrator Cavity Exhibiting 30-fold Concentration," *ACS Photonics*, vol. 2, no. 11, pp. 1576–1583, 2015.

[116] Bavali, A., Parvin, P., Mortazavi, S., Mohammadian, M. and Mousavi Pour, M., 2014. Red/blue spectral shifts of laser-induced fluorescence emission due to different nanoparticle suspensions in various dye solutions. Applied Optics, 53(24), p.5398.